Title
Controlling Thermal Emission: Fundamental Mechanisms and Applications to Water and Energy Technologies

Author
Huang, Xin N/A

Publication Date
2023

Peer reviewed|Thesis/dissertation

UNIVERSITY OF CALIFORNIA

Los Angeles

Controlling Thermal Emission: Fundamental Mechanisms and Applications to Water and Energy Technologies

A dissertation submitted in partial satisfaction of the

requirements for the degree of Doctor of Philosophy

in Materials Science and Engineering

by

Xin Huang

2023

ABSTRACT OF THE DISSERTATION

Controlling Thermal Emission: Fundamental Mechanisms and Applications to Water and Energy Technologies

by

Xin Huang

Doctor of Philosophy in Materials Science and Engineering

University of California, Los Angeles, 2023

Professor Aaswath P. Raman, Chair

Thermal radiation provides radiative access to all heat sources, with the sun representing the most important renewable energy resource and the universe representing the ultimate heat sink. Thermal radiation could have many applications such as solar energy harvesting and radiative cooling. In our quest to utilize various thermodynamic resources including both heat sources and heat sinks, the ability to control thermal radiation plays a fundamentally important role. Here, we will take advantage of the emerging tools at the intersection of photonic materials and metamaterials, thermal science and energy applications, namely coupled-mode theory to tailor the thermal radiation behaviors from multiple arbitrary numbers of resonators, radiative cooling for freezing desalination and radiative cooling atmosphere water harvesting.

The dissertation of Xin Huang is approved.

Ximin He

Qibing Pei

Laurent Pilon

Aaswath P. Raman, Committee Chair

University of California, Los Angeles

2023

Table of Contents

Acknowledgements

I'd like to express my gratitude to a number of people who have helped me over the years and without whom this work would not have been possible. First and foremost, I'd like to express my gratitude to Professor Aaswath Raman for the opportunity to work in his lab for the past four years. His insight and guidance were invaluable, and I will remember the lessons I learned for the rest of my life. I'd like to thank Dr. Jyotirmoy Mandal for patient mentoring my research and work. I'd like to thank my lab colleagues and contemporaries, Dr. Jin Xu, John Brewer, Dr. Christopher Yeung, Jae Hwang, David Abraham, and Dr. Parthiban Santhanam, for providing excellent feedback that helped improve the quality of this work. May you all continue to lead long successful careers and find fulfillment and happiness in the process. I would also like to thank the Prof. Ximin He, providing me the guidance on the collaboration work. I would also like to thanks to the Dr. Shuwang Wu as well as Yousif Alsaid from Prof. He's group for the help and advice on the collaboration project. I would also like to thank the Professors on my committee: Prof. Ximin He, Prof. Qibing Pei, Prof. Laurent Pilon for their questions and suggestions which have greatly influenced the direction of this work.

Finally, I would like to thank my family for their love, support, and encouragement which helped shape who I am today. Especially to my sweet wife, Jiawei Sun, this journey would not have been possible without you.

Vita

2012-2016	Bachelor of Engineering in Materials Chemistry Zhengzhou University
2016-2018	Master of Science in Material Science University of Rochester
2018-2023	Graduate Student Researcher – Raman Lab University of California Los Angeles, Los Angeles, California
2022	Optical Material Engineer internship Western Digital, Fremont, California
2023	Display Optical Engineer internship Apple, Cupertino, California

Select Publications

- ***Xin Huang***, J. Mandal, J. Xu, A. Raman. Passive freezing desalination driven by radiative cooling. *Joule* **2022**, 6,12, 2762-2775.
- ***Xin Huang***, C. Yeung, A. Raman. Temporal coupled-mode theory for thermal emission from multiple arbitrarily coupled resonators. *Physical Review Applied* **2023**, 19, 034037
- J. Mandal, ***Xin Huang***, A. Raman. Accurately quantifying clear-sky radiative cooling potentials: a temperature correction to the transmittance-based approximation. *Atmosphere* **2021**, 12(9), 1195.
- ***Xin Huang***, J. Mandal, A. Raman. A do-it-yourself radiative cooler as a radiative cooling standard and cooling component for device design. *Journal of Photonics for Energy* **2021**,12(1),012112.
- ***Xin Huang***, S. Wu, J. Mandal, X. He and A. Raman. High-efficiency dew condensation and collection using slippery hydrophilic radiative cooling surfaces. In preparation (2023).

Chapter 1: Introduction

Broad spectrum electromagnetic waves interact with the materials around us every day. All matter with an absolute temperature above zero emits thermal radiation, ranging from the cold universe at a temperature of 3 K to the sun at 6000 K. Therefore, thermal radiation provides radiative access to all heat sources, with the sun representing the most important renewable energy resource and the universe representing the ultimate heat sink.

One important application that can make use of thermal radiation is desalination. With increasing water scarcity there is now a significant push to find more efficient and low-cost ways to generate fresh water from seawater or other non potable water sources. At the same time, many industrial processes, including oil and gas production and (in particular fracking) produce saline wastewater that require desalination. The most commonly used thermal desalination method is solar desalination which uses the sun as the heat source to achieve water and salt separation through an evaporation-condensation cycle. However, weather conditions and solar insolation in general mean that this approach is only viable during the day and at certain times of the year. Here, by contrast, we focus on the cold side of the thermal process with another phase change that can also enable desalination: the freeze-melt cycle. In particular, we use the ultimate heat sink, outer space, through radiative cooling to enable this behavior.

Atmospheric water harvesting is emerging as an important approach for potable water generation, particularly in dry landlocked places. However, the high energy costs associated with condensation and capture of water vapor remains a big challenge. In this context, exploiting passive radiative cooling to condense water vapor has attracted much attention with the advantage of cooling down the water vapor below dew point passively without active energy input. However, maximizing the efficiency of condensation and collection of dew on the radiative cooling surface

remains a challenge, with most condensed water typically requiring mechanical means of collection. Here, we create and demonstrate a slippery hydrophilic radiative cooling surface (SRCs) that through its high infrared emissivity, enables effective sub-ambient cooling, and through its surface wettability characteristics optimizes both the condensation and collection of the water.

In our quest to utilize various thermodynamic resources including both heat sources and heat sinks, the ability to control thermal radiation plays a fundamentally important role. Conventional thermal emitters have a set of common characteristics: the emitted radiation is typically incoherent, broadband, un-polarized, and the emission pattern is near-isotropic. However, over the past 20 years, with the development of nanophotonics, it has been shown that coherent, narrowband, polarized and directional thermal radiation is in principle possible. One particular class of device is the metamaterial absorber which finds a wide variety of practical applications including selective thermal emitters[1], wavelength-tunable microbolometers[2], and refractive index sensing[3]. In many applications such as solar energy harvesting and radiative cooling, however, broadband yet spectrally selective absorption or emission is required. Since the mechanism of metamaterial absorbers is based on the strong electromagnetic resonance in the periodic structure, the bandwidth of this resonant absorption is narrow by nature[4]. But this raises a basic question of whether such a tradeoff is a fundamental limit, or whether the thermal emission spectrum from these nanostructures can be arbitrarily engineered. Here, we will probe these questions through theoretical analysis as well as a numerical study, with the goal of developing first-principles strategies for constructing arbitrary thermal spectra.

In this thesis, we will take advantage of the emerging tools at the intersection of photonic materials and metamaterials, thermal science and energy applications, namely coupled-mode

theory to tailor the thermal radiation behaviors from multiple arbitrary numbers of resonators, radiative cooling for freezing desalination and atmospheric water harvesting.

Chapter 2: Temporal coupled-mode theory for thermal emission from multiple arbitrarily-coupled resonators

2.1 Introduction

Thermal emission is a fundamental physical process whose control is essential for a broad range of imaging, sensing and energy technologies. Conventional thermal emitters are typically incoherent, broadband, unpolarized and lack directionality. Over the last two decades, a range of photonic strategies have by contrast shown that it is indeed possible to create narrowband, polarized and/or directional thermal emitters[1-8]. The spectral characteristics of thermal emission in particular have been sculpted through a range of nanophotonic approaches including metallic nanoantennas[9, 10], photonic crystals[11-16] and semiconductor nanorods[17]. Tailoring the frequency and bandwidth response of emitted thermal radiation using nanophotonic strategies has in turn proved critical for improved performance in many emerging applications, including thermophotovoltaics[13, 18-23], radiative cooling[24-30] and thermal management[31-34].

Conventional strategies to achieve an arbitrary degree of control over spectral selectivity for a thermal emitter rely on either numerical optimization or exploiting known electromagnetic mode behavior in conventional photonic systems. In this context, a resonance based approach to understanding thermal emission spectra in a more systematic way. Temporal coupled-mode theory[35, 36] in particular is a widely-used semi-analytical method that has been shown to provide excellent approximations and physical insight into the behavior of a range of resonance- and mode-driven nanophotonic structures and devices[37-42].

Recently, temporal coupled mode theory for singe-mode thermal emitters was developed to analytically model the thermal emission from such an emitter with high accuracy[43]. Further work has extended this coupled-mode theory to include coupling between multiple identical

resonant thermal emitters, and shown that thermal emission decreases with increasing number of identical thermal emitters in analogy to quantum superradiance effects[44]. As a semi-analytical model, coupled-mode theory is able to offer deeper insight on the effect of material and structural parameters and the resulting spectral nature of their thermal emission, an insight that simulations alone cannot offer. However, prior work has been limited to describing a constrained set of thermal emitters due to the resonators being identical in character. For many practical scenarios, highly complex and selective thermal emission spectra with multiple frequency peaks and varying bandwidths are desirable, but difficult to achieve with single-mode resonators, and more generally are challenging to elucidate. One particularly promising mechanism to achieving complex thermal emission spectra is to consider systems supporting multiple arbitrary resonators[9,10] which may additionally couple or hybridize with each other, thereby enhancing or suppressing thermal emission with several degrees of potential freedom to control the resulting spectral response. Such a scenario, while intriguing, is however challenging to model analytically and can require many complex and slow simulations. A universal theoretical framework for understanding the full range of complex coupling, and resulting thermal emission that may be possible in multi-resonant photonic structures is currently lacking, but could enable deeper insights into the behavior of such structures and enable more rapid design of their arrangements.

In this Letter we introduce an extended temporal coupled-mode theory framework to derive an analytical formalism to model thermal emission from an arbitrary number of resonators which can arbitrarily couple to each other. We validate the theory against simulation-based calculations of thermal emission from a range of physically realizable systems. We first demonstrate the coupled-mode theory's accuracy for multiple two-dimensional slit resonators, where the dielectric permittivity of each slit can vary, along with the distance between each slit, thereby altering both

the real and imaginary part of the coupling coefficient. We also demonstrate the coupled-mode theory's capabilities with a three slit system, highlighting how both subradiant enhancement and superradiant suppression of thermal emission can be selectively engineered at different frequencies. Finally, we demonstrate the accuracy of the coupled-mode theory in predicting the thermal emission spectra of supercell three-dimensional metal-dielectric-metal resonators for a range of inter-resonator distances. Collectively, our results offer a general theoretical framework capable of taking the response of individual resonators and using them to determine their complex spectral response when integrated and hybridized with each other.

2.2 Results and Discussion

Extended coupled-mode theory

We first develop an extended temporal coupled-mode theory capable of describing the collective thermal emission from N different emitters that are coupled to each other with varying degrees of strength. Each resonant emitter is assumed to have an amplitude $a = (a_1, a_2, \dots, a_N)^T$. The energy stored inside an emitter may decay through three pathways. The first pathway is through intrinsic absorption which is represented by the intrinsic decay rate $\mathbf{\Gamma_0} = diag(\gamma_{01}, \gamma_{02}, \dots \gamma_{0N})$. The second is to decay to the external free space channels, which is described by the external decay rate $\mathbf{\Gamma_e} = diag(\gamma_{e1}, \gamma_{e2}, \dots \gamma_{eN})$. The third is through coupling with other resonators, which is expressed by a complex coupling coefficient matrix K defined as

$$\begin{pmatrix} 0 & \kappa_{12} + i\beta_{12} & \cdots & \kappa_{1(N-1)} + i\beta_{1(N-1)} & \kappa_{1N} + i\beta_{1N} \\ \kappa_{21} + i\beta_{21} & 0 & \cdots & \kappa_{2(N-1)} + i\beta_{2(N-1)} & \kappa_{2N} + i\beta_{2N} \\ \vdots & & \ddots & & \vdots \\ \kappa_{(N-1)1} + i\beta_{(N-1)1} & \kappa_{(N-1)2} + i\beta_{(N-1)2} & \cdots & 0 & \kappa_{(N-1)N} + i\beta_{(N-1)N} \\ \kappa_{N1} + i\beta_{N1} & \kappa_{N2} + i\beta_{N2} & \cdots & \kappa_{N(N-1)} + i\beta_{N(N-1)} & 0 \end{pmatrix} \quad (1)$$

.To capture arbitrary coupling between resonating elements, we define κ as the real part of the coupling coefficient, which in our context can capture scenarios such as variable distance between resonators, and β which is the imaginary part of the coupling strength, and captures the phase difference between resonators. In the framework of the fluctuation- dissipation theorem, the absorption process is balanced by a random thermal excitation source $\boldsymbol{n}$. With all these considerations, the dynamic equations for resonance amplitudes can be written in the following form:

$$\frac{d\boldsymbol{a}}{dt} = (j\boldsymbol{\Omega_0} - \boldsymbol{\Gamma_0} - \boldsymbol{\Gamma_e})\boldsymbol{a} + \sqrt{2\boldsymbol{\Gamma_0}}\boldsymbol{n} - \boldsymbol{K}\boldsymbol{a} \tag{2}$$

where $\boldsymbol{\Omega_0} = diag(\omega_1, \omega_2, \ldots \omega_N)$ describes the resonant frequency of each resonator. We can explicitly calculate $\boldsymbol{a}(\omega)$ in the frequency domain,

$$\boldsymbol{a}(\omega) = (j(\omega - \boldsymbol{\Omega_0}) + \boldsymbol{\Gamma_0} + \boldsymbol{\Gamma_e} + \boldsymbol{K})^{-1}\sqrt{2\boldsymbol{\Gamma_0}}\boldsymbol{n} \tag{3}$$

We normalize the amplitude so that the mode energy is given by $|\boldsymbol{a}|^2$. Here we have introduced a noise source vector $\boldsymbol{n}$ in Eq. (1), to compensate for the intrinsic resonator loss and maintain thermal equilibrium [43]. Following the fluctuation-dissipation theorem this noise source is defined by a correlation function (See Supplementary Information):

$$\langle \boldsymbol{n}^*(\omega)\boldsymbol{n}(\omega')\rangle = \frac{1}{2N\pi}\boldsymbol{\Theta}(\omega, T)\delta(\omega - \omega') \tag{4}$$

Where $\boldsymbol{\Theta}(\omega, T) = \frac{\hbar\omega}{e^{\frac{\hbar\omega}{kT}} - 1}$. The total power emitted as thermal radiation, $\langle P\rangle$, can then be calculated as

$$\langle \boldsymbol{P}(t)\rangle = 2\boldsymbol{\Gamma_e}\langle \boldsymbol{a}^*(t)\boldsymbol{a}(t)\rangle = 2\boldsymbol{\Gamma_e}\int_0^\infty d\omega \int_0^\infty d\omega' \boldsymbol{e}^{-j(\boldsymbol{\omega}-\boldsymbol{\omega}')\boldsymbol{t}}\langle \boldsymbol{a}^*(\omega)\boldsymbol{a}(\omega')\rangle \tag{5}$$

Solving for the power spectral density of thermal emission we find that

$$\boldsymbol{P}(\omega) = \frac{\boldsymbol{\Theta}(\omega,T)}{2N\pi} 4\boldsymbol{\Gamma_e}((\boldsymbol{j}(\omega - \boldsymbol{\Omega_0}) + \boldsymbol{\Gamma_0} + \boldsymbol{\Gamma_e} + \boldsymbol{K})^{-1})^2\boldsymbol{\Gamma_0} \tag{6}$$

Here, as in conventional expositions of temporal coupled mode theory for multi-port systems, we assume that each resonances can decay into every other port in the system, described by a total value d_{ij} and encompassed by a coupling matrix **D**:

$$\boldsymbol{D} = \begin{pmatrix} d_{11} & d_{12} & \cdots & d_{1(N-1)} & d_{1N} \\ d_{21} & d_{22} & \cdots & d_{2(N-1)} & d_{2N} \\ \vdots & & \ddots & & \vdots \\ d_{(N-1)1} & d_{(N-1)2} & \cdots & d_{(N-1)(N-1)} & d_{(N-1)N} \\ d_{N1} & d_{N2} & \cdots & d_{N(N-1)} & d_{NN} \end{pmatrix} \tag{7}$$

By energy conservation the total coupling matrix **D** bounds the values of the coupling coefficients to each relevant channel (see Supplementary Information):

$$2(\boldsymbol{\Gamma_0} + \boldsymbol{\Gamma_e} + \boldsymbol{K}) = \boldsymbol{D}^{+}\boldsymbol{D} \tag{8}$$

Eq. (6) is a key result of this paper and provides a general expression for thermal emission from N resonators that are coupled to each other arbitrarily. To elucidate the power of this result, we first write analytical forms for small N scenarios of typical interest, beginning with the N=1 scenarios where coupling is not relevant:

$$P(\omega) = \frac{\boldsymbol{\Theta}(\omega,\boldsymbol{T})}{2\pi} \frac{4\gamma_{01}\gamma_{e1}}{(\omega-\omega_1)^2+(\gamma_{01}+\gamma_{e1})^2} \tag{9}$$

This expression is simply a standard Lorentzian form of power emitted due to a single resonance previously derived in Ref. 43. For two resonators ($N = 2$), however, we must include complex coupling terms $\kappa_{ij} + i\beta_{ij}$ for generality. This results in the following expression for the radiated power:

$$P(\omega) = \frac{\Theta(\omega,T)}{4\pi}\left(\frac{4\gamma_{01}\gamma_{e1}\alpha_2^2+4\gamma_{e1}\gamma_{02}\kappa_{12}^2+4\gamma_{e1}\gamma_{02}\beta_{12}^2-8\alpha_2\kappa_{12}\gamma_{e1}\sqrt{\gamma_{01}\gamma_{02}}}{(\alpha_1\alpha_2-(\kappa_{12}+i\beta_{12})(\kappa_{21}+i\beta_{21}))^2} + \right.$$

$$\left.\frac{4\gamma_{e2}\gamma_{02}\alpha_1^2+4\gamma_{e2}\gamma_{01}\kappa_{21}^2+4\gamma_{e2}\gamma_{01}\beta_{21}^2-8\alpha_1\kappa_{21}\gamma_{e2}\sqrt{\gamma_{01}\gamma_{02}}}{(\alpha_1\alpha_2-(\kappa_{12}+i\beta_{12})(\kappa_{21}+i\beta_{21}))^2}\right) \tag{10}$$

Here for convenience we have introduced variables α_j defined as:

$$\alpha_j = i(\omega - \omega_j) + \gamma_{0j} + \gamma_{ej}$$

κ_{12} and κ_{21} are the real parts of the coupling term determined by the spatial distance between the resonances, while the complex terms β_{12} and β_{21} describe the phase mismatch between resonances. Due to energy conservation, a two resonator system is constrained by Eq. (8), resulting in the following expression:

$$\cos(\theta_{12} - \theta_{11}) + i\sin(\theta_{12} - \theta_{11}) + \cos(\theta_{22} - \theta_{21}) + i\sin(\theta_{22} - \theta_{21}) = \frac{2\kappa_{12} + 2j\beta_{12}}{\sqrt{(\gamma_{01} + \gamma_{e1})(\gamma_{02} + \gamma_{e2})}} \quad (11)$$

Here, θ_{ij} is the phase angle of d_{ij}. As in conventional coupled-mode theory, this energy conservation relation extends to arbitrary numbers of resonators and fundamentally links the various coupling terms external to each resonator: coupling to neighboring resonators or to free space. In the two resonator case, we can first consider the scenario when the two resonators are spatially closed each other. In this case, as the two resonators move closer and closer, θ_{12} will be getting closer to θ_{11} and θ_{21} will be getting closer to θ_{22}. Therefore, $\cos(\theta_{12} - \theta_{11})$ is near 1 and $\sin(\theta_{12} - \theta_{11})$ is near 0, and the total thermal emission peak power is strongly driven by the real part of the coupling coefficients. When the two resonators are physically far away from each other, as θ_{12} and θ_{21} is small, the coupling strength is determined by the phase angle of θ_{11} and θ_{22}. If θ_{11} and θ_{22} closes to $\pi/2$, the total thermal emission peak is mainly determined by the imaginary portion of the coupling strength which encodes phase mismatch. If θ_{11} and θ_{22} closes to 0, the total thermal emission peak power is strongly driven by the real part of the coupling coefficients. More generally, the behavior of each resonant peak in an arbitrary multiple-resonance system is determined by both real and imaginary parts of the coupling coefficients.

Numerical results

To validate the extended couple-mode theory developed above, we consider an exemplary system consisting of multiple narrow dielectric slits of arbitrary permittivity which are introduced into a perfect electric conductor (PEC) layer, as shown in Fig. 1(a). In the system, the optical fields are confined in the slit and can couple with each other. This system is an extension of the slit resonator system considered in Ref. [44] which consider multiple identical resonators that were sufficiently close to each other to enable near-field coupling.

We first consider the two resonator (two dielectric slit) scenario and demonstrate how the

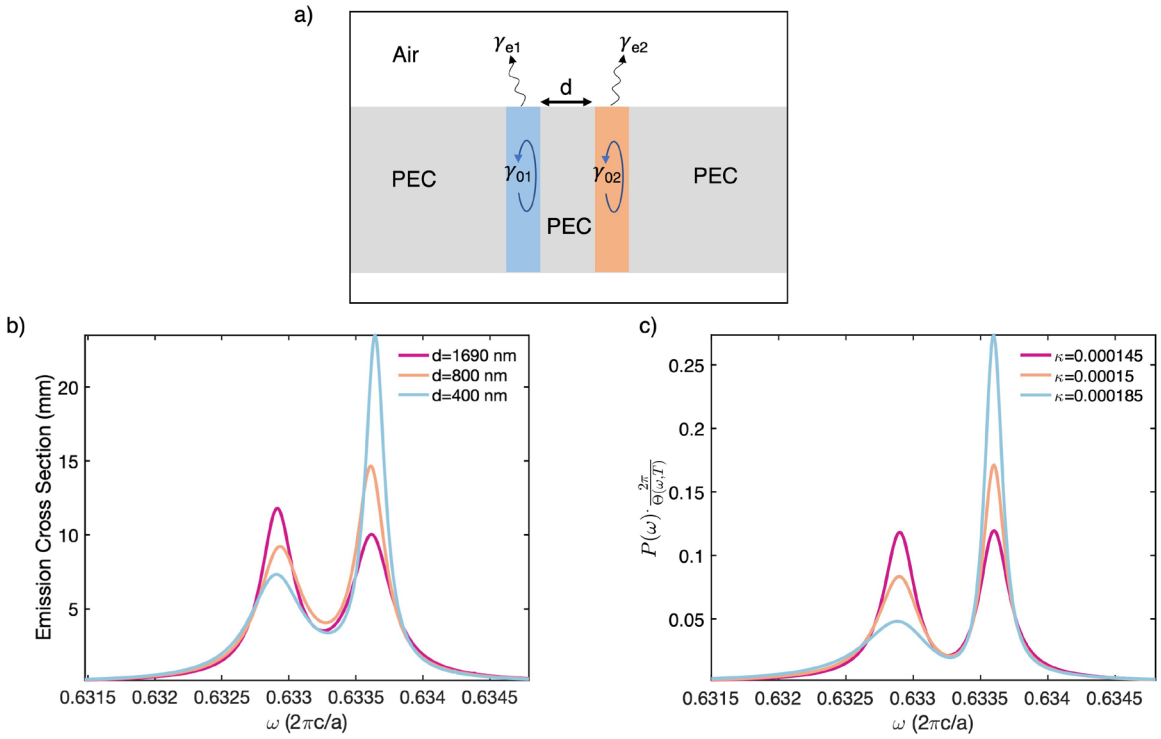

Figure 1. The effect of varying distance between dissimilar resonators. a) The structure of resonant emitters consisting of two slits in two PEC slabs. The length and width of the slit are 1.4 μm and 5nm, respectively. They are filled with two different emissive materials with a

dielectric constant of $\varepsilon_1 = 12.5 + 0.001i$ and $\varepsilon_2 = 12.53 + 0.001i$. b) FDFD-simulated spectra of emission cross section for two resonant emitters with a distance of 400 nm, 800 nm and 1690 nm, separately. c) Coupled mode theory thermal emission power prediction for two different emitters with a coupling strength of $\kappa = 0.000145$, $\kappa = 0.00015$, $\kappa = 0.000185$

Coupled-mode theory accurately predicts the effect of varying distance between dissimilar resonators, as well as differing permittivities at a fixed separation distance. In this scenario, the slits are 1.4 μm wide, and 5 nm long, and contain dielectric media with permittivities $\varepsilon_1 = 12.5 + 0.001i$ and $\varepsilon_2 = 12.53 + 0.001i$ respectively. Since the permittivity of each slit is different the system supports resonances at slightly different frequencies, ω_1 and ω_2 as can be seen in Fig. 1(b). We then calculate the emission cross section of this system using the finite-difference frequency domain method for different values of the slit separation distance d as shown in Fig. 1(b). Simulations reveal a notable behavior as we decrease the distance between two resonators: the resonator with lower dielectric permittivity sees a large enhancement in its total associated emission while a large decrease for the resonator with higher permittivity is observed.

We next model the same system using the extended coupled-mode theory and compare its predictions to the FDFD simulations. By defining a purely real inter-resonator coupling constant, κ and examining a range of its values we are able to systematically replicate the trend observed in Fig. 1(b) in Fig. 1(c) remarkably well. In particular, as the two resonators are moved closer, the real part of the coupling strength further increases. This in turn influences the internal coupling coefficients γ_{01} and γ_{02} and external coupling coefficients γ_{e1}

and γ_{e2} due to energy conservation. As detailed in the Supplementary Information, further increasing the real part of coupling constant will need to increase $\sqrt{(\gamma_{01}+\gamma_{e1})(\gamma_{02}+\gamma_{e2})}$ thereby resulting in a decrease of the lower frequency peak, and an increase of the higher frequency peak. The exact same behavior is observed in the FDFD simulations, with a small variation in resonance frequency the only notable difference. This result suggests that once coupling coefficients have been established for a particular multi-resonator system of interest, the temporal coupled-mode theory can be used as a rapid simulator of thermal emission from the class of nanophotonic structures being examined.

Next, we examine the effect of changing the permittivity in one of the two dielectric slits at a fixed, large distance d = 800 nm (Fig. 2(a)). As the permittivity of one of the slits is changed, the imaginary part of inter-resonator coupling coefficient, β changes due to phase difference between each resonator. Since the resonators are far apart, we expect minimal contribution from the real part of the coupling coefficient κ. In our system, we maintain the permittivity of ε_1 as 12.5+0.001i and change the permittivity of ε_2 to 12.5008+0.001i, 12.53 + 0.001i, and 12.55 + 0.001i respectively. FDFD simulations shown in Fig. 2(b) highlight that as ε_2 changes the emission peak associated with resonator 2 increases first, reaching a peak at $\Delta\varepsilon$ = 0.03 but then decreasing as ε_2 is further increased. We explore the same system using coupled-mode theory in Fig. 2(c) and find a range of β values which result in exactly the same behavior observed in the FDFD simulations, further demonstrating the utility of this coupled-mode theory model. Indeed, we emphasize that a purely real coupling coefficient would be insufficient to capture the scenarios shown here. Referring back to Eq. (11) we observe that as the sin(θ) term purely influences β it thereby encodes the phase difference between the resonators, which peaks at $\theta = \pi/2$ which corresponds to a particular β

value depending on the strengths of the internal coupling coefficients γ_0 and external coupling coefficients of the resonances γ_e.

To highlight the generality and flexibility of the developed coupled-mode theory we now examine a more complex systems involving three dielectric slits separated by some arbitrary

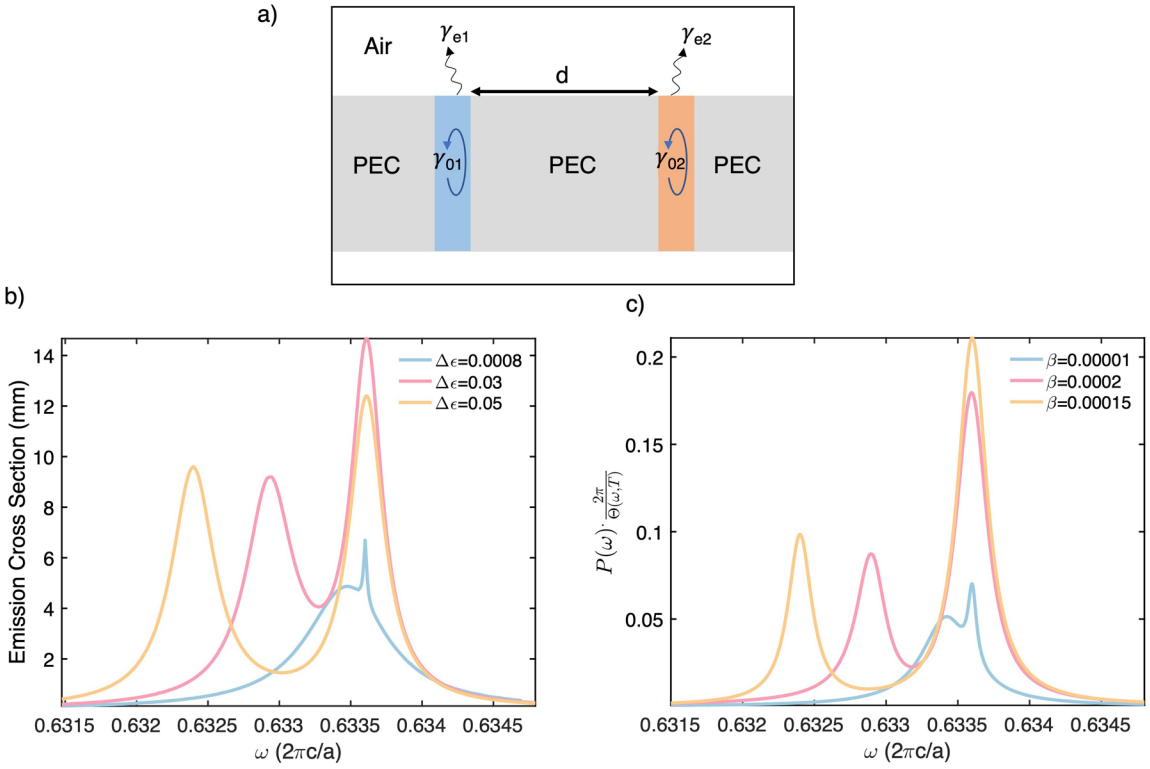

Figure 2. The effect of changing permittivity in one of the two dielectric slits at a fixed, large distance. a) the structure of resonant emitters consisting of two slits in two PEC slabs. The length and width of slit are 1.4 μm wide, and 5 nm, respectively. They are filled with two different dielectric materials with non-zero emissivity that are separated by a constant distance d = 800 nm. b) FDFD-simulated spectra of emission cross section for two resonant emitters. The dielectric constant difference of $\Delta\varepsilon_1 = 0.0008$, $\Delta\varepsilon_2 = 0.03$ and $\Delta\varepsilon_1 = 0.05$ separately. c) Coupled mode

theory thermal emission power prediction for two different emitters with a different imaginary coupling strength of $\beta = 0.00001$, $\beta = 0.0002$, $\beta = 0.00015$.

distance in a finite thickness PEC slab, and filled with dielectric materials of arbitrary permittivity, as is shown in Fig. 3(a). We consider the scenario where the first and third resonators have the same permittivity $\varepsilon_1 = \varepsilon_3 = 12.5 + 0.001i$ while the middle resonator has a slightly different permittivity of $\varepsilon_2 = 12.53 + 0.001i$. In Fig. 3(b), we compare the emission cross section as simulated by FDFD for this three slit resonator systems against a two resonator only system with $\varepsilon_1 = 12.5 + 0.001i$ and $\varepsilon_2 = 12.53 + 0.001i$ and without ε_3. Remarkably, we observe that the addition of the third resonator suppresses the lower frequency peak (associated with ε_1 and ε_3) while greatly enhancing the emission peak associated with the middle resonator (with permittivity ε_2). Coupling between the resonators 1 and 3 results in a super-radiant suppression of emission analogous to that observed in Ref.[44] for the lower frequency peak. However, coupling between resonator 2 and its neighbors results in a dramatic sub-radiant enhancement in its thermal emission peak. We can model both the baseline two resonator, and the more complex three resonator system using the coupled-mode theory and find that it replicates the result observed in the full-wave electromagnetic simulation, as is shown in Fig. 3(c). Our results, in addition to highlighting the capabilities of the coupled-mode theory, show a new mechanism to develop high power, narrow bandwidth thermal emitters through inter-resonator coupling.

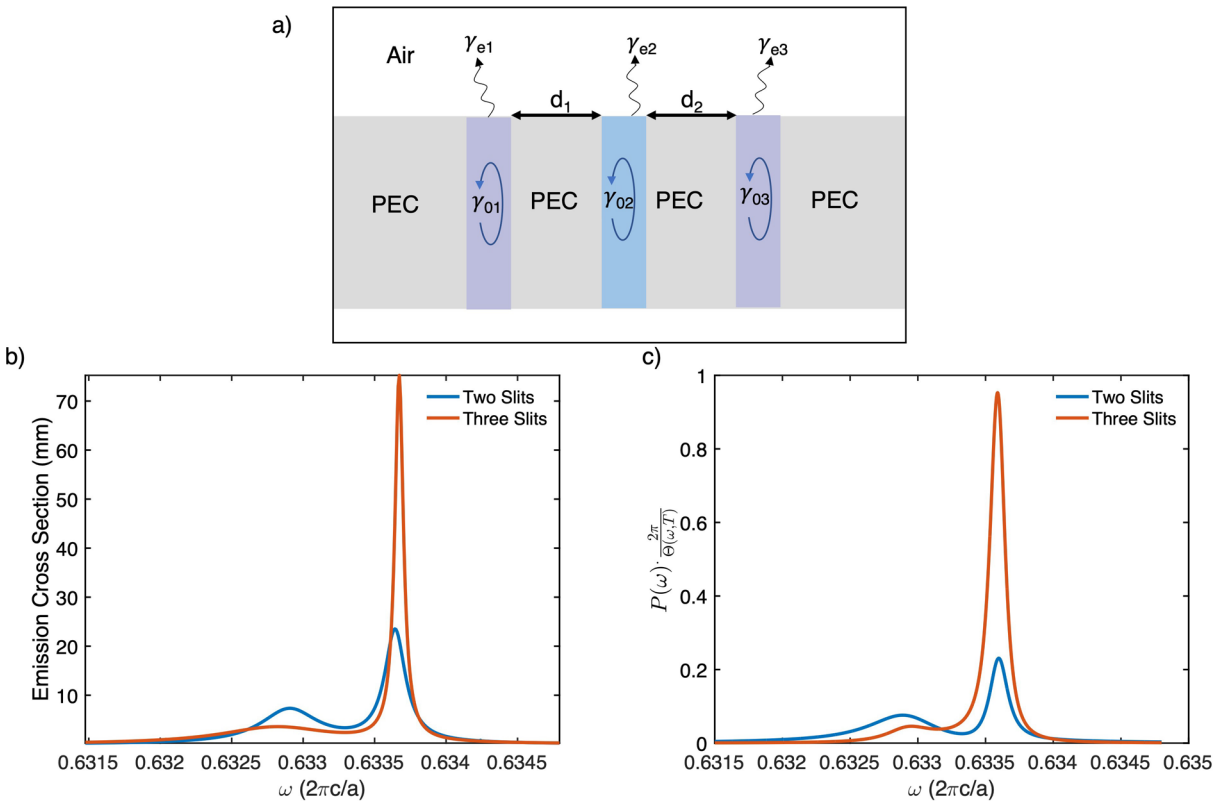

Figure 3. Comparison between two resonant emitters system and three resonant emitters system. a) The structure of resonant emitters consisting of three slits in three PEC slabs. The length and width of the slit are 1.4 μm and 5 nm, respectively. They are filled with three emissive materials. b) FDFD-simulated spectra of emission cross section for two resonators with a permittivity ε_1 = 12.5 + 0.001i and ε_2 = 12.53+0.001i, and for a three resonant emitter scenario where the dielectric permittivities are $\varepsilon_1 = 12.5 + 0.001i$, $\varepsilon_2 = 12.53 + 0.001i$ and $\varepsilon_3 = 12.5 + 0.001i$. c) Coupled mode theory thermal emission power prediction for both the two resonator and three resonator scenarios, showing strong alignment with the numerical simulations of b)

Finally, we demonstrate the ability of the coupled-mode theory to accurately model

thermal emission from complex, three-dimensional nanophotonic structures. In particular we consider complex supercells of metal-insulator-metal (MIM) metasurfaces[9, 45] featuring cross-shaped resonators made of two different noble metals, schematically shown in Fig. 4(a). The structures have $\pi/2$ rotational symmetry and consist of three layers. The top layer consists of a pair of gold metasurface elements, and a pair of silver metasurface elements with arms lengths of $l_1 = 2.5\ \mu$m, $l_2 = 2.1\ \mu$m, and arm widths $w_1 = 0.6\ \mu$m , $w_2 = 0.4\ \mu$m respectively, with a thickness of 0.1 μm. The permittivities of both silver and gold are modeled with a Drude fit that is accurate to the long-wave infrared target wavelength range [46]. The metasurfaces lie atop a 0.2 μm Al_2O_3 layer whose permittivity is defined in our wavelength region of interest with a Drude-Lorentz model $\varepsilon = \varepsilon_\infty - \sigma/(\omega^2 - i\omega\gamma - \omega^2)$, with $\varepsilon_\infty = 2.228$, $\sigma = 0.008385(2\pi c/a)$, $\gamma = 0.04(2\pi c/a)$, and $\omega_0 = 0.08(2\pi c/a)$, where $a = 1\ \mu m$. The bottom layer is assumed to be gold as well at a thickness of 0.2 μm. We performed full-field

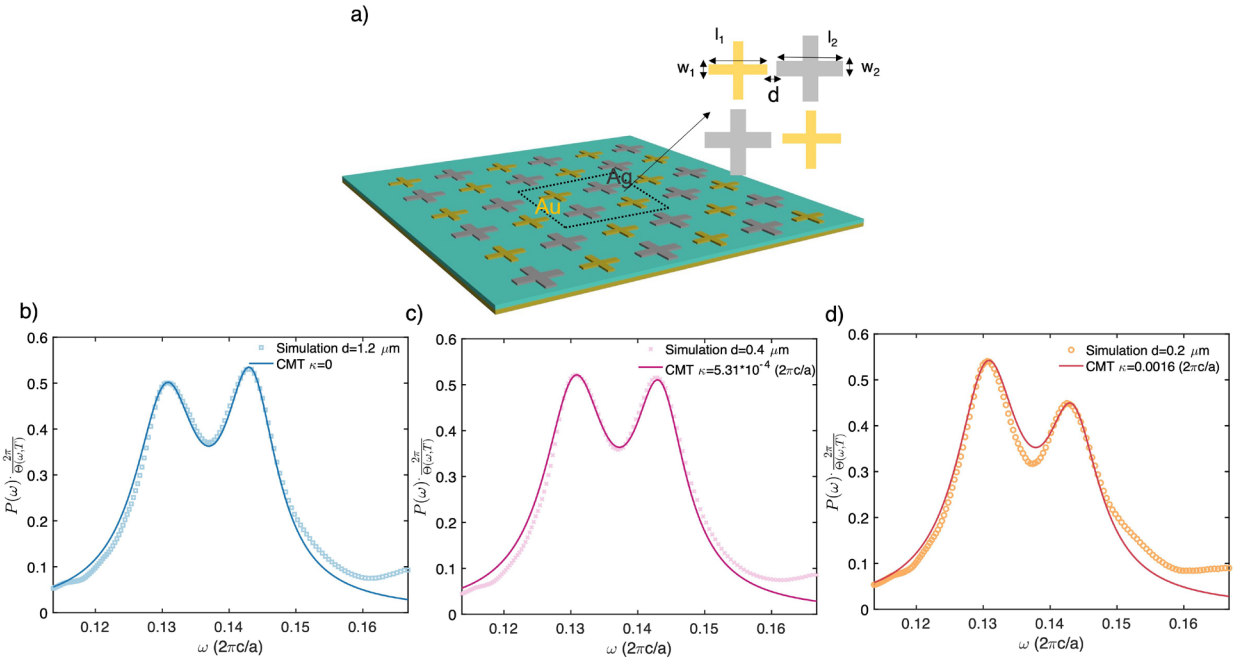

Figure 4. Couple-mode theory predictions vs. full-field simulations of a complex supercell metasurface. a) Geometry of the supercell metasurface architecture evaluated. The metasurface elements have dimensions of $l_1 = 2.5\ \mu$m, $l_2 = 2.1\ \mu$m, and $w_1 = 0.6\ \mu$m , $w_2 = 0.4\ \mu$m respectively, with a layer thickness of 0.1 μm. The central layer is Al_2O_3 with thickness 0.2 μm while the bottom layer is gold with thickness of 0.2 μm. b) Simulation thermal emission power when d=1.2 μm versus analytical coupled-mode theory prediction when κ=0. c) Simulation thermal emission power when d=0.4 μm versus analytical coupled-mode theory prediction when $\kappa=5.31\times 10^{-4}(2\pi c/a)$. d) Simulation thermal emission power when d=0.2 μm versus analytical coupled-mode theory prediction when κ=0.0016 (2πc/a)

electromagnetic simulations of a range of MIM supercell metasurfaces where the distance between the resonators in each supercell is modified, in analogy to the scenario explored in Fig. 1 in a two-dimensional systems. We simulated each geometry across both polarizations and all angles of incidence to calculate the total spectral hemispherical emittance. Given the four-fold symmetry of the supercells, to find the total emitted power we integrate the incident angle θ from 0 to $\pi/2$ at $\pi/12$ step and the azimuth angle φ from 0 to $\pi/4$ with $\pi/12$ steps:

$$\varepsilon(\lambda) = \frac{\int_0^{2\pi}\int_0^{\pi/2} \varepsilon(\lambda,\theta,\phi) cos\theta sin\theta d\theta d\phi}{\int_0^{2\pi}\int_0^{\pi/2} cos\theta sin\theta d\theta d\phi} \tag{12}$$

As shown in Fig. 4(b-d), the simulations show that the supercell structure supports two non-degenerate modes at ω_1=0.131 (2πc/a) and ω_2=0.143 (2πc/a). We then use the coupled- mode theory to fit each resonator's intrinsic decay rate and external decay rate by simulating its hemispherical emittance with a single resonator model, finding γ_{01} = 0.0019 (2πc/a), γ_{02}

= 0.0017 (2πc/a), γ_{e1} = 0.0038 (2πc/a), and γ_{e2}= 0.0030 (2πc/a). As the distance d is varied, the numerically simulated total hemispherical emittance is then compared against the coupled-mode theory predictions and shows remarkably strong agreement, as can be seen in Fig. 4(b-d) for a range of resonator distances. Our results highlight a powerful capability enabled by the coupled-mode theory framework in the context of thermal emission from such complex supercell systems: simulating the response of each metasurface resonator in a periodic configuration provides sufficient information to rapidly model the behavior of complex arrangements of metasurface resonators through the use of the complex coupling coefficients $\boldsymbol{K}$.

2.3 Conclusions

In conclusion, we have developed a coupled mode theory that accurately models thermal emission from complex photonic structures composed of multiple resonators that can be arbitrarily coupled to each other. We demonstrated that the coupled-mode theory accurately models anomalous, complex behavior such as combined sub- and super-radiant thermal emission in a single nanophotonic structure, as well as the response of supercell three-dimensional MIM metasurface thermal emitters. Furthermore, the coupled mode theory provides accurate predictions while taking far less time than full-field simulations which takes hours to simulate[46], and in the process provides physical insight into the original of the complex spectral behavior that can result. Although we only fit our theoretical framework using regular nanophotonic systems, this theory also implies that, once intrinsic decay rate, external decay rate and coupling coefficients for a particular multi-resonator system of interest have been determined, the temporal coupled-mode theory can be utilized as a quick simulator

of thermal emission from the class of complex nanophotonic structures under consideration. As a semi-analytical model, it can provide deeper insight into the effect of material and structural characteristics on the spectral nature of their thermal emission, which simulations alone cannot provide. One can thus imagine building libraries of individual resonator responses which can then rapidly be assessed for their integration into coupled arrangements based on the developed coupled-mode theory. As demands on the complexity of the spectral response of thermal photonic emitters grow, such a framework may prove critical to further enhance and rapidly model their capabilities.

2.4 Supporting Information

Proof of $2(\boldsymbol{\Gamma_0} + \boldsymbol{\Gamma_e} + \boldsymbol{K}) = \boldsymbol{D^+ D}$

The energy is in the resonators varies as

$$\frac{d(\boldsymbol{a}^+\boldsymbol{a})}{dt} = \frac{d\boldsymbol{a}^+}{dt}\boldsymbol{a} + \boldsymbol{a}^+\frac{d\boldsymbol{a}}{dt} = \boldsymbol{a}^+(-i\boldsymbol{\Omega_0} - \boldsymbol{\Gamma_0} - \boldsymbol{\Gamma_e} - \boldsymbol{K})\boldsymbol{a} + \boldsymbol{a}^+(i\boldsymbol{\Omega_0} - \boldsymbol{\Gamma_0} - \boldsymbol{\Gamma_e} - \boldsymbol{K})\boldsymbol{a} =$$

$$-2\boldsymbol{a}^+(\boldsymbol{\Gamma_0} + \boldsymbol{\Gamma_e} + \boldsymbol{K})\,\boldsymbol{a} \tag{1}$$

Because the entire system, including the resonator and the ports, is energy efficient, the decaying of the resonance amplitudes is solely related to the generation of the outgoing waves. Hence

$$\frac{d(\boldsymbol{a}^+\boldsymbol{a})}{dt} = -\boldsymbol{a}^+\boldsymbol{D}^+\boldsymbol{D}\boldsymbol{a} \tag{2}$$

Here we assume that all the resonance in the cavity can decay into all the ports. D is the coupling matrix with all the ports

$$\boldsymbol{D} = \begin{pmatrix} d_{11} & d_{12} & \cdots & d_{1(N-1)} & d_{1N} \\ d_{21} & d_{22} & \cdots & d_{2(N-1)} & d_{2N} \\ \vdots & & \ddots & & \vdots \\ d_{(N-1)1} & d_{(N-1)2} & \cdots & d_{(N-1)(N-1)} & d_{(N-1)N} \\ d_{N1} & d_{N2} & \cdots & d_{N(N-1)} & d_{NN} \end{pmatrix} \tag{3}$$

Therefore, we have

$$2(\boldsymbol{\Gamma_0} + \boldsymbol{\Gamma_e} + \boldsymbol{K}) = \boldsymbol{D}^{+}\boldsymbol{D} \tag{4}$$

We consider a resonator system with two resonances and two physical ports, as an example of the general theory. Ω_0 describes the resonant frequency of each resonator.

$$\boldsymbol{\Omega_0} = \begin{pmatrix} \omega_1 & 0 \\ 0 & \omega_2 \end{pmatrix} \tag{5}$$

Γ_0 describe the intrinsic decay rate,

$$\boldsymbol{\Gamma_0} = \begin{pmatrix} \gamma_{01} & 0 \\ 0 & \gamma_{02} \end{pmatrix} \tag{6}$$

and Γ_e describe the external decay rate,

$$\boldsymbol{\Gamma_e} = \begin{pmatrix} \gamma_{e1} & 0 \\ 0 & \gamma_{e2} \end{pmatrix} \tag{7}$$

The two emitters couple with each other and complex coupling matrix K is defined as

$$\boldsymbol{K} = \begin{pmatrix} 0 & \kappa_{12} + jb_{12} \\ \kappa_{21} + jb_{21} & 0 \end{pmatrix} \tag{8}$$

κ_{12} is the real part of coupling strength, determined by the spatial distance between the resonators and b_{12} is the imaginary part of coupling strength, representing the phase difference. Here we assume that all the resonance in the cavity can decay into all the ports and

D id the coupling matrix with all the ports

$$\boldsymbol{D} = \begin{pmatrix} d_{11} & d_{12} \\ d_{21} & d_{22} \end{pmatrix} \tag{9}$$

By applying our general energy conservation equation shown in Eq.(4) into two resonators system, we can get:

$$\begin{pmatrix} d_{11}^2 + d_{21}^2 & d_{11}d_{12} + d_{21}d_{22} \\ d_{12}d_{11} + d_{22}d_{21} & d_{12}^2 + d_{22}^2 \end{pmatrix} = \begin{pmatrix} 2(\gamma_{01} + \gamma_{e1}) & 2\kappa_{12} \\ 2\kappa_{21} & 2(\gamma_{02} + \gamma_{e2}) \end{pmatrix} \tag{10}$$

By solving the Eq.(10), we can have

$$|d_{11}| = |d_{21}| = \sqrt{\gamma_{01} + \gamma_{e1}} \tag{11}$$

$$|d_{12}| = |d_{22}| = \sqrt{\gamma_{02} + \gamma_{e2}} \tag{12}$$

$$\exp(j\theta_{12} - j\theta_{11}) + exp(j\theta_{22} - j\theta_{21}) = \frac{2\kappa_{12} + 2jb_{12}}{\sqrt{(\gamma_{01}+\gamma_{e1})(\gamma_{02}+\gamma_{e2})}} \tag{13}$$

$$\cos(\theta_{12} - \theta_{11}) + isin(\theta_{12} - \theta_{11}) + \cos(\theta_{22} - \theta_{21}) + i\,sin(\theta_{22} - \theta_{21}) = \frac{2\kappa_{12} + 2jb_{12}}{\sqrt{(\gamma_{01}+\gamma_{e1})(\gamma_{02}+\gamma_{e2})}}$$

(14)

Expression for the three resonator (N=3) scenario

For three resonators (N=3), if we only include the real part of coupling terms κ_{ij}, the radiated power is expressed as follows:

$$P(\omega) = \frac{\Theta(\omega,T)}{6\pi} \frac{1}{(\alpha_1\alpha_2\alpha_3 - \alpha_1\kappa_{32}\kappa_{23} - \kappa_{21}\kappa_{12}\alpha_3 + \kappa_{13}\kappa_{21}\kappa_{32} + \kappa_{31}\kappa_{12}\kappa_{23})^2} \times [4\gamma_{01}\gamma_{e1}(\alpha_2\alpha_3 - \kappa_{32}\kappa_{23})^2 +$$

$$4\gamma_{02}\gamma_{e2}(\alpha_1\alpha_3 - \kappa_{13}\kappa_{31})^2 + 4\gamma_{03}\gamma_{e3}(\alpha_1\alpha_2 - \kappa_{21}\kappa_{12})^2 + 4\gamma_{02}\gamma_{e1}(\kappa_{13}\kappa_{32} - \kappa_{12}\alpha_3)^2 +$$

$$4\gamma_{03}\gamma_{e1}(\kappa_{12}\kappa_{23} - \kappa_{13}\alpha_2)^2 + 4\gamma_{01}\gamma_{e2}(\kappa_{23}\kappa_{31} - \kappa_{21}\alpha_3)^2 + 4\gamma_{03}\gamma_{e2}(\kappa_{21}\kappa_{13} - \kappa_{23}\alpha_1)^2 +$$

$$4\gamma_{01}\gamma_{e3}(\kappa_{21}\kappa_{32} - \kappa_{31}\alpha_2)^2 + 4\gamma_{02}\gamma_{e3}(\kappa_{12}\kappa_{31} - \kappa_{32}\alpha_1)^2 \tag{15}$$

Here for convenience we have introduced variables α_j defined as:

$$\alpha_j = i\left(\omega - \omega_j\right) + \gamma_{0j} + \gamma_{ej} \tag{16}$$

Proof of $\langle \boldsymbol{n}^*(\boldsymbol{\omega})\boldsymbol{n}(\boldsymbol{\omega}')\rangle = \frac{\mathbf{1}}{\mathbf{2N\pi}}\boldsymbol{\Theta}(\boldsymbol{\omega}, \boldsymbol{T})\boldsymbol{\delta}(\boldsymbol{\omega} - \boldsymbol{\omega}')$

We assume that the noise source is stationary and that each resonator has the same thermal noise. We can thus define a correlation function in terms of a response [43]:

$$\langle \boldsymbol{n}^*(\omega)\boldsymbol{n}(\omega')\rangle = S(\omega)\delta(\omega - \omega') \tag{17}$$

If we then express the time-domain norm of the amplitudes in terms of their frequency domain counterparts, we can then use the expression for n above and the main coupled-mode theory expression in Eq. (3) of the main article to find:

$$\langle \boldsymbol{a}^*(t)\boldsymbol{a}(t)\rangle = \int_0^\infty \boldsymbol{d\omega} \int_0^\infty \boldsymbol{d\omega' e^{-j(\omega-\omega')t}} \langle \boldsymbol{a}^*(\omega)\boldsymbol{a}(\omega')\rangle = \int_0^\infty \boldsymbol{d\omega} \int_0^\infty \boldsymbol{d\omega'} ((j(\omega - \boldsymbol{\Omega_0}) + \boldsymbol{\Gamma_0} + \boldsymbol{K})^{-1})^2 2\boldsymbol{\Gamma_0 S}(\boldsymbol{\omega})\boldsymbol{\delta}(\boldsymbol{\omega} - \boldsymbol{\omega}') = \int_0^\infty \boldsymbol{d\omega} ((j(\omega - \boldsymbol{\Omega_0}) + \boldsymbol{\Gamma_0} + \boldsymbol{K})^2 2\boldsymbol{\Gamma_0}\, \boldsymbol{S}(\boldsymbol{\omega}) \tag{18}$$

If we assume that the noise source is sufficiently broadband $S(\omega)$ in the integrand above can then be replaced, without loss of generality, by $S(\langle\Omega_0\rangle)$. This then allows us to solve for the integral, where we find that

$$\langle \boldsymbol{a}^*(t)\boldsymbol{a}(t)\rangle = \mathbf{2N\pi S}(\langle \boldsymbol{\Omega_0}\rangle) \tag{19}$$

At thermal equilibrium the modal amplitudes must relate to the Planck term as:

$$\langle \boldsymbol{a}^*(t)\boldsymbol{a}(t)\rangle = \boldsymbol{\Theta}(\langle \boldsymbol{\Omega_0}\rangle, \boldsymbol{T}) \tag{20}$$

Comparing Eqs. (19) and (20), we have $\boldsymbol{S}(\langle \boldsymbol{\Omega_0}\rangle) = \frac{1}{2N\pi}\boldsymbol{\Theta}(\langle \boldsymbol{\Omega_0}\rangle, T)$. However, since this derivation can be carried out for resonances at any arbitrary resonant frequency$\langle \boldsymbol{\Omega_0}\rangle$,we have

$\boldsymbol{S(\omega)} = \frac{1}{2N\pi}\boldsymbol{\Theta}(\omega, T)$.

2.5 References

1. V. Shchegrov, K. Joulain, R. Carminati, and J.-J. Greffet, Phys. Rev. Lett. **85**, 1548 (2000).

2. M. U. Pralle, N. Moelders, M. P. McNeal, I. Puscasu, A. C. Greenwald, J. T. Daly, E. A.

3. Johnson, T. George, D. S.Choi, I. El-Kady, and R. Biswas, Appl. Phys. Lett. **81**, 4685 (2002).

4. J.-J. Greffet, R. Carminati, K. Joulain, J.-P. Mulet, S. Mainguy, and Y. Chen, Nature **416**, 61 (2002).

5. Celanovic, D. Perreault, and J. Kassakian, Phys. Rev. B **72**, 075127 (2005).

6. M. Laroche, C. Arnold, F. Marquier, R. Carminati, J.-J. Greffet, S. Collin, N. Bardou, and J.-L. Pelouard, Opt. Lett. **30**, 2623 (2005).

7. J. Lee, C. J. Fu, and Z. M. Zhang, Appl. Phys. Lett. **87**, 071904 (2005).

Puscasu and W. L. Schaich, Appl. Phys. Lett. **92**, 233102 (2008).

8. S. Shen, A. Narayanaswamy, and G. Chen, Nano Lett. **9**, 2909 (2009).

9. X. Liu, T. Tyler, T. Starr, A. F. Starr, N. M. Jokerst, and W. J. Padilla, Phys. Rev. Lett.**107**, 045901 (2011).

10. Liu, W. Gong, B. Yu, P. Li, and S. Shen, Nano Lett **17**, 666 (2017).

11. S.-Y. Lin, J. G. Fleming, E. Chow, K. K. C. J. Bur, and A. Goldberg, Phys. Rev. B **62**, R2243 (2000).

12. Luo, A. Narayanaswamy, G. Chen, and J. D. Joannopoulos, Phys.Rev.Lett. **93**, 213905 (2004).

13. S. Y. Lin, J. Moreno, and J. G. Fleming, Appl.Phys.Lett. **83**, 380 (2003).

14. T. Inoue, M. D. Zoysa, T. Asano, and S. Noda, Nat. Mater. **13**, 928 (2014).

15. C. M. Cornelius and J. P. Dowling, Phys. Rev. A **59**, 4736 (1999).

16. M. D. Zoysa, T. Asano, K. Mochizuki, A. Oskooi, T. Inoue, and S. Noda, Nat. Photonics **6(8)**, 535 (2012).

17. J. A. Mason, S. Smith, and D. Wasserman, Appl.Phys. Lett. **98**, 241105 (2011).

18. Y. Guo and S. Fan, Opt. Express **24**, 29896 (2016).

19. S. Narayanaswamy and G. Chen, Appl. Phys. Lett. **82**, 3544 (2003).

20. P. Nagpal, S. E. Han, A. Stein, and D. J. Norri, Nano Lett. **8**, 3238 (2008).

21. Rephaeli and S. Fan, Opt. Express **17**, 15145 (2009).

22. R. Messina and P. Ben-Abdallah, Sci. Rep. **3**, 1383 (2013).

23. Lenert, D. M. Bierman, W. R. C. Y. Nam, M. S. c. I. Celanovic, and E. N. Wang, Nat. Nanotechnol. **9**, 126 (2014).

24. P. Raman, M. A. Anoma, L. Zhu, E. Rephaeli, and S. Fan, Nature **515**, 540–544 (2014).

25. Z. Chen, L. Zhu, A. P. Raman, and S. Fan, Nat. Commun. **7**, 13729 (2016).

26. J. Kou, Z. Jurado, Z. Chen, and S. Fan, ACS Photonics **4(3)**, 626 (2017).

27. M. M. Hossain, B. Jia, and M. Gu, Adv. Opt. Mater. **3(8)**, 1047 (2015).

28. N. N. Shi, C. C. Tsai, F. Camino, G. D. Bernard, N. Yu, and R. Wehner, Science **349(6245)**, 298 (2015).

29. R. Gentle and G. B. Smith, Adv Sci **2(9)**, 1500119 (2015).

30. A. Goldstein, A. P. Raman, and S. Fan, Nat. Energy **2(9)**, 17143 (2017).

31. P. C. Hsu, A. Y. Song, P. B. Catrysse, C. Liu, Y. Peng, J. Xie, S. Fan, and Y. Cui, Science **353(6303)**, 1019 (2016).

32. J. K. Tong, X. Huang, S. V. Boriskina, J. Loomis, Y. Xu, and G. Chen, ACS Photonics **2(6)**, 769 (2015).

33. P. B. Catrysse, A. Y. Song, and S. Fan, ACS Photonics **3(12)**, 2420 (2016).

34. S. Jafar-Zanjani, M. M. Salary, and H. Mosallaei, ACS Photonics **4(4)**, 915 (2017).

35. Haus, *Waves and Filed in Optoelectronics* (Prentice Hall,Englewood Cliffs, NJ, 1984).

36. W. Suh, Z. Wang, and S. Fan, IEEE J. Quantum Electron **40(10)**, 1511 (2004).

37. M. J. Khan, C. Manolatou, S. Fan, P. R. Villeneuve, H. A. Haus, and J. D. Joannopoulos, IEEE J. Quantum Electron **35(10)**, 1451 (1999).

38. H.-C. Liu and A. Yariv, Opt. Express **19(18)**, 17653 (2011).

39. S. Fan, W. Suh, and J. D. Joannopoulos, J. Opt. Soc. Am. A **20(3)**, 569 (2003).

40. M. F. Yanik and S. Fan, Phys. Rev. Lett. **92(8)**, 083901 (2004).

41. D. M. Ramirez, A. W. Rodriguez, H. Hashemi, J. D. Joannopoulos, M.Soljacic, and S. G. Johnson, Phys. Rev. A **83(3)**, 033834 (2011).

42. M. Ghebrebrhan, P. Bermel, Y. X. Yeng, I. Celanovic, M. Soljačić, and J. D. Joannopoulos, Phys. Rev. A **83**, 033810 (2011).

43. L. Zhu, S. Sandhu, C. Otey, S. Fan, M. B. Sinclair, and T. S. Luk, Appl.Phys. Lett **102**, 103104 (2013).

44. M.Zhou, S. Yi, T. S. Luk, Q. Gan, S. Fan, and Z. Yu, Phys. Rev.B **92**, 024302 (2015).

45. Yeung, J. M. Tsai, B. King, B. Pham, D. Ho, J. Liang, M. W. Knight, and A. P. Raman, Nanophotonics **10**, 3 (2021).

46. M. A. Ordal, L. L. Long, R. J. Bell, S. E. Bell, R. R. Bell, R. W. Alexander, and C. A. Ward, Appl. Opt. **22**, 1099 (1983).

Chapter 3: Low-cost scalable radiative cooling material

3.1 Introduction

Passive radiative cooling, which involves net heat loss from terrestrial objects to the cold of outer space through long wavelength infrared (LWIR, λ ~8-13 μm) transmission windows of the atmosphere, is a zero-energy, zero-carbon method of cooling objects under the sky. In recent years, it has been increasingly explored[1–12] as an alternative or complement to active cooling methods for a range of applications, including cooling buildings[13], harvesting dew[14–16] and thermoelectric power generation[17]. A variety of materials and designs, ranging from photonic architectures[18] to scalable polymer films[19–21], paints[22,23] and composites[24] have been created for radiative cooling. These materials and designs are capable of efficient radiative cooling and are typically suited to specific applications. However, simplicity of design, and ease of application remain a major research endeavor – both for scientific and large-scale use. Low cost radiative coolers[25] have attracted much attention recently with the possibility of greatly expanding the scope of radiative cooling's deployment.

In this chapter, we demonstrate an easily fabricable and efficient radiative cooling design made using household materials. The radiative cooler, which can be made from scotch tape and aluminum foil and has excellent infrared optical characteristics for radiative cooling: selective LWIR emittance (ε_{LWIR}, emittance in the 8-13 μm (LWIR) wavelength range) of 0.87 at near-normal incidence and hemispherical selective LWIR emittance of 0.83. Furthermore it is flexible, robust, scalable and low-cost. The total broadband emittance ε_{BB} of scotch tape is 0.68 at near-normal incidence and its hemispherical broadband emittance is 0.63. The back aluminum foil yields a modest weighted solar reflectance at 0.83. If silver is used as a back-reflector, the design's high solar reflectance (R_{solar}~0.95) makes it capable of daytime radiative cooling as well. We

experimentally demonstrate a sub-ambient cooling by 11 ℃ at night with a convection shield, and daytime cooling performance with a 2 ℃ drop under a solar illumination of 965Wm^{-2} without one. Given that the design has high optical performance, and is created using standard commercially available materials, we argue that this makes it attractive as a convenient and reproducible standard – both for designs that require a generic radiative cooling component for their operation, and as a control for radiative cooling experiment. In that regard, its high LWIR emittance, along with the modest directional LWIR selectivity at near normal incidence, defined as $\frac{\varepsilon_{LWIR}(near\ normal\ incidence)}{\varepsilon_{BB}(near\ normal\ incidence)}$ of 1.28, and hemispherical LWIR selectivity, defined as $\frac{\varepsilon_{LWIR}(hemispherical)}{\varepsilon_{BB}(hemispherical)}$ of 1.32. The intermediate nature of its selectivity may also make it useful as a reference threshold between broadband and selective radiative coolers. Towards these ends, we provide extensive optical characterization for the radiative cooling research community to use as a reference.

3.2 Results and Discussion

We investigated scotch-tape based radiative cooling designs because of their readily reproducible optical performance, which arises from their standardized material constituents. To achieve passive radiative cooling, a radiative cooling design should have a high emittance ε in the LWIR atmospheric transmission window (λ~8-13 μm), and a high R_{solar} for sub-ambient cooling during the day. In that regard, certain variants of scotch tapes, which comprise acrylic adhesive on a polypropylene film, are intuitive choices (Fig. 1A). Both acrylic and polypropene have chemical bonds which absorb, and hence radiate heat in the LWIR wavelengths, which can be lose to space (Fig. 1B). A lack of highly emissive chemical bonds in the non-LWIR thermal wavelengths makes sufficiently thin films of both materials selectively LWIR emissive. The 3M Long Lasting Scotch

Tape, which we propose for use here, combines both these properties in a standardized and reproducible manner.

As an infrared reflector for the scotch tape, we use commercial aluminum foil, which, regardless of the commercial source, has minimal variation in LWIR reflectance. A design comprising 2 layers of tape on aluminum foil has spectral reflectance shown in Fig. 1C for near-normal incidence. The ultra-wide bandwidth spectral measurements were taken using a Perkin Elmar Lambda 950 spectrophotometer and a directional selectivity of 1.28, and a modest R_{solar} of 0.83. If sputter-coated silver is used instead of aluminum, the solar reflectance rises to 0.95 (Fig. 1C).

The optical performance we highlight here, even without considering the simplicity of the design, is noteworthy in two ways. First, the scotch-tape based design combines a moderately selective infrared emittance with a reasonably high, near-normal ε_{LWIR}. This makes it useful as a night time radiative cooler, and while not a sub-ambient radiative cooling design under strong sunlight, a point of reference nonetheless for experiments involving other radiative coolers. Secondly, when backed with sputter-coated silver, its solar reflectance (0.95) is sufficiently high for daytime radiative cooling under most meteorological conditions (Fig. 1C). The optical parameters of this radiative cooler design are thus quite good, and rank highly among known designs.

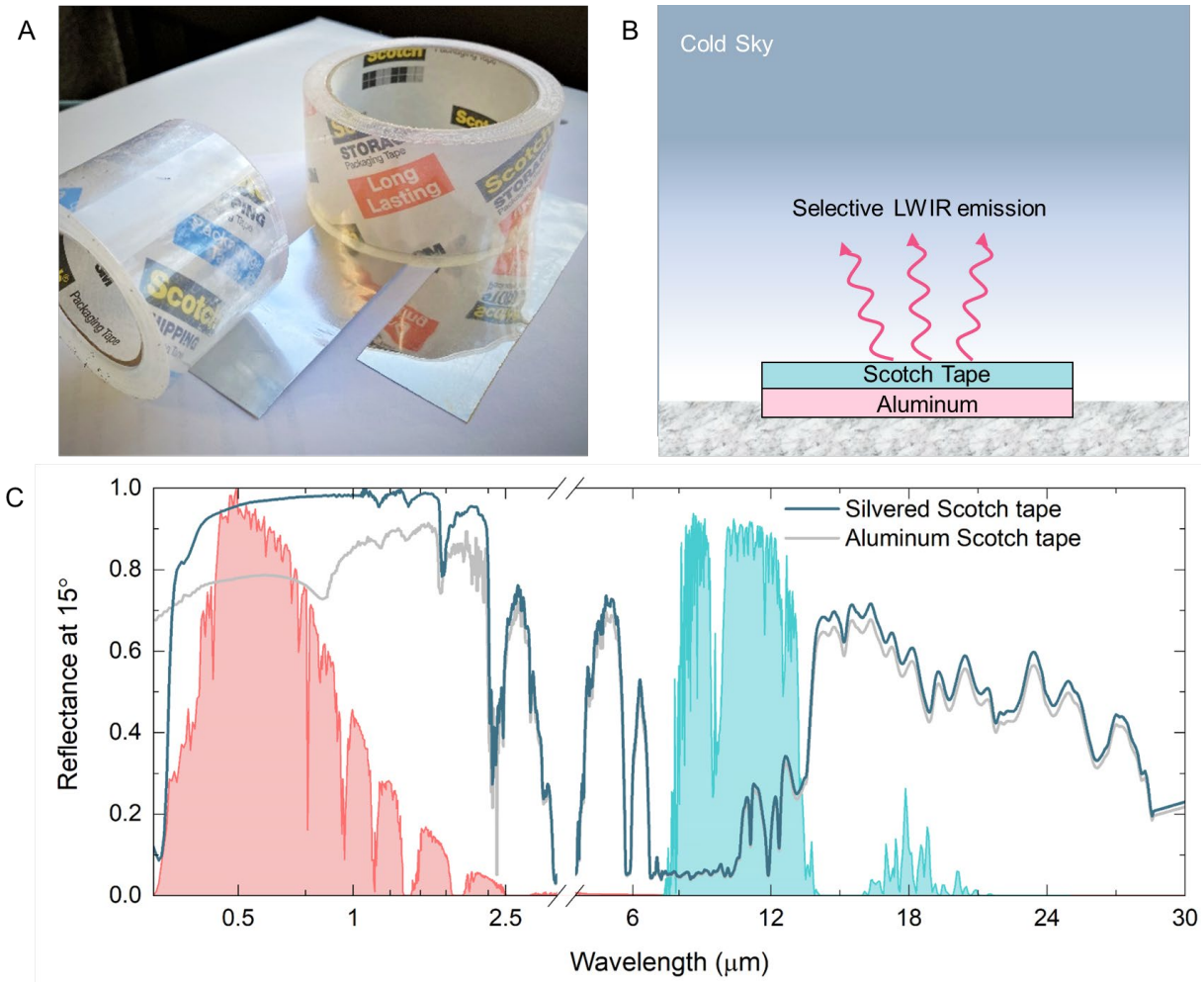

Figure 1. A) Photo of silvered scotch tape. Two-layer scotch tape is coated with silver on the bottom. B) Schematic of the scotch tape radiative cooler with aluminum. C) Reflectance of silvered scotch tape and aluminized scotch tape at 15° incident angle.

A more detailed picture of the scotch tape's radiative capabilities is revealed by the hemispherical emittance (Fig. 2A) derived from angular measurements (Fig. 2B) of reflectance at 15° to 84° using a Harrick Reflectance measurement accessory coupled with an FTIR (Bruker Invenio-R), and averaged using Eq. (1).

$$\varepsilon_\lambda = \frac{\int_0^{2\pi}\int_0^{\pi/2} \varepsilon_{\lambda,\theta}(\lambda,\theta,\varphi)\cos\theta\sin\theta d\theta d\varphi}{\int_0^{2\pi}\int_0^{\pi/2} \cos\theta\sin\theta d\theta d\varphi} \quad (1)$$

We observe that scotch tape has a hemispherical emittance in the LWIR atmospheric window that is high (0.83) and selective. It is difficult for us to compare the performance directly with similar polymer films in the literature as data is scarce. However, we note that it compares favorably with the hemispherical emittance of a highly scalable polymer based radiative cooler (~0.80) proposed by Angus and Gentle[19], and that of our reproduction of metallized polyvinyl chloride (0.73), which was the first polymeric radiative cooler demonstrated by Trombe[21] (Fig. 2A). The ε_{LWIR} of scotch tape persists at high angles, as shown in Fig. 2(C), which enables it to lose heat through the spatial extent of the LWIR window, which only closes near the horizontal.

We also investigate the scotch tape's performance relative to notable broadband emitter and selective emitters in the literature (Fig. 2D). The ε_{LWIR} of scotch tape at near normal incidence is 0.87, which is fairly high, while its directional selectivity at near normal incidence is 1.28, which appears to fall between highly selective[18,21] and broadband designs.[3,19,22] It should be noted here that the performances compared are for near-normal emittances. Further data is provided in an online archive.[26]

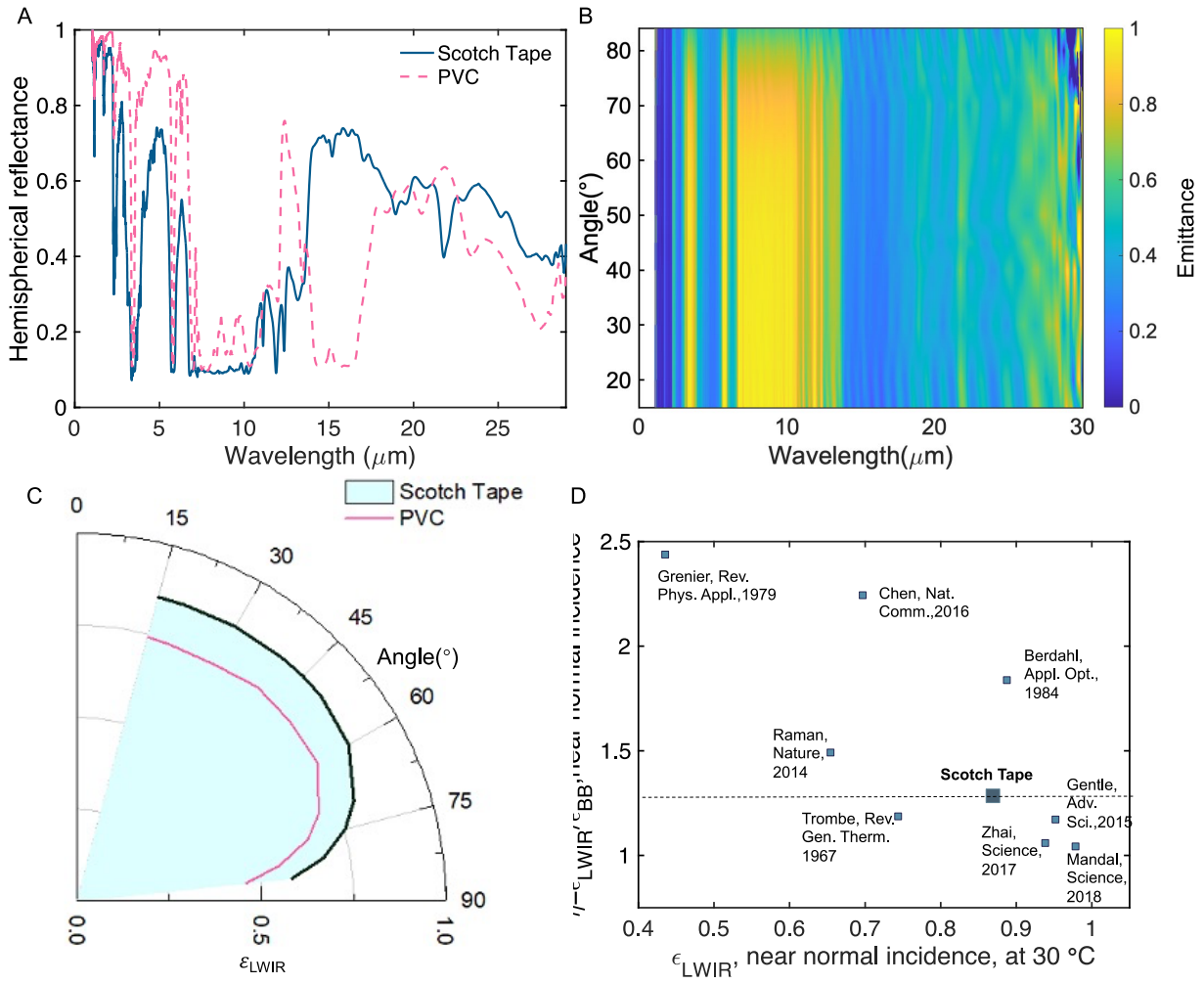

Figure 2. (A) Spectral reflectance $\boldsymbol{R(\lambda)=1-\varepsilon(\lambda)}$ of the silvered scotch-tape radiative cooler, presented alongside that of metallized PVC proposed by Trombe. (B) Emittance of the silvered scotch-tape radiative cooler from 15° to 84° (C) Angular emittance (=1-Reflectance) of the two designs in Fig. 2A. (D) ε_{LWIR} and $\boldsymbol{\eta}$ of silvered scotch-tape radiative cooler compared against notable designs in the literature[3,18–22,27,28].

The optical parameters, which are suitable for radiative cooling, lead to good radiative cooling performance during both day and night. Daytime performance of scotch tape is demonstrated by exposing it directly under the sun in Los Angeles, California on Mar 27th, 2021, as is shown in Fig. 3(A). The scotch tape can maintain a 2-3 ℃ temperature drop compared with the ambient air temperature under 965 W/m^2 solar radiation. We also demonstrate the nighttime performance of the scotch tape in Los Angeles, California on Jan 20th, 2021 by exposing it to the sky during night-time hours and testing its performance compared with the broadband thermal emitter, double-layer white paper. As shown in the temperature data of Fig. 3(B), immediately after the scotch tape is exposed to the environment (20:26 local time in Fig. 3(B)), its temperature drops to approximately 11 ℃ below the measured ambient air temperature. Compared with the white paper, which is a broadband emitter with an emittance of ~0.9, the scotch tape is 1 ℃ cooler despite its lower hemispherical emittance, because of its LWIR selectivity that reduces parasitic heat gain form the atmosphere.

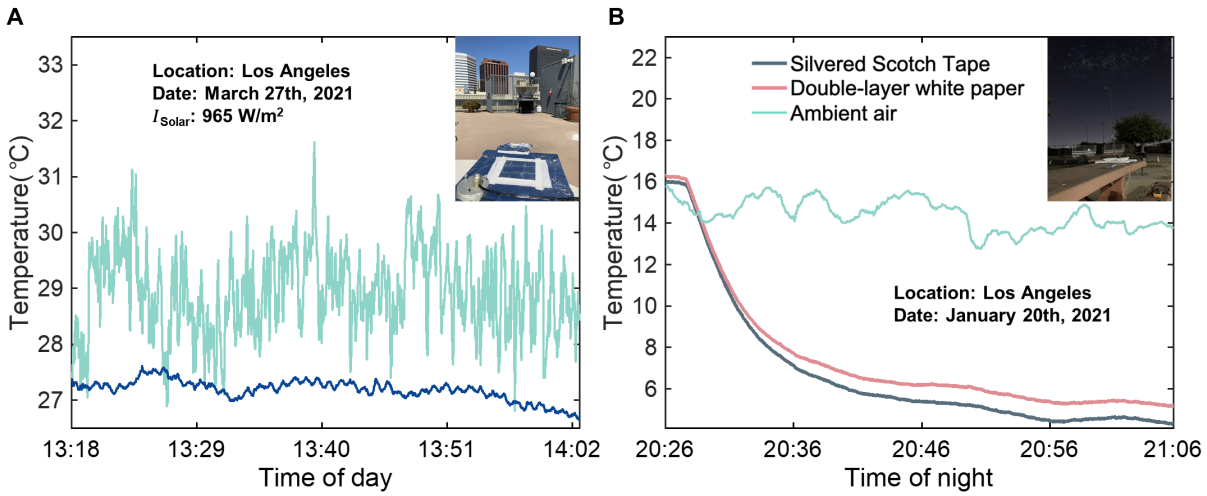

Figure 3. A) Measurement of the silvered scotch tape's temperature(blue) against ambient air temperature (green) on a clear day in Los Angeles, California, USA , March 27th, 2021. Solar radiation: 965 W/m^2

B) Measurement of the silvered scotch tape's temperature (blue) and double-layer white paper's temperature (pink) against ambient air temperature (green) on a clear night in Los Angeles, California, USA, January 20th, 2021.

3.3 Conclusions

To summarize, we have characterized and demonstrated the optical performance of a scotch tape-based radiative cooler, which can be deployed at scale for passive cooling applications. With the scotch tape and aluminum foil, it can have a 11 ℃ temperature drop compared with ambient temperature during night, which makes it useful for cooling down the objects and generating electricity using this temperature difference. A large temperature drop can be achieved by having good insulation. The silvered scotch tape can be used for daytime cooling with a 2-3 ℃ temperature drop, which could make it a good candidate for applications requiring modest cooling below the ambient.

Unlike other approaches to making radiative coolers, which require new or expensive materials and fabrication techniques, scotch tape can be directly applied on the aluminum foil at low cost. Furthermore, the mass production and wide availability of scotch tape makes it a reliable standard as a thermal emitter, and coupling it with commercial aluminum foil or vapor deposited silver makes it into a reproducible radiative cooler that could be used to standardize outdoor radiative cooling experiments. This stands in contrast to other commonly used radiative cooling

polymers like PDMS,[4,29] which are efficient radiative coolers but are hard to coat or otherwise apply in a reproducible manner. Therefore, we propose that:

1. It can be used as a standard reference radiative cooler – with the aluminized version being sufficient as a generic radiative cooling standard, and the silvered version being a standard for sub-ambient daytime applications. The low cost and easy fabrication of such a standard could allow it to easily be used by researchers and practitioners as a control in outdoor experiments. It should be noted that while the aluminized version can be made using standard commercial materials and is thus highly reproducible, the silvered variant's solar reflectance may depend on the silver deposition process, and requires a high quality, optically thick (>200 nm) coating.
2. Because there currently exist no clear boundaries delineating selective and broadband thermal emitters, we propose that the scotch tape radiative cooler could serve as a threshold of selectivity. Materials with selective emittance ratios higher than that of scotch tape can be considered at the selective thermal emitters, while others as broadband thermal emitters.
3. It can be used as an easily fabricable radiative cooler for investigations where a radiative cooling material itself is not central to the study. Potential examples of this include thermoelectricity generation, dew collection or desalination using radiative cooling, where metallized scotch tape can be used as a cooling component.

Towards these ends, we have shown the full spectrum ranging from 0.3 μm to 30 μm for silvered and aluminized scotch tapes, and angular emittances for 15° to 84° for use as a reference. The data, which, to our knowledge, represents the most extensive characterization of a radiative cooler, is

publicly available online.[30,31] The data can also be used for theoretical simulations of radiative coolers. With radiative cooling emerging as an important frontier for research, we hope that this work can offer a potential standard control for other radiative coolers and radiative cooling experiments.

3.4 References

1. Zhu, L., Raman, A. & Fan, S. Color-preserving daytime radiative cooling. *Appl. Phys. Lett.* **103**, 223902 (2013).

2. Zhu, L., Raman, A. P. & Fan, S. Radiative cooling of solar absorbers using a visibly transparent photonic crystal thermal blackbody. *Proc. Natl. Acad. Sci.* **112**, 12282–12287 (2015).

3. Zhai, Y. *et al.* Scalable-manufactured randomized glass-polymer hybrid metamaterial for daytime radiative cooling. *Science* **355**, 1062–1066 (2017).

4. Kou, J., Jurado, Z., Chen, Z., Fan, S. & Minnich, A. J. Daytime Radiative Cooling Using Near-Black Infrared Emitters. *ACS Photonics* **4**, 626–630 (2017).

5. Goldstein, E. A., Raman, A. P. & Fan, S. Sub-ambient non-evaporative fluid cooling with the sky. *Nat. Energy* **2**, 17143 (2017).

6. Bhatia, B. *et al.* Passive directional sub-ambient daytime radiative cooling. *Nat. Commun.* **9**, 5001 (2018).

7. Kim, H. & Lenert, A. Optical and thermal filtering nanoporous materials for sub-ambient radiative cooling. (2018) doi:10.1088/2040-8986/AACAA1.

8. Zhao, D. *et al.* Subambient Cooling of Water: Toward Real-World Applications of Daytime Radiative Cooling. *Joule* **3**, 111–123 (2019).

9. Yang, P., Chen, C. & Zhang, Z. M. A dual-layer structure with record-high solar reflectance for daytime radiative cooling. *Sol. Energy* **169**, (2018).

10. Zhao, B., Hu, M., Ao, X., Chen, N. & Pei, G. Radiative cooling: A review of fundamentals, materials, applications, and prospects. *Appl. Energy* **236**, 489–513 (2019).

11. Harrison, A. W. & Walton, M. R. Radiative cooling of TiO2 white paint. *Sol. Energy* **20**, 185–188 (1978).

12. Hjortsberg, A. & Granqvist, C. G. Radiative cooling with selectively emitting ethylene gas. *Appl. Phys. Lett.* **39**, 507–509 (1981).

13. Mandal, J., Mandal, S., Brewer, J., Ramachandran, A. & Raman, A. P. Radiative Cooling and Thermoregulation in the Earth's Glow. *ArXiv200611931 Phys.* (2021).

14. Li, W. *et al.* Nighttime Radiative Cooling for Water Harvesting from Solar Panels. *ACS Photonics* **8**, 269–275 (2021).

15. Zhou, M. *et al.* Vapor condensation with daytime radiative cooling. *Proc. Natl. Acad. Sci.* **118**, (2021).

16. Haechler, I. *et al.* Exploiting radiative cooling for uninterrupted 24-hour water harvesting from the atmosphere. *Sci. Adv.* **7**, eabf3978 (2021).

17. Raman, A. P., Li, W. & Fan, S. Generating Light from Darkness. *Joule* **3**, 2679–2686 (2019).

18. Raman, A. P., Anoma, M. A., Zhu, L., Rephaeli, E. & Fan, S. Passive radiative cooling below ambient air temperature under direct sunlight. *Nature* **515**, 540–544 (2014).

19. Gentle, A. R. & Smith, G. B. A Subambient Open Roof Surface under the Mid-Summer Sun. *Adv. Sci.* **2**, 1500119 (2015).

20. Grenier, Ph. Réfrigération radiative. Effet de serre inverse. *Rev. Phys. Appl.* **14**, 87–90 (1979).

21. TROMBE, F. PERSPECTIVES SUR L'UTILISATION DES RAYONNEMENTS SOLAIRES ET TERRESTRES DANS CERTAINES REGIONS DU MONDE. *Perspect. SUR Util. Rayonnem. Sol. Terr. DANS Certain. Reg. MONDE* (1975).

22. Mandal, J. *et al.* Hierarchically porous polymer coatings for highly efficient passive daytime radiative cooling. *Science* **362**, 315–319 (2018).

23. Mandal, J., Yang, Y., Yu, N. & Raman, A. P. Paints as a Scalable and Effective Radiative Cooling Technology for Buildings. *Joule* **4**, 1350–1356 (2020).

24. Gentle, A. R. & Smith, G. B. Radiative Heat Pumping from the Earth Using Surface Phonon Resonant Nanoparticles. *Nano Lett.* **10**, 373–379 (2010).

25. Zhou, L. *et al.* A polydimethylsiloxane-coated metal structure for all-day radiative cooling. *Nat. Sustain.* **2**, 718–724 (2019).

26. Mandal, J. Survey of Radiative Coolers. *Tableau Public* https://public.tableau.com/app/profile/jyoti.mandal/viz/SurveyofRadiativeCoolers-TestVersion/Homepage (2021).

27. Chen, Z., Zhu, L., Raman, A. & Fan, S. Radiative cooling to deep sub-freezing temperatures through a 24-h day–night cycle. *Nat. Commun.* **7**, 13729 (2016).

28. Berdahl, P. Radiative cooling with MgO and/or LiF layers. *Appl. Opt.* **23**, 370–372 (1984).

29. Czapla, B., Srinivasan, A., Yin, Q. & Narayanaswamy, A. Potential for Passive Radiative Cooling by PDMS Selective Emitters. in (American Society of Mechanical Engineers Digital Collection, 2017). doi:10.1115/HT2017-4853.

30. Mandal, J. Resources for Radiative Cooling Research. *Jyotirmoy Mandal* https://jyotirmoymandal.com/radiative-cooling-resources/ (2021).

31. Raman, A. P. Raman Lab @ UCLA. *GitHub* https://github.com/Raman-Lab-UCLA.

Chapter 4: Atmosphere modelling for radiative cooling potential

4.1 Introduction

In recent years, radiative cooling has seen growing scientific and commercial interest for applications ranging from the passive cooling of buildings to geoengineering. The process, which involves a spontaneous heat loss from terrestrial objects to the atmosphere and outer space by radiation of heat (and reflection of incident sunlight) through the atmospheric transmission windows, has a zero-energy, zero-carbon functionality and a net cooling effect on the environment [1]. Precisely how much cooling occurs for a given surface depends strongly on meteorological conditions. For instance, the cooling potential, which is defined as the difference between the radiance from a sky-facing radiative cooler and the downwelling atmospheric irradiance under clear skies, can vary between ~0-150 Wm^{-2} depending on the ambient temperature and total precipitable water (TPW) content[2].

Given this large variability, accurate determination of radiative cooling potentials is crucial for validating the performance of radiative coolers, informing industry on the geographical scope of designs like cool-roof paints[3], and potentially the best geographic regions for radiative cooling approaches for geoengineering[2,4]. Research over the years has yielded a range of atmospheric models that can be used to calculate radiative cooling potentials accounting for various factors such as humidity, topography, cloud cover and altitude[1,5–12]. However, standard models used today to calculate radiative cooling potentials or cooling power are often used beyond their scope, leading to systematic errors. The most prevalent example of this is the transmittance-based cosine approximation, widely used to model radiative cooling potentials under clear skies, particularly of materials with strong spectral and angular selectivity in their emissivity.

In this chapter, we elucidate the source of the errors in atmospheric radiance calculations that use the transmittance-based cosine approximation, and demonstrate its underestimation of radiative cooling potential due to its simplified accounting of the irradiance from greenhouse gases where the atmosphere is transparent. Comparative analysis against the MODTRAN atmospheric hemispherical irradiance model shows that the transmittance-based cosine approximation yields a significantly higher downwelling atmospheric irradiance and thus cooling potentials that are lower by 6-24 Wm^{-2} under typical operating conditions, which is 10-23% more than the approximation itself. To address this, we apply a temperature correction that accounts for the high elevations and thus low temperatures of greenhouse gases, namely water vapor, carbon dioxide and ozone, which allows a net heat transfer to them from the earth's surface. This reduces the underestimation of the cooling potential to 0.1-6%, while retaining the useful angular resolution of the transmittance-based cosine approximation, which the MODTRAN hemispherical irradiance model does not provide. Our results suggest that recently constructed maps of radiative cooling potentials may require corrections. Moreover, they indicate that the common use of the uncorrected transmittance-based cosine approximation to verify experimental demonstrations of radiative cooling could be leading to an overestimation of performance of radiative cooling designs across the literature.

4.2 Results and Discussion

Atmospheric Irradiance and the Transmittance-based Cosine Approximation

Due to its constituent greenhouse gases that are intrinsically absorptive or emissive in the thermal wavelengths, the atmosphere radiates heat towards the earth's surface. The difference between this irradiance I_{atm} and the blackbody radiance I_{BB} (T_{amb}) at the ambient air temperature (T_{amb}) close to the ground is what is typically defined as the cooling potential or cooling power

$P_{cooling}$ The cooling potential arises primarily within the long-wavelength infrared (LWIR, 8-13 μm) atmospheric transmission window, where the low intrinsic absorption of water vapor lowers I_{atm}, and reveals the cold upper reaches of the atmosphere and the cold space beyond, allowing for heat radiated upwards from the ground to be lost.

While the calculation of the blackbody irradiance is straightforward, it is more challenging to calculate I_{atm}, which needs to account for, at the very least, the spectral properties of greenhouse gases, their distributions along the height of the atmosphere, and variations in temperature across heights. A long history of work on this topic has yielded a number of useful theoretical models for calculating I_{atm}, each of which is reasonably accurate within its scope of use[1,5,7,6,9,8]. For instance, when using a spectrally flat emitter (gray- or black-body), simple correlations have been shown to be very accurate in predicting downwelling atmospheric irradiance[6]. However, for many radiative cooling calculations, spectrally and angularly resolved sky irradiance is often required since radiative cooling surfaces can present highly spectrally and angularly selective emissivity. Models which yield the level of detail needed for such calculations are comparatively rare[1,5,13]. One model, which has achieved almost universal use in recent radiative cooling literature is the transmittance-based cosine approximation[1,14–29], which was first used as part of a more comprehensive model by Granqvist in 1981[1]. This model assumes that the irradiance of the atmosphere originates from the greenhouse gases water vapor, carbon dioxide and ozone, and calculates the spectral, angular sky irradiance based on an effective spectral angular emittance as follows:

$$I_{atm}(\theta, \lambda, \mathrm{T_{amb}}) = \varepsilon_{atm}(\theta, \lambda, T_{amb}) \cdot I_{BB}(\theta, \lambda, \mathrm{T_{amb}}) \quad (1)$$

where

$$\varepsilon_{atm}(\theta, \lambda, T_{amb}) = 1 - [1 - \varepsilon_{atm}(0, \lambda, T_{amb})]^{1/cos\theta} \quad (2)$$

Here, ε_{atm} is the effective emittance of the atmosphere, θ is the angle measured from the zenith and λ is the wavelength. As stated by Granqvist, implicit in this model is Kirchhoff's Law, which states that at thermal equilibrium:

$$\varepsilon_{atm}(\theta,\lambda) = \alpha_{atm}(\theta,\lambda) = 1 - \tau_{atm}(\theta,\lambda) \quad (3)$$

Where $\alpha_{atm}(\theta,\lambda)$ is the spectral, directional absorptance of the atmosphere. $\tau_{atm}(\theta,\lambda)$ is the spectral, directional transmittance, and is calculated based on the zenith-ward value $\tau_{atm}(0,\lambda)$ using the cosine approximation:

$$\tau_{atm}(\theta,\lambda) = \tau_{atm}(0,\lambda)^{\frac{1}{cos\theta}} \quad (4)$$

The hemispherical irradiance I_{atm} can be calculated by hemispherical integration of the angular values from (1), and in turn yields $P_{cooling}$=$I_{BB} - I_{atm}$.

Issues with the Transmittance-based Cosine Approximation

While the model provides a reasonable estimate of I_{atm} (θ, λ), a crucial point to note is that in using Kirchhoff's law and equation (3), it implicitly assumes that the atmosphere is a homogenous entity at thermal equilibrium[1]. In reality, it is a complex, semi-transparent structure whose temperature decreases with height. Where the atmosphere is particularly transparent, the colder upper reaches of the atmosphere are apparent from the ground, which enables heat loss not only through the atmosphere, but also to it (Fig. 1A), a fact that is not accounted for by the transmittance-based approximation.

The case for ozone, illustrates this well. It is first important to note that the overwhelming majority of ozone occurs in frigid 10-40 km heights of the stratosphere, in what is known as the

ozone layer. Consequently, any downwelling irradiance outside the LWIR window from ozone is masked by the highly absorptive water vapor and CO_2 in the troposphere. In the LWIR window, however, the transparency of the atmosphere reveals the ozone layer and outer space beyond. This means that some of the radiance from the earth's surface is absorbed by the ozone, and much of its intrinsic radiance at ~ 9.5 μm reaches the earth. However, because of the low temperature of the ozone layer, which can be ~70°C lower than T_{amb} at altitudes where ozone concentration peaks in the summer, and ~40°C lower in the winter[30], it radiates far less towards the ground than it absorbs from the latter. In other words, a net heat loss occurs from the surface to the ozone layer, and the assumption of a thermally homogeneous atmosphere no longer holds (Fig. 1A). This is not captured by Equation (3), which implicitly assumes the ozone layer to be at T_{amb}, leading the downwelling irradiance from ozone to be incorrectly equal to the fraction of I_{BB} (T_{amb}) absorbed by it. Consequently, heat loss to the ozone layer is not registered, I_{atm} is overestimated, and $P_{cooling}$ is underestimated, as is shown in Fig. 1B. This is also evident when one compares the hemispherical emittance calculated by MODTRAN with I_{atm} calculated using the transmittance-based cosine approximation. The difference due to the ozone effect alone is about 5-18.5 Wm^{-2} depending on the atmosphere type and temperature, which is a significant 6-21% of the net cooling potential predicted by the transmittance-based cosine approximation.

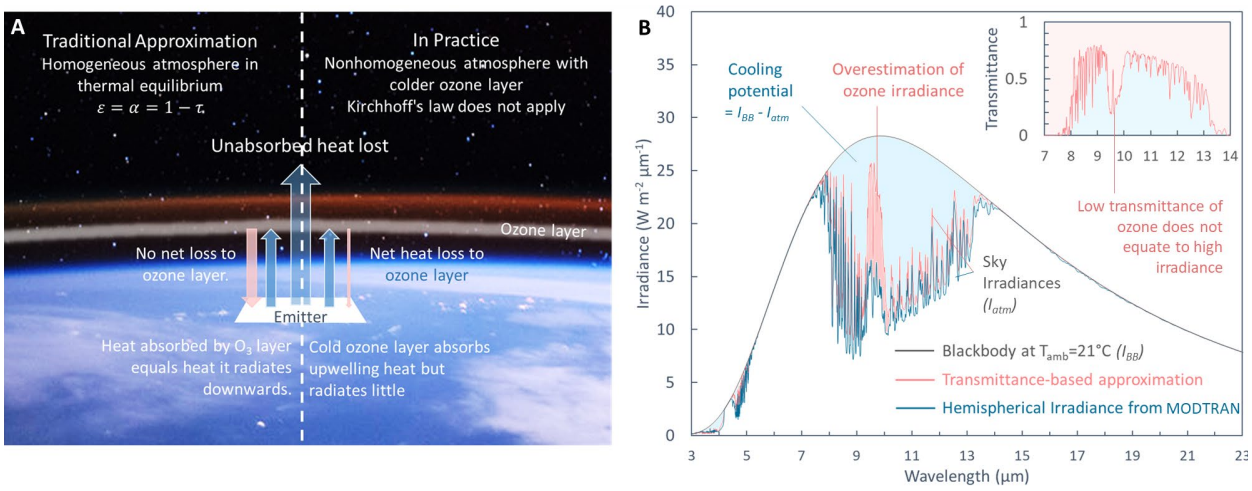

Figure 1. A) Conceptual framework for traditional atmospheric thermal radiation against real case atmospheric thermal radiation. The photograph[31] was used under the Creative Commons-CC-BY-NC-ND 2.0 License. B) The spectral hemispherical atmospheric irradiance of the transmittance-based approximation and that from MODTRAN,

A similar effect occurs for water vapor and carbon dioxide, which we consider collectively in this analysis. The two gases are well mixed throughout the atmosphere, and a majority of their downwelling irradiance arises from within ~10^2 m depths of the atmosphere near the earth's surface outside the LWIR window (which is at ~T_{amb}), and within 2 km of the earth's surface (or within ~ 12 °C of T_{amb}) in the LWIR. The resulting temperature differences are far less than that for ozone. Consequently, the transmittance-based approximation is largely correct outside the LWIR window where the atmosphere is opaque, and shows a lower underestimation of $P_{cooling}$ than seen for ozone at individual LWIR wavelengths (Fig. 1B). However, unlike for ozone, the underestimation occurs over a much broader bandwidth – across the LWIR and for dry atmospheres, across the 16-20 μm wavelengths, which adds to a significant total when integrated.

It should be noted that Granqvist explicitly proposed the transmittance-based cosine approximation for use with a box model for calculating the radiative cooling powers of SiO films on metal. Since the irradiance from ozone and absorptance/emittance of SiO films have little overlap, and the SiO film has a narrowband emittance, such a choice is justifiable in that context. However, the approximation has since been used to calculate radiative cooling potentials of ideal emitters and cooling powers of radiative coolers with different spectral emittances, leading both to a systematic underestimation of the cooling potential, and relative to it, an overestimation of the performance[14–29]. The MODTRAN hemispherical emittance, which is more accurate, should ideally be used instead. Indeed, Granqvist used a similar model in a later work[5]. However, because publicly available versions of MODTRAN contain no angle resolved information[30,32], to date, it has mostly been used for ideal emitters or real ones with ultra-wide angle emittances[33]. Furthermore, given the widespread use of the transmittance-based model in the radiative cooling community, it may be expedient for researchers to use a modified version of the model that provides the flexibility needed to accurately model spectrally and angularly-selective radiative coolers. Towards that end, in the subsequent section, we propose a correction to the transmittance-based cosine approximation that reduces the systematic overestimation of the ozone's irradiance, while retaining the necessarily angular resolution of the model.

Temperature-Corrections of the Transmittance-based Model

Although the publicly-accessible MODTRAN hemispherical irradiance model provides a highly accurate estimate of the cooling potential, it does not contain angle-resolved information, which is crucial for calculating the performance of typical radiative coolers whose emittances can vary considerably with angle[1,15,34,35], and which the transmittance-based cosine approximation provides. Therefore, here we propose a correction that retains the mathematical fundamentals of

the original model, but corrects for the overestimation of the irradiance from greenhouse gases. To do so, the lower effective temperatures of the ozone layer, and water vapor+CO_2 in the LWIR, which allow for heat loss from the terrestrial environment, must be taken into account. The ozone layer is kilometers thick, and CO_2 and water vapor are distributed throughout the atmosphere, which means that their radiative contributions are determined by a temperature distribution along their height. However, we can simplify calculations assuming that the irradiance of the i^{th} gaseous component arises from a specific combination of its emittance ε_i and effective temperature T_i. The irradiance I_{atm} can then be separated into two contributions, one for ozone, which is distributed high in the atmosphere, and one for CO_2 +water vapor, which is distributed throughout, as follows:

$$I_{atm}(\theta,\lambda) = \varepsilon_{ozone}(\theta,\lambda) \times I_{BB}(T_{ozone},\lambda) + \varepsilon_{rest}(\theta,\lambda) \times I_{BB}(T_{rest},\lambda) \quad (5)$$

The directional emittances $\varepsilon_i(\theta,\lambda)$of each component is calculated using Equations 2-4, using their transmittance instead of τ_{atm}. The transmittance $\tau_{rest}$of water vapor+CO_2, which effectively occur below the ozone layer, is calculated using MODTRAN by setting the atmospheric ozone concentration to zero. The transmittance of ozone is calculated as follows:

$$\tau_{Ozone}(\theta,\lambda) = \tau_{atm}(\theta,\lambda)/\ \tau_{rest}(\theta,\lambda) \quad (6)$$

As mentioned earlier, for the transmittance-based cosine model, it is reasonable to assume that the effective temperature of water vapor+CO_2 where it is highly absorptive is the ambient temperature T_{amb}, and the effective temperature of the completely masked ozone layer beyond is 0 K. It thus remains to calculate the effective temperature T_{Ozone} of the ozone layer in the LWIR, and T_{rest} of water vapor and CO_2 in the LWIR and in the 16-20 μm range. To do so, we first obtain from MODTRAN the effective hemispherical irradiance of CO_2 and water vapor I_{rest} (i.e. without ozone), and that of the ozone layer, I_{Ozone} by subtracting I_{rest} from the hemispherical irradiance

of the whole atmosphere (I_{atm}). In parallel, we also calculate the hemispherical emittance of water vapor+CO_2, and the ozone layer from the directional values $\varepsilon_{rest}(\lambda,\theta)$ and $\varepsilon_{Ozone}(\lambda,\theta)$ calculated earlier. We then solve for $T_i(\lambda)$ using the equation:

$$I_i(\lambda) = \varepsilon_i(\lambda)\int_0^{2\pi}\int_0^{\frac{\pi}{2}} 2hc^2\lambda^{-5}\left(e^{\frac{hc}{\lambda k_B T_i(\lambda)}}-1\right)^{-1}\cos\theta\sin\theta\ d\theta d\varphi \qquad (7)$$

Plots of T_{rest} and T_{Ozone} are presented in Fig. 2 for the six MODTRAN standard atmospheres, US standard, Tropical, Midlatitude summer, Midlatitude winter, Subarctic summer and Subarctic winter in Fig. 2. As shown, the effective temperatures of the gaseous components are drastically lower than T_{amb}, with ΔT(lambda) being 50-100°C for ozone and 5-20°C for water vapor+CO_2, which the traditional transmittance-based model does not capture.

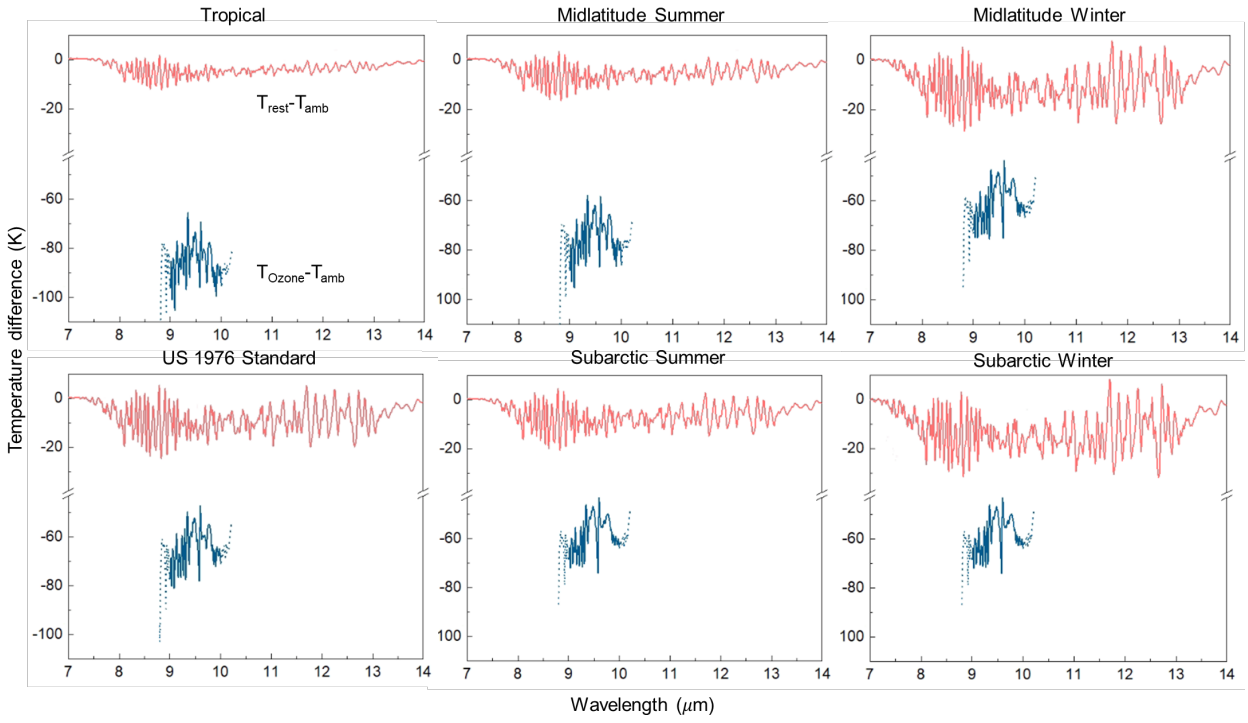

Figure 2. ΔT_{ozone} and ΔT_{rest} for the six MODTRAN standard atmospheres: Tropical, Midlatitude summer, Midlatitude winter, US 1976 Standard Atmosphere, Subarctic summer, Subarctic winter.

Equation 5, along with Equations 2-4, yields the directional irradiance, which in turn can be used to calculate the hemispherical irradiance (I_{atm}) that corrects the overestimation of the transmittance-based model. As an illustration, we present the resulting hemispherical sky irradiances I_{atm} for the six MODTRAN standard atmospheres against the respective MODTRAN and transmission-model outputs (Fig. 3). As expected, the corrected transmission-based I_{atm} is far closer to the MODTRAN irradiance than the original transmission-based approximation. More importantly, our method maintains its closeness to the MODTRAN model when the temperature T_{amb} is changed. Fig. 4 shows the cooling potential $P_{cooling} = I_{BB}(T_{amb}) - I_{atm}$ of the traditional transmission-based model, the corrected model we propose, and the MODTRAN irradiances of versions of the standard atmospheres at different temperatures. The values of I_{atm} are calculated using T_{amb} for the traditional transmission-based model, using T_{amb} and ΔT in Fig. 2 (assuming that ΔT is unaffected by T_{amb}) for the corrected model, and by scaling the irradiances of the standard atmosphere by the blackbody spectra corresponding to T_{amb} for the MODTRAN model. As shown in Fig. 4, the relative to the MODTRAN model, the traditional approximation underestimates the cooling potential of radiative coolers by 6 to 24 Wm^{-2} or 12 to 29 % depending on the temperature and atmosphere type. The underestimations are large, particularly for high values of I_{atm}. Our corrected model, by comparison, is within 1-8 Wm^{-2} or 0.1-7 % of the MODTRAN model, irrespective of the temperature, and the different total precipitable water and other greenhouse gas levels represented by the different atmospheres. The corrected transmission-based model thus provides an accurate irradiance relative to MODTRAN, while also providing angle-resolved irradiance values that the traditional transmission-based model provides.

It should be noted that the transmittance-based model, and the correction we propose, are intended for clear, cloudless skies. This is sufficient for validating experimental performances of

radiative coolers, as such experiments are usually performed under clear skies. However, the effects of clouds are important as well, particularly for mapping global average radiative cooling potentials. We note here our model can in principle be modified to account for clouds – which are essentially finite layers of condensed water vapor with high absorption across the thermal and LWIR wavelengths – similarly to how it accounted for the ozone layer in Equation 5. Doing so requires information about the thickness and type of clouds (e.g., thin cirrus vs thick cumulus), their heights (which could be estimated from the dew point temperatures and atmospheric lapse rates), their coverage and view angle from the perspective of the radiative cooler. However, that is beyond the scope of the present study, since the angle-resolved and spectrally resolved irradiances, which are the unique yields of the transmittance-based model, varies continuously as clouds move. In that case, the hemispherical irradiance becomes more important, and models which output it may be better suited. A number of such models, which take into account factors like cloud cover, topography and altitude exist in the literature[6,8,10–12,36,37], and could be used in conjunction with satellite imagery of cloud covers and their calculated transmittances[38], as well as radiometric characterization of clouds[39,40] to calculate downwelling atmospheric irradiances. It should be noted that if the cloud cover is uniform and near-full, the motion of individual clouds has little impact

and they behave as a layer, in which case our model can be conveniently used.

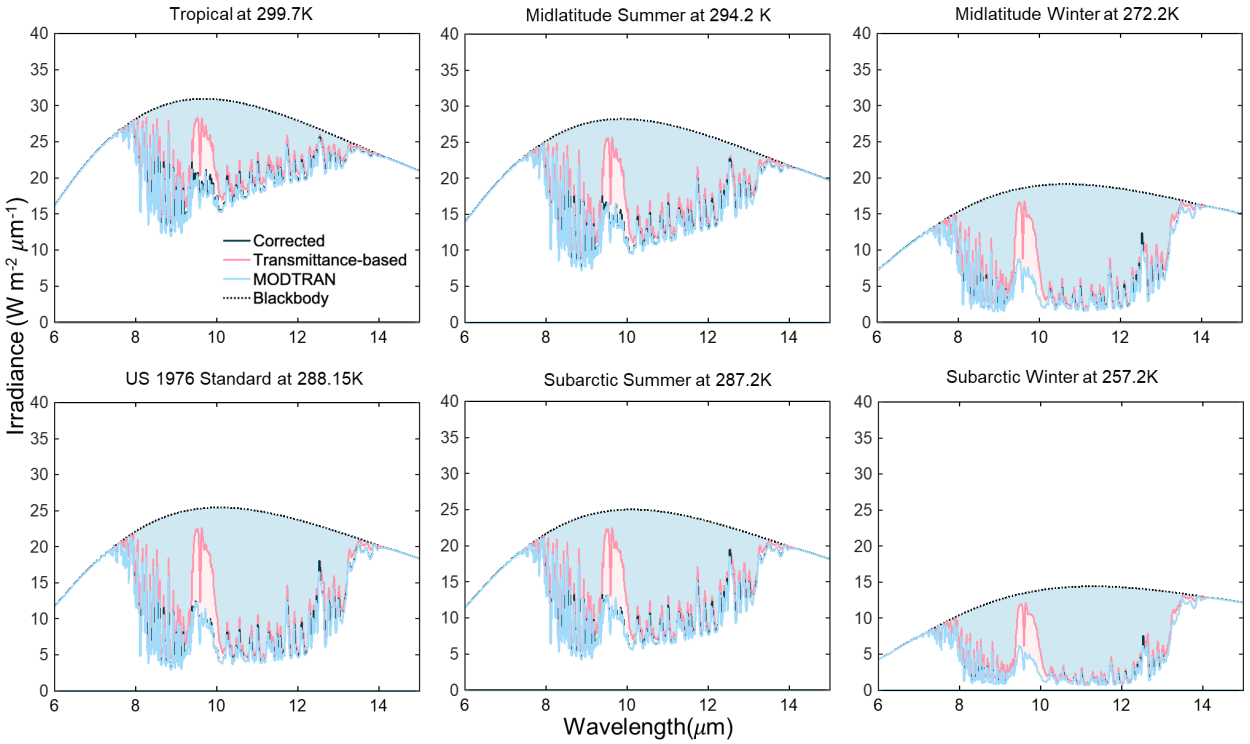

Figure 3. Spectral hemispherical atmospheric irradiance I_{atm} for the transmittance-based model and our corrected model for the standard MODTRAN atmospheres.

4.3 Conclusions

Two results stand out from our analysis. From a computational standpoint, our results indicate that a higher cooling power can be achieved by radiative coolers than is calculated using the traditional transmittance-based model under clear skies. This adds to their promise for cooling at local and global scales, with ~20% greater cooling potentials possible for some atmospheres. However, our results also suggest that except in rare cases, experimentally demonstrated radiative coolers perform less well relative to what is theoretically possible than usually thought. One reason for this could be that such radiative coolers often have their near-normal emittances reported and used in radiative cooling calculations, rather than their true hemispherical emittance, which may

require full angularly-resolved measurements. Since hemispherical emittances are usually considerably lower than the near-normal emittances typically reported [41], this could explain why this mismatch has not been previously noted.

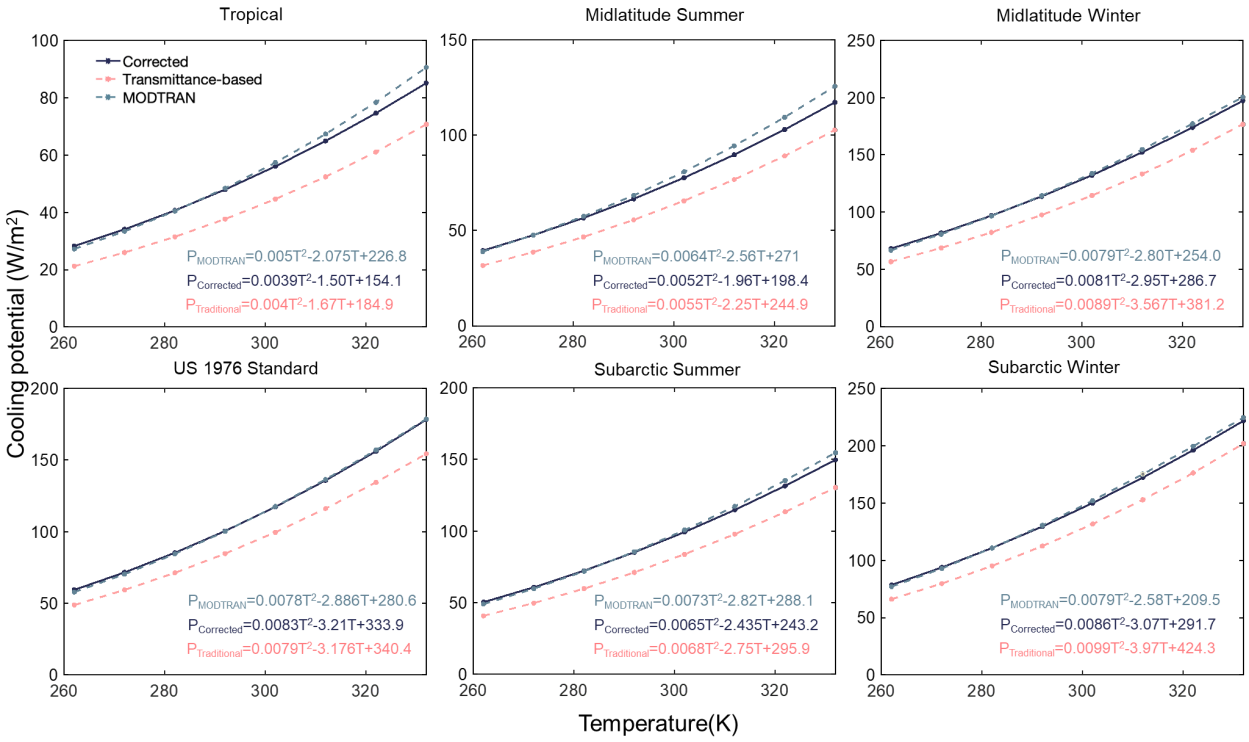

Figure 4. Maximum cooling potential ($P_{cooling} = I_{BB}(T_{amb}) - I_{atm}$) calculated using the traditional transmittance-based model, the corrected model and MODTRAN for the six standard atmospheric profiles, but with T_{amb} varied from 262 to 332 K. Dots indicate the calculated data, and the lines indicate fits with R^2>0.99. Equations for the fits are provided. The data at low temperatures for the Tropical, Midlatitude Summer and Subarctic summer atmospheric profiles should be used with caution because at such temperatures, the atmosphere does not typically hold the high TPW levels that characterize the standard cases.

Table 1. Analytical expressions of the $P_{cooling}$ corrections between the MODTRAN, transmittance-based and corrected models.

$\Delta P_{cooling}$	**Tropical**	**Midlatitude Summer**	**Midlatitude Winter**	**US 1976 Standard**	**Sub-Arctic Summer**	**Sub-Arctic Winter**
$P_{MODTRAN}$ -$P_{Corrected}$	$0.0011T^2$-0.57T+72.7	$0.0012T^2$-0.6T+72.6	-$0.002T^2$+0.15T-32.7	-$0.0005T^2$+0.32T-53.32	$0.0008T^2$-0.385T+45	-$0.0007T^2$+0.49T-82.2
$P_{MODTRAN}$ -$P_{Traditional}$	$0.001T^2$-0.4T+41.9	$0.0009T^2$-0.31T+26.1	-$0.001T^2$+0.767T-127.2	-$0.0001T^2$+0.29T-59.8	$0.0005T^2$-0.071T-7.9	-$0.002T^2$+1.39T-214.8

Given the above implications of our work, we believe that it may be useful to contextualize prior works which used the transmittance-based model, and that future works should account for the underestimation of the theoretical radiative cooling potential by the traditional transmittance-based model. Towards that end, we have provided analytical expressions of the cooling potentials for the different MODTRAN atmospheres as a function of temperature, as well as analytical expressions of $\Delta P_{cooling}$ between the MODTRAN, transmittance-based and corrected models, in Table 1. Additionally, we have also made numerical data for the zenith-ward transmittances and ΔT_i for different model atmospheres, which can be used with our method to calculate angular and hemispherical emittances, publicly available[42,43]. We hope that these resources will be useful to researchers modelling atmospheric irradiances for radiative cooling applications.

4.4 References

1. Granqvist, C.G.; Hjortsberg, A. Radiative Cooling to Low Temperatures: General Considerations and Application to Selectively Emitting SiO Films. *J. Appl. Phys.* **1981**, *52*, 4205–4220, doi:10.1063/1.329270.

2. Mandal, J.; Yang, Y.; Yu, N.; Raman, A.P. Paints as a Scalable and Effective Radiative Cooling Technology for Buildings. *Joule* **2020**, *4*, doi:10.1016/j.joule.2020.04.010.

3. Levinson, R.; Akbari, H. Potential Benefits of Cool Roofs on Commercial Buildings: Conserving Energy, Saving Money, and Reducing Emission of Greenhouse Gases and Air Pollutants. *Energy Effic.* **2010**, *3*, 53–109, doi:10.1007/s12053-008-9038-2.

4. Munday, J.N. Tackling Climate Change through Radiative Cooling. *Joule* **2019**, *3*, 2057–2060, doi:10.1016/j.joule.2019.07.010.

5. Eriksson, T.S.; Granqvist, C.G. Radiative Cooling Computed for Model Atmospheres. *Appl. Opt.* **1982**, *21*, 4381–4388, doi:10.1364/AO.21.004381.

6. Martin, M.; Berdahl, P. Characteristics of Infrared Sky Radiation in the United States. *Sol. Energy* **1984**, *33*, 321–336, doi:10.1016/0038-092X(84)90162-2.

7. Berdahl, P.; Fromberg, R. The Thermal Radiance of Clear Skies. *Sol. Energy* **1982**, *29*, 299–314, doi:10.1016/0038-092X(82)90245-6.

8. Li, M.; Peterson, H.B.; Coimbra, C.F.M. Radiative Cooling Resource Maps for the Contiguous United States. *J. Renew. Sustain. Energy* **2019**, *11*, 036501, doi:10.1063/1.5094510.

9. Berger, X.; Buriot, D.; Garnier, F. About the Equivalent Radiative Temperature for Clear Skies. *Sol. Energy* **1984**, *32*, 725–733, doi:10.1016/0038-092X(84)90247-0.

10. Centeno, M. New Formulae for the Equivalent Night Sky Emissivity. *Sol. Energy* **1982**, *28*, 489–498, doi:10.1016/0038-092X(82)90320-6.

11. Crawford, T.M.; Duchon, C.E. An Improved Parameterization for Estimating Effective Atmospheric Emissivity for Use in Calculating Daytime Downwelling Longwave Radiation. *J. Appl. Meteorol. Climatol.* **1999**, *38*, 474–480, doi:10.1175/1520-0450(1999)038<0474:AIPFEE>2.0.CO;2.

12. Iziomon, M.G.; Mayer, H.; Matzarakis, A. Downward Atmospheric Longwave Irradiance under Clear and Cloudy Skies: Measurement and Parameterization. *J. Atmospheric Sol.-Terr. Phys.* **2003**, *65*, 1107–1116, doi:10.1016/j.jastp.2003.07.007.

13. Raman, A.P.; Anoma, M.A.; Zhu, L.; Rephaeli, E.; Fan, S. Passive Radiative Cooling below Ambient Air Temperature under Direct Sunlight. *Nature* **2014**, *515*, 540–544, doi:10.1038/nature13883.

14. Rephaeli, E.; Raman, A.; Fan, S. Ultrabroadband Photonic Structures To Achieve High-Performance Daytime Radiative Cooling. *Nano Lett.* **2013**, *13*, 1457–1461, doi:10.1021/nl4004283.

15. Gentle, A.R.; Smith, G.B. A Subambient Open Roof Surface under the Mid-Summer Sun. *Adv. Sci.* **2015**, *2*, 1500119, doi:10.1002/advs.201500119.

16. Hossain, M.M.; Jia, B.; Gu, M. A Metamaterial Emitter for Highly Efficient Radiative Cooling. *Adv. Opt. Mater.* **2015**, *3*, 1047–1051, doi:10.1002/adom.201500119.

17. Hossain, M.M.; Gu, M. Radiative Cooling: Principles, Progress, and Potentials. *Adv. Sci.* **2016**, *3*, 1500360, doi:10.1002/advs.201500360.

18. Zhao, D.; Aili, A.; Zhai, Y.; Xu, S.; Tan, G.; Yin, X.; Yang, R. Radiative Sky Cooling: Fundamental Principles, Materials, and Applications. *Appl. Phys. Rev.* **2019**, *6*, 021306, doi:10.1063/1.5087281.

19. Aili, A.; Zhao, D.; Lu, J.; Zhai, Y.; Yin, X.; Tan, G.; Yang, R. A KW-Scale, 24-Hour Continuously Operational, Radiative Sky Cooling System: Experimental Demonstration and Predictive Modeling. *Energy Convers. Manag.* **2019**, *186*, 586–596, doi:10.1016/j.enconman.2019.03.006.

20. Son, S.; Liu, Y.; Chae, D.; Lee, H. Cross-Linked Porous Polymeric Coating without a Metal-Reflective Layer for Sub-Ambient Radiative Cooling. *ACS Appl. Mater. Interfaces* **2020**, *12*, 57832–57839, doi:10.1021/acsami.0c14792.

21. Liu, C.; Wu, Y.; Wang, B.; Zhao, C.Y.; Bao, H. Effect of Atmospheric Water Vapor on Radiative Cooling Performance of Different Surfaces. *Sol. Energy* **2019**, *183*, 218–225, doi:10.1016/j.solener.2019.03.011.

22. Zhu, Y.; Qian, H.; Yang, R.; Zhao, D. Radiative Sky Cooling Potential Maps of China Based on Atmospheric Spectral Emissivity. *Sol. Energy* **2021**, *218*, 195–210, doi:10.1016/j.solener.2021.02.050.

23. Huang, W.; Chen, Y.; Luo, Y.; Mandal, J.; Li, W.; Chen, M.; Tsai, C.-C.; Shan, Z.; Yu, N.; Yang, Y. Scalable Aqueous Processing-Based Passive Daytime Radiative Cooling Coatings. *Adv. Funct. Mater. n/a*, 2010334, doi:https://doi.org/10.1002/adfm.202010334.

24. Chen, M.; Yi, Z.; Tao, S.; Wang, S.; Fang, Z.; Lu, C.; Xu, Z. A Pragmatic Device Based on a Double-Sided Functional Structure for Efficient Water Harvesting. *Glob. Chall.* **2020**, *4*, 1900094, doi:https://doi.org/10.1002/gch2.201900094.

25. Kim, M.; Lee, D.; Son, S.; Yang, Y.; Lee, H.; Rho, J. Visibly Transparent Radiative Cooler under Direct Sunlight. *Adv. Opt. Mater.* **2021**, *9*, 2002226, doi:10.1002/adom.202002226.

26. Zhang, Z.; Dai, Y.; Ma, C. Design of Selectively Multilayered Periodic Gratings by PSO Algorithm for Radiative Cooling. *Opt. Commun.* **2021**, *500*, 127323, doi:10.1016/j.optcom.2021.127323.

27. Xiang, B.; Zhang, R.; Luo, Y.; Zhang, S.; Xu, L.; Min, H.; Tang, S.; Meng, X. 3D Porous Polymer Film with Designed Pore Architecture and Auto-Deposited SiO2 for Highly Efficient Passive Radiative Cooling. *Nano Energy* **2021**, *81*, 105600, doi:10.1016/j.nanoen.2020.105600.

28. Zhou, K.; Li, W.; Patel, B.B.; Tao, R.; Chang, Y.; Fan, S.; Diao, Y.; Cai, L. Three-Dimensional Printable Nanoporous Polymer Matrix Composites for Daytime Radiative Cooling. *Nano Lett.* **2021**, *21*, 1493–1499, doi:10.1021/acs.nanolett.0c04810.

29. Zhu, R.; Hu, D.; Chen, Z.; Xu, X.; Zou, Y.; Wang, L.; Gu, Y. Plasmon-Enhanced Infrared Emission Approaching the Theoretical Limit of Radiative Cooling Ability. *Nano Lett.* **2020**, *20*, 6974–6980, doi:10.1021/acs.nanolett.0c01457.

30. Spectral Sciences Incorporated MODTRAN® Available online: http://modtran.spectral.com/modtran_home (accessed on 19 October 2019).

31. Johnson, N. *The Atmospheric Glow and the Milky Way's Stars*; 2020;

32. University of Chicago MODTRAN Infrared Light in the Atmosphere Available online: http://climatemodels.uchicago.edu/modtran/ (accessed on 5 May 2020).

33. Mandal, J.; Fu, Y.; Overvig, A.C.; Jia, M.; Sun, K.; Shi, N.N.; Zhou, H.; Xiao, X.; Yu, N.; Yang, Y. Hierarchically Porous Polymer Coatings for Highly Efficient Passive Daytime Radiative Cooling. *Science* **2018**, *362*, 315, doi:10.1126/science.aat9513.

34. Gentle, A.R.; Smith, G.B. Radiative Heat Pumping from the Earth Using Surface Phonon Resonant Nanoparticles. *Nano Lett.* **2010**, *10*, 373–379, doi:10.1021/nl903271d.

35. Chen, Z.; Zhu, L.; Raman, A.; Fan, S. Radiative Cooling to Deep Sub-Freezing Temperatures through a 24-h Day–Night Cycle. *Nat. Commun.* **2016**, *7*, 1–5, doi:10.1038/ncomms13729.

36. Malek, E. Evaluation of Effective Atmospheric Emissivity and Parameterization of Cloud at Local Scale. *Atmospheric Res.* **1997**, *45*, 41–54, doi:10.1016/S0169-8095(97)00020-3.

37. Aubinet, M. Longwave Sky Radiation Parametrizations. *Sol. Energy* **1994**, *53*, 147–154, doi:10.1016/0038-092X(94)90475-8.

38. Srivastava, A.; Rodriguez, J.F.; Saco, P.M.; Kumari, N.; Yetemen, O. Global Analysis of Atmospheric Transmissivity Using Cloud Cover, Aridity and Flux Network Datasets. *Remote Sens.* **2021**, *13*, 1716, doi:10.3390/rs13091716.

39. Hirsch, E.; Agassi, E.; Koren, I. A Novel Technique for Extracting Clouds Base Height Using Ground Based Imaging. *Atmospheric Meas. Tech.* **2011**, *4*, 117–130, doi:10.5194/amt-4-117-2011.

40. Shaw, J.A.; Nugent, P.W. Physics Principles in Radiometric Infrared Imaging of Clouds in the Atmosphere. *Eur. J. Phys.* **2013**, *34*, S111–S121, doi:10.1088/0143-0807/34/6/S111.

41. Mandal, J. A Survey of Radiative Coolers in the Literature 2021.

42. Mandal, J. Resources for Radiative Cooling Research. *Jyotirmoy Mandal* 2021.

43. Raman, A.P. Raman Lab @ UCLA Available online: https://github.com/Raman-Lab-UCLA (accessed on 31 July 2021).

Chapter 5: Passive freezing desalination driven by radiative cooling

5.1 Introduction

Freshwater scarcity is expected to grow with rising temperatures this century, a challenge that will be compounded by growth in demand for water worldwide[1]. Only 1.5% of water on Earth is fresh water, with 96.5% of total water on Earth instead in the ocean as salt water[2]. Desalination has thus become an important method for the production of fresh water with daily desalination capacity estimated as 95.37 million m^3/day at the end of 2018[3], twice the rate of global water production in 2008[4]. In addition to fresh water generation, remediating industrial saline waste streams from sources such as oil and gas facilities[5–7] as well as brine waste from seawater desalination plants[8] is essential to mitigate the threats they pose to human health[9] and the environment[10]. Conventional membrane-based desalination processes are widely deployed but require significant energy inputs[11–13]. Collectively, most desalination systems deployed today need a substantial amount of energy, and thus lie at the heart of the nexus between energy and water use.

Thermal desalination has been actively explored for decades as a mechanism to complement reverse osmosis-based systems and is today a commonly used method for desalinating high salinity waters and brines. Thermal desalination entails the evaporation of salt water and its condensation into pure water, with typical thermal desalination systems also demanding large energy inputs typically driven by non-renewable fuels[14–17]. One notable exception is solar desalination[18,19], which exploits a renewable source of energy, and in the past decade has seen substantial advancement in systems enabled by solar-driven interfacial evaporation[20,21]. Although

much work has gone into developing high-performance materials[22–28] and high-efficiency system designs[29–32], solar desalination's need for high solar insolation has placed limits on its applicability in many geographic regions. Furthermore, the use of evaporation, a high-temperature phase change, introduces additional operational costs due to scaling and corrosion.

Here, we focus on an alternate phase change that can also enable thermal desalination: freezing. Freezing desalination exploits the fact that when water is crystallized to ice, salt will separate from the ice crystals which will be pure water. Compared to evaporation, the energy needed for the phase change can be reduced by 75% to 90% as the latent heat of fusion of ice is 334 kJ/kg, while the heat of evaporation of water is 2256 kJ/kg at 100°C[33]. Experiments in the 17th and 18th centuries demonstrated fresh water generation through the freezing of sea ice[34,35]. In the modern era, freezing desalination has remained an active topic of research inquiry with considerable focus on improving its efficiency[36–42]. Despite substantial early work on freezing desalination in the 1960s, commercialization of the technology has been hampered due to the substantial energy input needed for the freezing process[43]. If freezing desalination were possible to enable passively, however, its viability as a technology might be dramatically enhanced. Moreover, it could complement existing thermal evaporative desalination methods, including solar desalination.

Given this context, we are motivated by recent breakthroughs in passive radiative cooling[44,45] wherein sky-facing surfaces radiate their heat as thermal radiation, some of which effectively escapes to the cold of space through an atmospheric window in the long-wave infrared part of the electromagnetic spectrum between 8–13 μm. To passively reach temperatures substantially below the ambient, as one would need for freezing, it is well understood that thermal emitters that selectively emit within the atmospheric window will outperform broadband

emitters[46–48]. Prior work has shown that with a selective emitter and a vacuum system to minimize non-radiative heat gain a maximal reduction of 42 °C relative to the ambient is achievable[45]. Because of its cooling performance below ambient temperature, radiative coolers have also been used to obtain dew from atmosphere[49]. In the context of desalination, a single observational study in 1974 claimed that a natural freezing process resulted in desalination in open pools of salt water in the Atacama desert in Chile, where both evaporative and radiative cooling nominally resulted in freezing desalination[50]. However, this work did not provide any quantitative data with respect to the salinity levels of the water generated, and the overall efficiency of the process. Since that early work, no further attempts have been made at enabling a passive thermal desalination process using freezing. Recent advances in optimizing radiative cooling materials and systems however raise the intriguing possibility that this passive cooling mechanism could enable a compelling technological capability for thermal desalination.

In this chapter, we conceptually develop, and experimentally demonstrate passive freezing desalination driven by radiative cooling. Furthermore, we develop and validate models against our experimental results and use them to predict expected performance in a range of climate zones. We also use these models to determine the thermodynamic limits of performance of this approach to desalination. Collectively, our work shows that passive freezing desalination can be both competitive and complementary to solar desalination, and other thermal desalination approaches.

5.2 Results and Discussion

Conceptual Overview

Figure 1A shows the overall concept of the radiative cooling-driven freezing desalination process we propose. A sky-facing radiative cooler passively freezes the saltwater and ice, which in turn separate, with remaining higher salinity brine sinking because of its higher density. The

generated ice can then be melted into pure water. Figure 1B shows the specific steps in the radiative cooling-driven freezing desalination process. After freezing the salt water by thermal contact with the radiative cooling surface, the ice and the brine are mechanically separated through a simple filter. In practice, the remaining ice will have saltwater pockets trapped within it. Thus, following standard processing techniques for freezing desalination, we wash the generated ice particles with a small volume of pure water. The remaining high-purity ice is then melted to obtain fresh water.

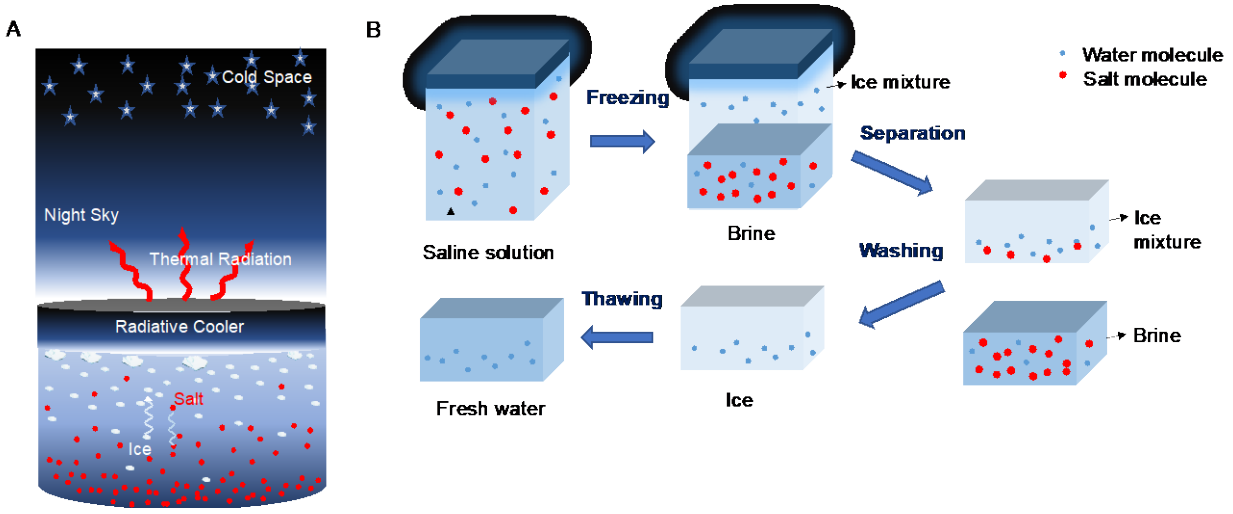

Figure 1: (A) Conceptual framework of the radiative cooling freezing desalination process. The ice forms inside the salt water because of the coldness of the radiative cooler and separates with the brine. **(B)** Detailed schematic of a single stage freezing desalination process, including freezing, separating, washing and melting.

We now examine the basic heat transfer mechanisms at play here to understand the potential of this passive approach to desalination. Consider a radiative cooler of area A at

temperature T. When the radiative cooler is exposed to the night sky, it is subject to downwelling atmospheric thermal irradiance (corresponding to ambient air temperature T_{amb}) as well as non-radiative heat exchange to its surroundings. The net cooling power P_{net} achievable by the radiative cooler is given by:

$$P_{net}(T) = P_{rad}(T) - P_{atm}(T_{amb}) - P_{cond+conv} \quad (1)$$

In Eq. (1) the power radiated out by the radiative cooling surface is

$$P_{rad}(T) = A\int d\Omega cos(\theta)\int_0^{\infty} d\lambda I_{BB}(T,\lambda)\,\varepsilon(\lambda,\theta) \quad (2)$$

Here $\int d\Omega = 2\pi\int_0^{\frac{\pi}{2}}$ is the angular integral over a hemisphere. $I_{BB}(T,\lambda) = \frac{2hc^2}{\lambda^5}\frac{1}{e^{hc/\left(\lambda k_B T\right)}-1}$ is the spectral radiance of a blackbody at temperature T, where h is Planck's constant, k_B is the Boltzmann constant, c is the speed of light and λ is the wavelength.

$$P_{atm}\left(T_{amb}\right) = A\int d\Omega cos(\theta)\int_0^{\infty} d\lambda I_{BB}\left(T_{amb},\lambda\right)\varepsilon(\lambda,\theta)\varepsilon_{atm}(\lambda,\theta) \quad (3)$$

is the absorbed downwelling atmospheric irradiance over long-wave infrared wavelengths. The atmospheric emittance $\varepsilon_{atm}(\lambda)$ is calculated from $I_{sky}(\lambda)$ using the MODTRAN Web Application for different weather conditions, as shown in the Supplementary section. Finally, heat gained due to conduction and convection $P_{cond+conv}$ can be expressed based on a combined effective heat transfer coefficient h_c as

$$P_{cond+conv}\left(T,T_{amb}\right) = Ah_c\left(T_{amb} - T\right) \quad (4)$$

A selective thermal emitter will have high emittance within the atmospheric window (8–13 μm) and low emittance elsewhere. For below-ambient cooling (i.e., $T < T_{amb}$), a broadband thermal emitter stands to gain more heat from thermal radiation outside the atmospheric window than it loses through thermal emission within the window, potentially resulting in negative cooling power and limiting the lowest temperature achievable. By contrast, a selective emitter allows us to maximize $P_{net}(T)$ at sub-ambient temperatures and thereby achieve a lower temperature, which is essential for freezing desalination.

At the onset of freezing, the maximum ice generation rate that can be formed from simple thermodynamic considerations alone can be understood by equating the net cooling power P_{net} at that temperature to v_f, the ice generation rate of salt water and H_f the enthalpy of fusion of water (334 kJ/kg):

$$P_{net}(T) = v_f H_f \quad (5)$$

To illustrate the potential of radiative cooling-driven desalination, we calculate and show in Figure S1 the maximum ice generation rate per second at a temperature of -2°C for a range of air temperatures and relative humidity conditions assuming an ideal selective emitter. While this is meant to be a first-order thermodynamic approximation, it does indicate the potential of radiative cooling to enable meaningful ice generation for a range of weather conditions. In a full implementation of such a system, to enable truly passive operation, the radiative cooling surface

will further be responsible for cooling the saline solution to the onset of freezing, and the kinetics of the freezing process will determine the nature of crystallization. We explore this in further detail as part of our experimental implementation and detailed modeling in this paper.

Experimental Implementation

We experimentally demonstrated passive freezing desalination driven by radiative cooling using a custom-built apparatus shown in Figure 2A. The radiative cooling surface is made of a low-cost acrylic polymer (3M Scotch tape[51]) coated with silver, which is then affixed to a polished aluminum cold plate which contains two tubes for water. The plate and radiative cooling surface are placed inside a polystyrene box which is covered with Aluminized mylar both inside and outside to minimize its own emittance. Two clear 12.5-μm polyethylene films are placed above the sample at a distance of 7 cm as an infrared-transparent windshield to enable effective, yet low-cost insulation. Hemispherical emissivity measurements of the radiative cooling surface show that it possesses a selective thermal emittance with high emittance in the atmospheric window (Figure 2B).

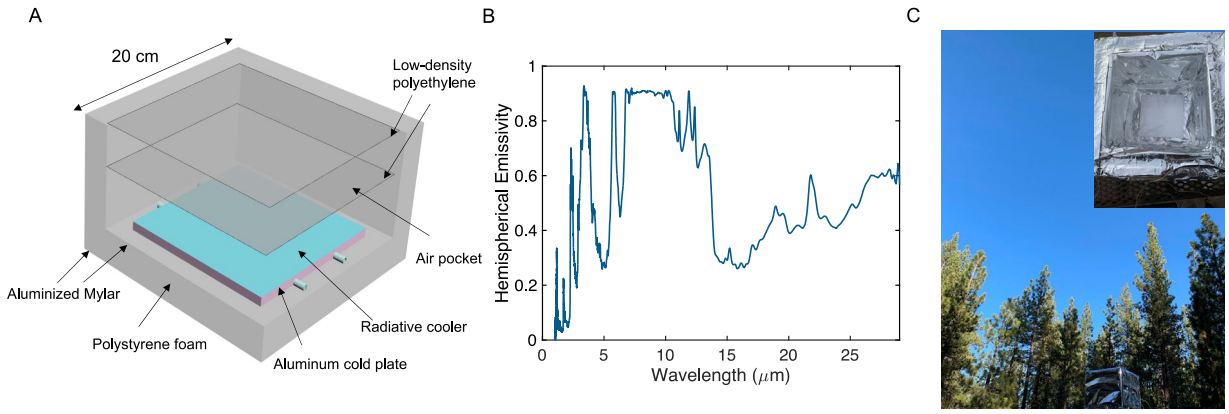

Figure 2: **Experimental apparatus and conditions:** (**A)** Three-dimensional schematic of the radiative cooling apparatus. A cold plate with two tubes is used to place the salt water in thermal contact with the radiative cooling surface, while the rest of the apparatus is designed to minimize conductive and convective heat exchange to the cooler. (**B)** Hemispherical emissivity measurement of the low-cost acrylic polymer used as the radiative cooling surface in the experiment. C Photo of the setup and its surroundings in Big Bear Lake, CA, USA. The apparatus can be seen at bottom during daylight hours. Experiments were conducted at night.

We demonstrated the performance of the radiative cooling desalination device in two overnight experiments at Big Bear Lake, California (photo of the environment is shown in Figure 2C), by exposing it to the sky during night-time hours and testing its performance. In the first experiment, the tubes in the cold plate were filled with 30 mL of salt water at 37.3 g/L, approximately the salinity of seawater. As shown in the temperature data of Figure 3A, immediately after the cooler is exposed to the environment (shortly before 22:30 local time in Figure 3A), its temperature drops to approximately 8°C below the measured ambient air temperature. The temperature of the saltwater reaches -6.2°C around 00:40 at which point it rises rapidly to -2.98°C, a signature of the onset of freezing. The temperature of the forming ice/water

slurry then slowly drops to -4.5℃ during the crystallization process. Through multiple lab experiments we determined that this temperature range resulted in approximately 75% crystallization in our setup, a crystallization level previously shown to be optimal for freezing desalination[36]. At this point, we removed the ice/water and brine mixture from the tube and mechanically separate the ice and brine using a simple paper filtration system and use 3.5 mL of fresh water to wash the formed ice crystals to remove the attached brine on the surface of the ice crystal. 19 mL of water with a salinity of 8.99 g/L is obtained after melting the ice crystals, as shown in Figure 3C.

We then re-inserted the partially desalinated water from the first stage back into the tube of the cold plate and repeated the previous steps for a second stage of freezing desalination. As shown in the temperature data of Figure 3B, after the cooler is exposed to the environment (at 03:07 local time in Figure 3B), its temperature drops to around -5℃ at 04:00 and immediately rises to -1.35℃ because of the lower salinity of the salt water. We repeated the separation process and used 2.5 mL of fresh water to wash the formed ice crystals. After the second stage's desalination process, we finally obtained 15 mL with a salinity of 1.88 g/L (Figure 3C) representing a 50% recovery rate from the 30 mL salt water initially introduced into the system. We note that the wash water used in both stages rapidly flows past the ice and in this implementation contributes negligibly to the finally measured output water from the system which is determined by melting the remaining ice.

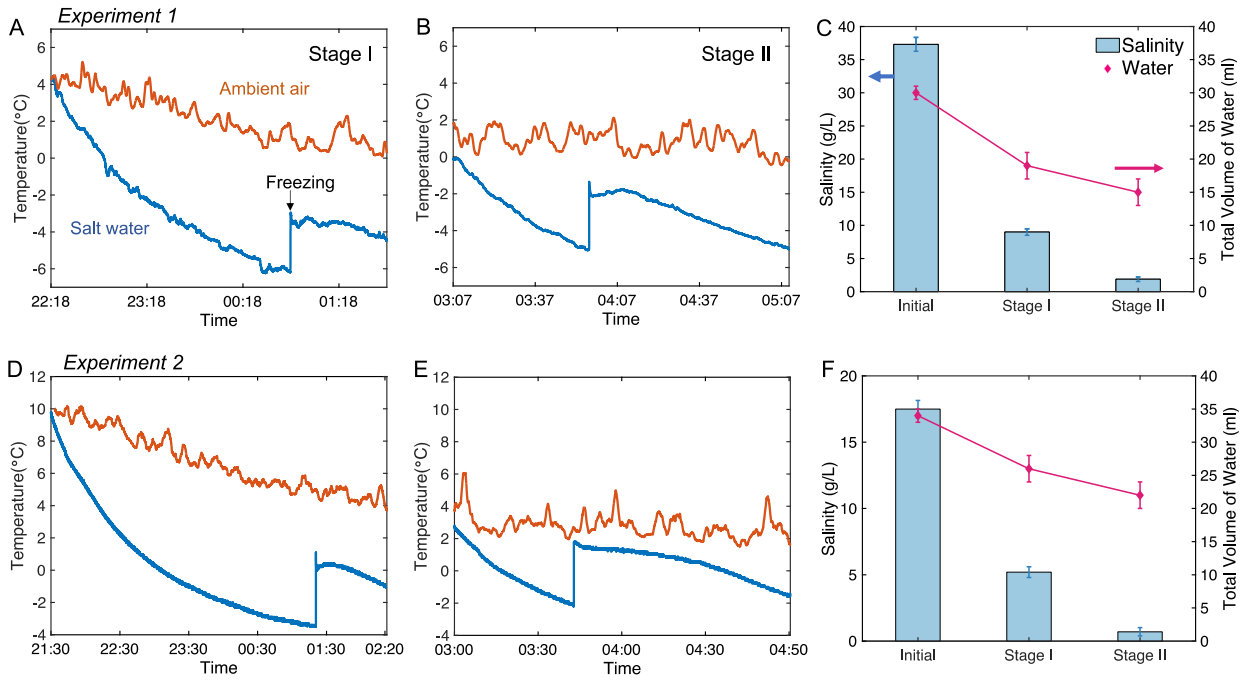

Figure 3: (**A)** First stage measurement of the salt water (37.3g/L) temperature (blue) against ambient air temperature (orange) on a clear night in Big Bear Lake, California, USA. The water temperature immediately drops below ambient once exposed to the sky and increases from -6.2℃ to -2.98 ℃ at the onset of freezing. **(B)** Second stage measure of the first stage's saltwater temperature (blue) vs. ambient air temperature (orange). The water temperature drops to -5.01 ℃ and then rises to -1.35 ℃ at freezing onset. (**C)** Salinity measurements of the two desalination stages. The salinity of water drops from 37.3 g/L to 8.99 g/L after the first stage with a 11 mL water loss and from 8.99 g/L to 1.88 g/L at the second stage with a 4 mL water loss. (**D)** First stage measurement of the lower salinity input saltwater (17.5 g/L) temperature (blue) vs. ambient air temperature (orange) on a clear night at the Big Bear Lake test site. The water temperature immediately drops below ambient once exposed to the sky and increases from -3.5℃ to 1.1 ℃ at the onset of freezing. (**E)** Second stage measurement of the saltwater temperature (blue) vs. ambient air temperature (orange). The water temperature drops to -2.2 ℃ and then rises to

1.65 ℃ at freezing onset. **(F)** Salinity measurements after each desalination stage. The salinity of water drops from 17.5 g/L to 5.2 g/L at the first stage with an 8 mL water loss and from 5.2 g/L to 0.7 g/L at the second stage with a 4 mL water loss.

To explore the effect of initial input salinity, in a second experiment we demonstrated the performance of the radiative cooling desalination device for lower salinity input water. In this experiment, the tubes in the cold plate were filled with 34 mL of salt water at 17.5 g/L input salinity. As shown in the temperature data of Figure 3D, immediately after the cooler is exposed to the environment (at 21:30 local time), its temperature drops to approximately 13℃ below the measured ambient air temperature, a deep sub-ambient cooling effect enabled by the selective thermal emitter. The temperature of the saltwater reaches -3.5℃ at around 01:10 at which point it rises rapidly to 1.1℃ at freezing onset. The temperature of the forming ice/water slurry then slowly drops to -1.2℃ during the crystallization process. As in the previous experiment, we mechanically separated the ice and brine and used 3.5 mL of fresh water to wash the formed ice crystals to remove the attached brine on the surface of the ice crystal. 26 mL of water with a salinity of 5.2 g/L is obtained after melting the ice crystals, as shown in Figure 3F. We next re-inserted the 26 ml of 5.2 g/L salinity saltwater back into the tube of the cold plate and repeated the previous steps for a second desalination stage. As shown in the temperature data of Figure 3E, after the cooler is exposed to the environment (at 03:00 local time in Figure 3E), its temperature drops to around -2℃ at 03:45 and immediately rises to 2℃ because of the lower salinity of the salt water. We then repeated the separation process and use 2.5 mL of fresh water to wash the ice crystals. After the second stage's desalination process, we finally obtained 22 mL of water at a salinity of 0.7 g/L

(Figure 3F) representing a 65% recovery rate from the 34 mL salt water initially introduced into the system.

After the first stage of the desalination process in these experiments the salinity of saltwater decreases 70-75% while there is also 8-11 mL water loss. Previous work has shown that in freezing desalination systems the removal efficiency decreases as the residual liquid volume reduces due to the difficulty of maintaining regular contact between the liquid and solid phases[52]. Freezing in general can further cause impurities to be trapped inside ice crystals relative to the fraction of the solution that remains unfrozen. This in turn can result in lower separation efficiency of the salt-water solution[53–55]. There is thus a compromise between water loss and the purity of water obtained that we believe can be further optimized in future work. Finally, we note that the pump for the mechanical separation process used here consumes about 30 J during the desalination process. This corresponds to less than 0.5% of the total energy that would otherwise be needed to freeze 19 ml of salt water. This energy consumption is thus negligible relative to the effective energy savings made possible by the passive radiative cooling process.

Modeling and validation

We next developed a theoretical model for the developed freezing desalination system, validated it against the experimental measurements and then used it to predict the net freshwater yield of both current and future improved radiative-cooling freezing desalination systems in a range of climate zones. Given input environmental conditions (air temperature and dew point), as well as the mass of water in the system, the model first predicts the cooling curve for water in the radiative cooling apparatus (see Supplementary Information for details). In Figure 4A, the model's

prediction for the temperature of the saltwater at an input salinity of 37.3 g/L for a range of non-radiative coefficients of heat exchange is compared against the first stage experimental data in Figure 4A and the second stage in Figure 4B, showing excellent agreement. The temperatures of saltwater for the lower input salinity experiment (17.5 g/L) for both stages are also simulated by the model, and shown in Figure 4Cand 4D, also showing excellent agreement. The model then uses this information, as well as phenomenologically derived assumptions about when freezing onset occurs, and the associated temperature rise of the saline solution, to predict a range of expected freshwater production rates for a particular set of operating conditions (see Supplementary Information). The model's predicted range of freshwater production is shown in Figure 4E and is validated against the values obtained experimentally showing excellent overall agreement.

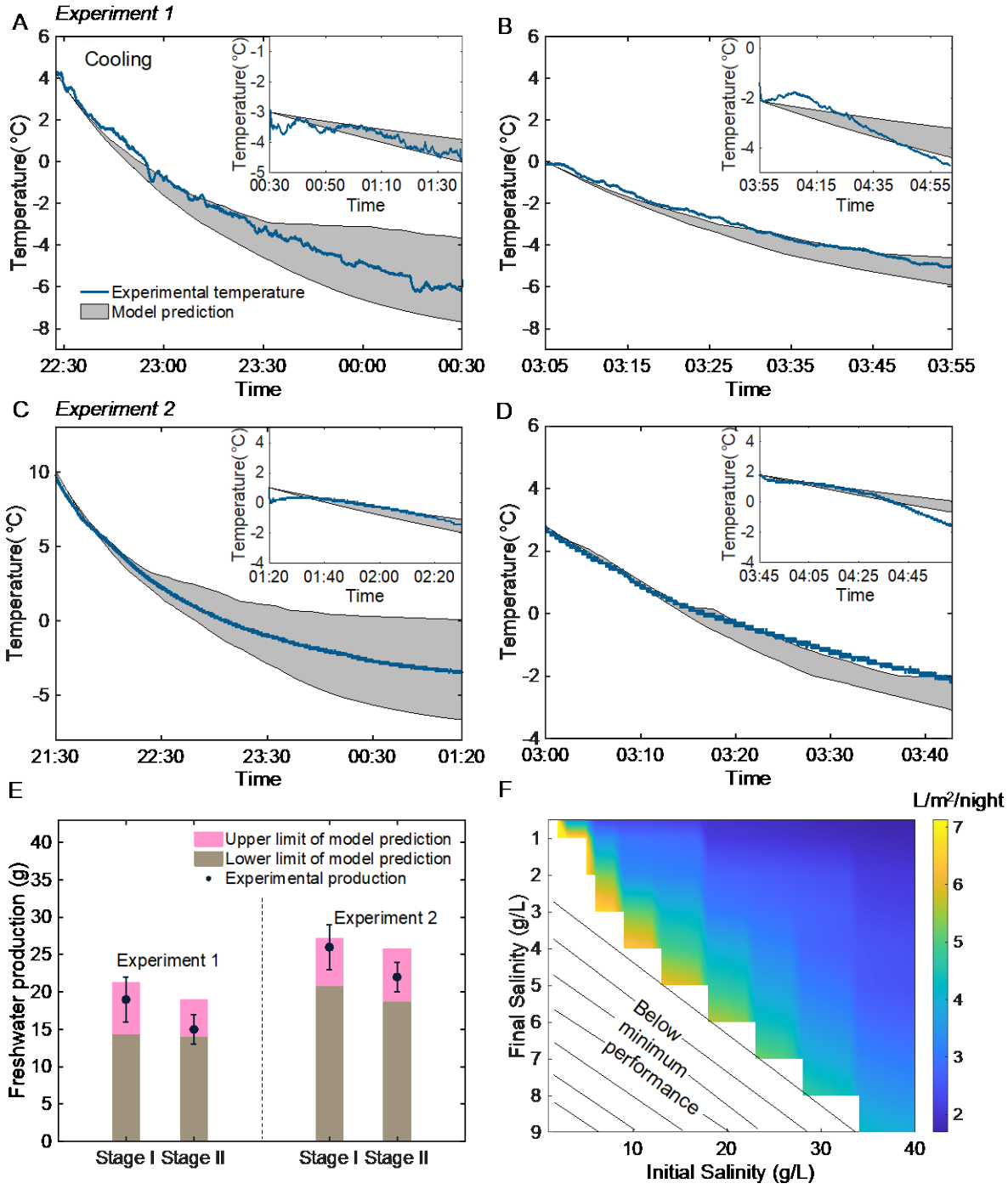

Figure 4: (A) Model predictions (gray) vs. experimentally measured (blue) saltwater (37.3 g/L concentration) during the first stage, showing excellent agreement. The gray regions denote model uncertainty associated with the coefficient of non-radiative heat

exchange which is modeled in a range of potential values. (**B)** Model predictions (gray) vs. experimentally measured (blue) saltwater (37.3 g/L concentration) during the second stage, also showing good agreement. (**C)** Model predictions (gray) vs. experimentally measured (blue) saltwater (17.5 g/L concentration) during the first stage, showing excellent agreement. (**D)** Model predictions (gray) vs. experimentally measured (blue) saltwater (17.5 g/L concentration) during the second stage, also showing good agreement. **(E)** Modeled total freshwater production from saltwater vs. experimentally yielded quantities. **(F)** Modeled total freshwater production using the experimental apparatus for different input salinities given weather conditions during experiments at the Big Bear Lake test site, and assuming the use of up to three consecutive stages.

We next used the validated model to predict the nightly freshwater output of our apparatus for different input and output salinities under the same set of environmental conditions as our experiments. First, we note that the higher the salinity of input saltwater, the harder it will be for it to freeze, as it will have to reach lower supercooling temperatures, as shown in Figure S3. Furthermore, higher salinities can necessitate multiple stages of freezing and washing, as demonstrated in our experiments. Using our experimental implementation as a phenomenological baseline for the values of the input and output salinities achievable for experimental stage (with a maximum of four stages total set as an upper limit), we show in Figure S5 the expected number of desalination stages needed as a function of input salinity. The model demonstrates that, given our apparatus and test environmental conditions, it takes at most three stages to desalinate freshwater from higher salinity water (37.3+ g/L), and takes fewer stages for lower input salinities. For seawater desalination (input salinity of 35 g/L), based on the current implementation (current cold

plate, radiative cooling material and apparatus insulation) the performance of this system at different ambient temperatures and relative humidities is shown in Figure 5A. In this model, we assume that there is no supercooling resulting in freezing onset as prior works has shown that supercooling can be avoided by adding a nucleation agent or increasing the roughness of the nucleation surface[53,56–60].

Finally, to explore the performance limits of radiative cooling-driven freezing desalination, we further apply our model on an idealized freezing desalination system. We assume in this model that the mass of the cold plate is negligible, that the radiative cooling surface is under vacuum, that the radiative cooler is an ideal selective thermal emitter (with unity emissivity between 8-13 um and 0 at other wavelengths), that the convective shield has perfect transmittance and that there is no supercooling resulting in freezing onset exactly at the freezing point of 35 g/L salt water (-2 °C). The performance predictions under these assumptions for different ambient temperatures and relative humidities is shown in Figure 5B. For the ideal case, as much as 0.9 $L/m^2/h$ freshwater can be generated using this method, which compares favorably with common solar desalination production values of 0.3-0.7 $L/m^2/h$ under the standard one Sun illumination condition (1 kW/m^2)[61–63], but is lower than the theoretical limit of hourly averaged production values for a multi-stage solar desalination system, 10 $L/m^2/h$[15,21].

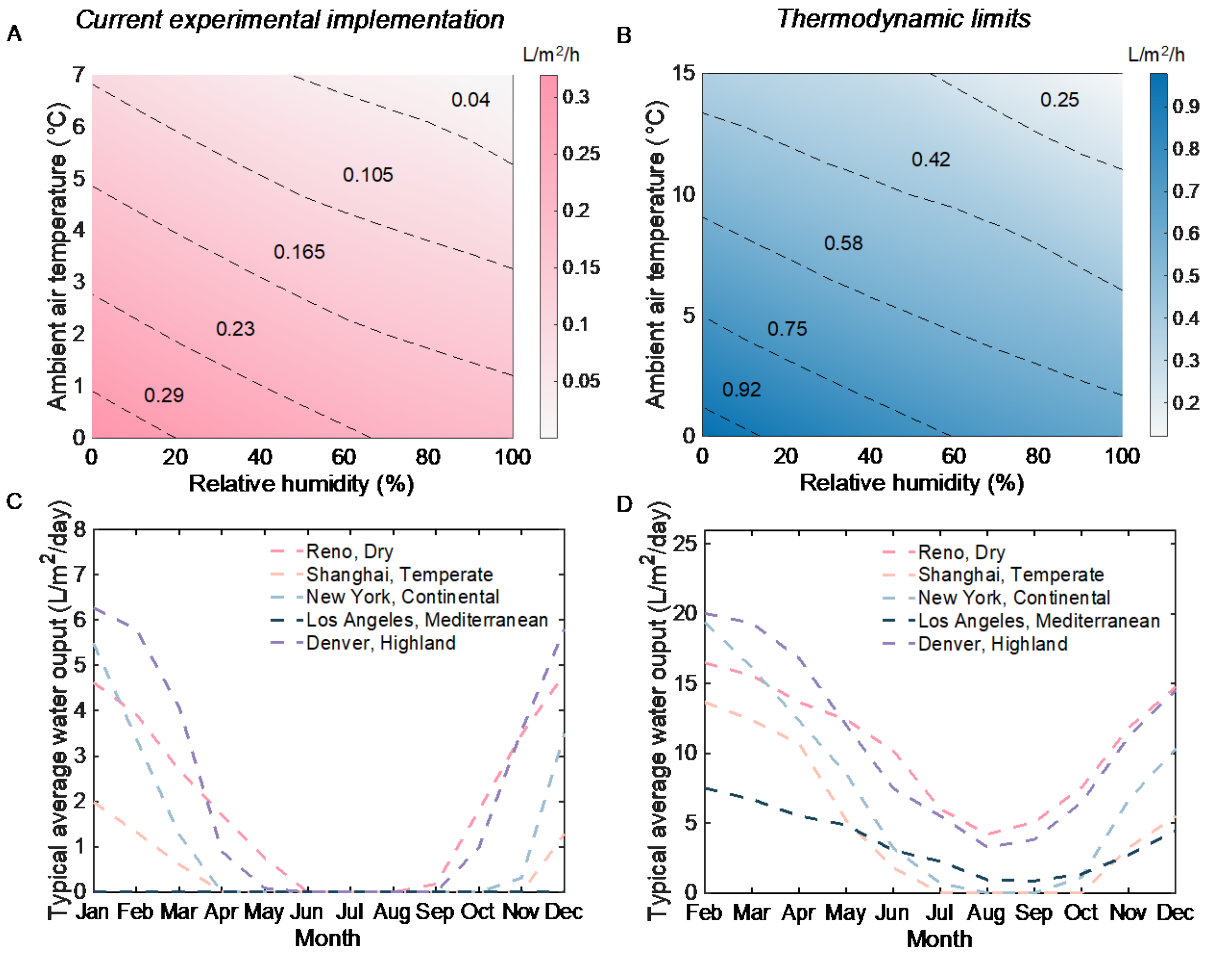

Figure 5: (**A)** Model prediction of the amount of water produced hourly by radiative cooling freezing desalination assuming the current experimental implementation for different relative humidity and ambient temperatures. (**B)** Single-state thermodynamic limit of hourly water production by radiative cooling freezing desalination for different relative humidity and ambient temperatures. (**C)** Prediction of average daily water production each month of the current experimental implementation using typical meteorological year (TMY3) weather data for cities located in five different climate zones. (**D)** Single-state thermodynamic limit of average daily water production each month for the same cities located in five different climate zones.

To further explore the viability of this approach to desalination, we apply our model using typical meteorological year (TMY3) data for cities in five different climate zones: dry, temperate, continental, Mediterranean, and highland climates. We then calculate the amount of water produced by radiative cooling freezing desalination daily based on both the current experimental implementation in Figure 5C, as well as the production from the ideal passive radiative cooling-driven freezing desalination system in Figure 5D. In all cases we consider solar energy absorption by the radiative cooler based on its current solar reflectivity. Overall, with this desalination approach we observe the highest production during non-summer months when solar irradiance and ambient temperatures are cooler in all climate zones. However, as shown in Figure 5D, with further improvements meaningful production can occur during low solar irradiance hours in the summer as well. As can be seen in Table S2 of the Supplementary Information, the dry and highland climate zones are optimal climate zones due to many hours of relatively cooler air temperatures and lower relative humidities. However, in winter months with relatively solar irradiance, this approach may outperform solar desalination-based approaches.

While Figure 5 examines the system's performance in terms of production capacity, the rates shown here must be compared against system costs. As a preliminary effort to that end, we developed a first order levelized cost of water (LCW) analysis for the passive freezing desalination system and benchmarked it against LCW ranges for other desalination methods. As shown in Figure S6, production rates of 2-5 $L/m^2/day$, achievable with the system as it would currently performs in range of climate zones (Figure 5C), could yield LCW in the range \$1.5 – \$0.75/m^3, competitive with solar desalination today[64]. We note that with the theoretical limits of performance shown in Figure 5D, Figure S6 indicates that LCW could be achieved that would be competitive with membrane desalination systems in a range of climate zones. The current implementation's

costs are driven by small-volume manufacturing of the cold plate used, as well as sub-optimal performance due to non-ideal infrared selectivity as well as supercooling. Improvements on both these fronts are possible with increased manufacturing scale, as well as through further advancements in selective radiative coolers. While this is a preliminary estimate, the results do highlight the potential of this approach to desalination, given the simplicity of the system's components and low-temperature operation relative to alternate thermal desalination approaches that rely on evaporation. For climate zones with relatively low solar irradiance during large fractions of the year, radiative cooling-driven desalination may represent a compelling renewable thermal desalination approach, including to remediate saline wastewater in industrial, and oil and gas facilities.

5.3 Conclusions

To summarize, we have highlighted the remarkable possibility and potential of desalinating salt water by radiative cooling-driven freezing desalination. Unlike membrane desalination, our approach is passive and can in principle work for water of any salinity level. Compared with solar desalination, our approach overcomes both challenges associated with evaporative desalination, including corrosion related to high temperature operation, and makes freezing desalination more attractive from an energy input perspective. While a potentially competitive technology in its own right, we emphasize that radiative cooling-driven freezing desalination could be combined with solar desalination to realize year-round, 24 hour a day passive thermal desalination for the first time. The low-salinity water generated by this method could also serve as a preliminary stage for conventional membrane-based desalination to overcome the high pressures that can be encountered when desalinating high-salinity input streams. While radiative cooling has emerged in recent years as an important frontier for research in energy challenges, this work highlights the important contributions that harnessing the thermodynamic resource of the cold of space could play for water challenges we face this century.

5.4 Supporting Information

1. Experimental Methods

Temperature measurements

Desalination experiments were performed on a flat surface in Big Bear Lake, California, in late June 2020 and 2021. The apparatus containing the radiative cooler consists of a 2-inch-thick polystyrene foam covered by a layer of aluminized Mylar. A polished, custom-fabricated aluminum cold plate is on the bottom of the box and the radiative cooler is placed on the top of it.

Two layers of 12.5 μm low-density polyethylene film is then used to seal the top of the box and serve as an infrared-transparent shield. This design, schematically represented in Figure 2A, creates a well-sealed air pocket around the sample, which provides the well insulation.

The tube was inserted by a thermocouple with ±0.25 ℃ accuracy sealed by wax, connected to a data logger (Omega-OM-USB-TC). Ambient air temperature is measured by another thermocouple with accuracy with free air flow near the sample, but outside the air pocket around the sample.

Salinity measurements

The ice and brine were poured into a vacuum filtration system, which includes 500 ml filter flask, 9 cm porcelain buchner funnel, 9 cm filter paper, pre-drilled rubber stopper and 3/8 in vacuum tubing with a 1/4 in adapter sleeve as well as a 1 W vacuum pump for 15 s. The solid ice particles cannot pass through the filter medium and are washed by 3.5 ml pure water. After washing, the ice crystals were transferred into a beaker. Once the ice melted completely, its salinity was measured using a LCD salinity meter (Grainger) with an accuracy of ±2%.

Spectral characterization of the radiative cooler

The hemispherical emissivity of the radiative cooler is measured by a Bruker Invenio-R FTIR spectrometer and is shown in Figure 2B. Emissivity is measured by angular reflectance measurements from 0° to 80 with integrating sphere and averaged using Eq. (6). We observe strong thermal emissivity in the atmospheric window between 8 μm and 13 μm.

$$\varepsilon_{\lambda} = \frac{\int_0^{2\pi}\int_0^{\frac{\pi}{2}} \varepsilon_{\lambda,\theta}(\lambda,\theta,\phi)\cos(\theta)\sin(\theta)\,d\theta\,d\phi}{\int_0^{2\pi}\int_0^{\frac{\pi}{2}} \cos(\theta)\sin(\theta)\,d\theta\,d\phi} \tag{6}$$

Typical water output in different cities

To access the temperature data for different cities, we use the TMY3 data from EnergyPlus, a widely used temperature resource. We use average hourly ambient temperature of different cities in a typical month provided by the TMY3 temperature file and assume the ambient temperature is constant during each hour segment. The amount of water produced by radiative cooling freezing desalination on a daily basis based on the current experiment implementation and the ideal conditions are shown in Figure 5(C,D).

2. First-Order Thermodynamic Model

Figure S1 shows the maximum ice generation rate per second at a temperature of -2°C (freezing point of 35 g/L salt water) from a first-order thermodynamic calculation. The calculations are performed for a range of air temperatures and relative humidities in clear sky conditions assuming an ideal selective emitter with unity emissivity between 8 and 13 microns, and zero elsewhere, and no non-radiative heat exchange (vacuum insulation). Expected freezing output limits range from 0.06 to 0.24 $g/m^2 \cdot s$ freshwater, with meaningful generation accessible at air temperatures as high as 15-20°C.

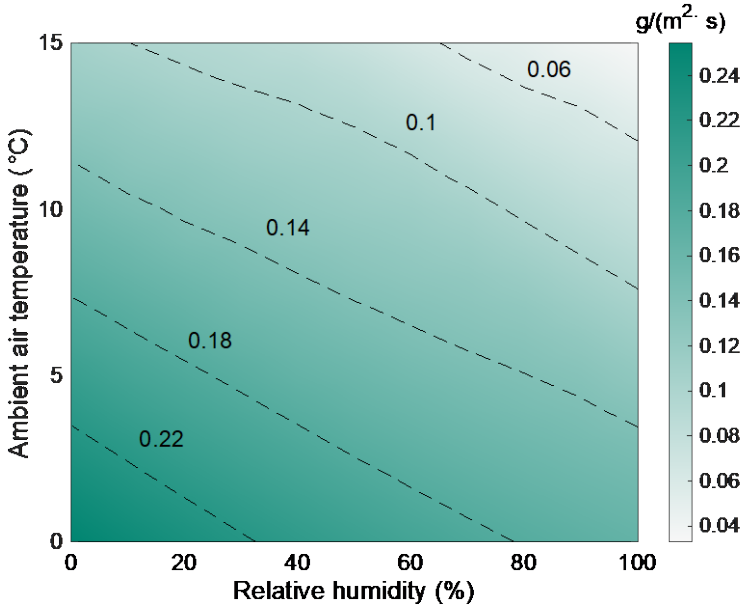

Figure S1. First-order thermodynamic prediction for the water production rate at the freezing point for 35g/L by radiative cooling freezing desalination at ideal case for different relative humidity and ambient temperatures.

3. Heat-Transfer Model of Experiment

The atmospheric emittance ε_{atm} calculated from $I_{sky}(\lambda)$. For this calculation, we used weather and location date to model $I_{sky}(\lambda)$ using the MODTRAN Web Application. Parameters used for the modelling included location, time and total precipitable water (TPW) in the atmosphere. For the experiment at Big Bear Lake on June 30th, 2020, the TPW is 11mm and the altitude was 7400 ft. For the experiment on May 28th, 2021, the TPW is 7.5mm. A clear, cloudless sky was observed and assumed for the model.

Heat-transfer simulations were performed in order to better understand convective and conductive loss mechanisms in the experiment, and to quantify $P_{cond+conv}$ and h_c as defined in Eq. (4). The model simulates the experimental setup in three dimensions with four objects: a thin

radiator, two layers of 12.5 um low-density polyethylene, surrounding air and the supporting polystyrene block as is shown in Figure S2A. We define the air temperature and the conductive properties of all objects and the value of the heat flux P_{out} that is leaving the radiator, allowing us to infer $P_{cond+conv}$ according to the radiator's temperature T. The outside boundaries of the system (shown at the top of Figure S2A are set to the air temperature. The simulation handles the fluid mechanics in the air pocket and the conduction in the polystyrene block and the radiator in order to determine the steady-state temperature T of the sample for each value of P_{out}. At the steady-state temperature, $P_{out} = P_{cond+conv} = Ah_c(T_{amb} - T)$. The result of this simulation is shown in Figure S2B as the blue line, whose slope is the simulation's prediction of the non-radiative heat transfer coefficient h_c. By linear regression we find a value of $h_c = 2.5$ W m^{-2} K^{-1} which is within the range between 2-4 W/m^2/K in the theoretical model in Figure 4 grey region and fits the observed data very well.

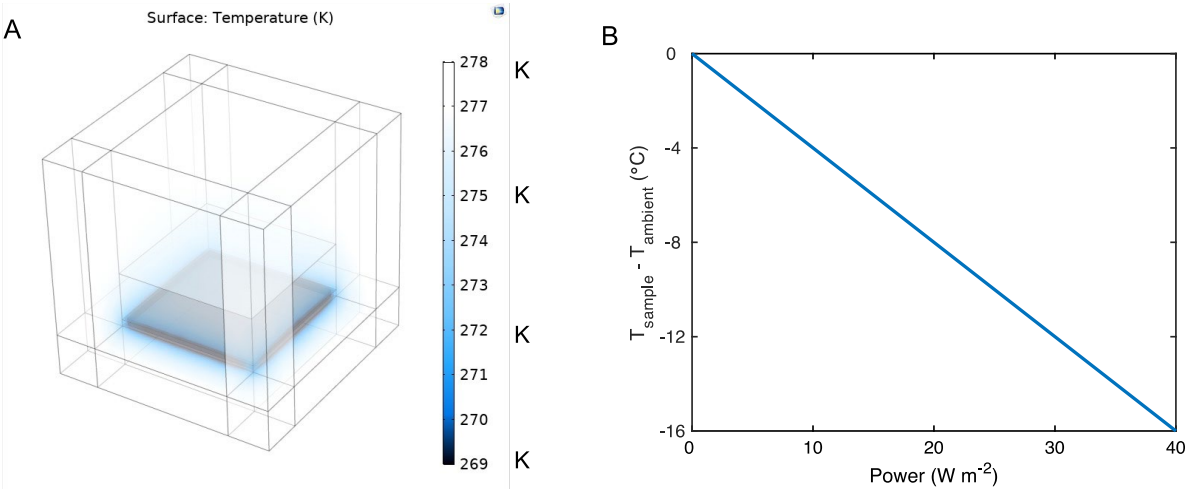

Figure S2. (A) A numerical (finite-element) heat transfer simulation of the apparatus and radiative cooler yields a temperature distribution within the geometry that takes into account non-radiative heat exchange in the apparatus. **(B)** The simulation calculation for $P_{cond+conv}$ as a

function of $T_{sample} - T_{ambient}$ (blue line) yields a value of $h_c = 2.5$ W m^{-2} K^{-1}, which is within the range between 2-4 W/m^2/K in our theoretical model to compare against experimental data in Figure 4 grey region.

We propose a theoretical model to explain the water temperature curve. Before freezing occurs, because of the high heat conductivity of aluminum as 205 W/m K and small thermal mass of salt water as 30 g, it's reasonable to assume that there is no heat loss between the cold plate and the salt water, so the saltwater and cold plate can be considered as a whole. Then the radiative power P_{rad} can be expressed as follows:

$$P_{net}\,\Delta t = (m_{Al}C_{Al} + m_s C_s)\,\Delta T \tag{7}$$

Here m_{Al} and m_s are the mass of the cold plate and saltwater and C_{Al} and C_s are the heat capacity of aluminum plate and saltwater. P_{net} can be calculated from Equation (1) with the air transfer coefficient h_c within the range of 2-4 W/ m^2/K. The mass of cold plate and saltwater is 410 g and 30 g separately. To fit the curve, we assume that the initial temperature of the radiative cooler is the same as the ambient temperature measured during the experiment and we choose ΔT equals =0.01 K each time and calculate time step Δt to cool down for this small temperature drop according to Eq. (7). Then we use the corresponding experimental ambient temperature after each time step as the input ambient temperature for the next ΔT drop to calculate the new time step Δt. By progressing through these time steps, we model the temperature drop corresponding to time as is shown in the Figure 4 grey regions, which fits very well with the experimental value. After the transition point, new ice particles will form. This formation process can be expressed as follows:

$$P_{net}\,\Delta t - S \times H_f\,\Delta t = (m_{Al} \times C_{Al} + m_s \times C_s)\,\Delta T \tag{8}$$

The rate of mass transferred from liquid to solid (S) depends upon the nucleation rate S_n, the mass of the single crystal S_m according to the relationship.[1,2]

$$S = S_n S_m \tag{9}$$

where S_n is the nucleation rate given as[3]

$$S_n = \frac{RT_b}{h} exp(\frac{A(T_f)^2}{T_b(T_f - T_b)^2}),\ T_b < T_f. \tag{10}$$

Here T_b is the bulk water temperature, T_f is the freezing temperature of brine used, R is the ideal gas constant, h is Planck's constant and A is an empirical constant which may be calculated by assuming that $S_n = 1$ at nucleation. Further assuming that the crystals are spherical, the mass of single crystal is obtained from

$$S_m = 4\pi r \rho_s / 3 \tag{11}$$

where ρ_s is the density of ice, r_s is the average diameter of the single ice crystal and we assume it equals half of the final crystal size, $r = 0.5\ D_p$.

The rate of change of diameter D_p of a single crystal relates with the difference between the temperature T_i of the ice/liquid interface and temperature T_b of the bulk liquid,

$$\frac{dD_p}{dt} = \frac{G}{D_p}(T_i - T_b) \tag{12}$$

where G is the rate constant defined according to driving force ratio E_x as

$$G = 0.6129 \times 10^{-8} E_x. \tag{13}$$

E_x is dependent on salt concentration W_l of the bulk liquid according to

$$E_x = 1/\{1 + 77 W_l/(1 - W_l)\}. \tag{14}$$

Finally, The ice/liquid interface temperature T_i is defined in terms of the liquid bulk temperature and the driving force ratio using

$$T_i = (T_f - T_b)E_x + T_b \quad (15)$$

To fit the curve, we discretize the temperature decrease as $\Delta T = 0.01$ K and calculate the time step Δt needed to cool down for this temperature drop according to Eq. (8). The rate of mass formation S can be calculated from Eqs. (9-15). We then use the corresponding experimental ambient temperature after each time step as the input ambient temperature for the next ΔT drop to calculate the new time step Δt. Using this approach, we can iteratively model the temperature drop corresponding to time as is shown in the grey regions of Figure 4, which map well to the experimentally measured values.

4. Supercooling temperatures at different salinities

To phenomenologically assess the degree of supercooling one can expect in our apparatus during freezing as a function of input salinity, we conducted a controlled lab experiment of the apparatus whereby the supercooling temperature of saltwater was measured for different input salinities. The results, shown in Figure S3, highlight that the supercooling temperature is observed to be roughly linear function as a function of salinity over the salinities and temperature range of interest and relevance to our experiments. This then allows us to establish an expected supercooling temperature and freezing onset temperature for our model.

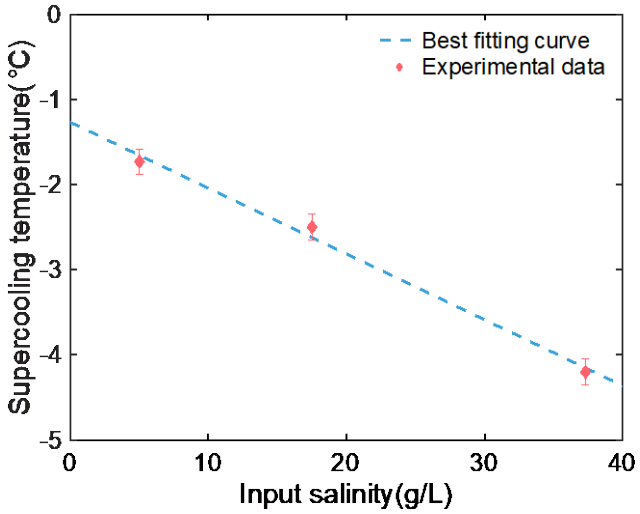

Figure S3. Measured supercooling temperatures for different input salinities during the freezing desalination process in our apparatus.

5. Desalination steps to get freshwater for different initial input salinity

Figure S4 shows the final freshwater production after one stage desalination process according to different initial input salinity. The higher initial salinity, after one stage desalination process, the higher final salinity as well as lower water production rate.

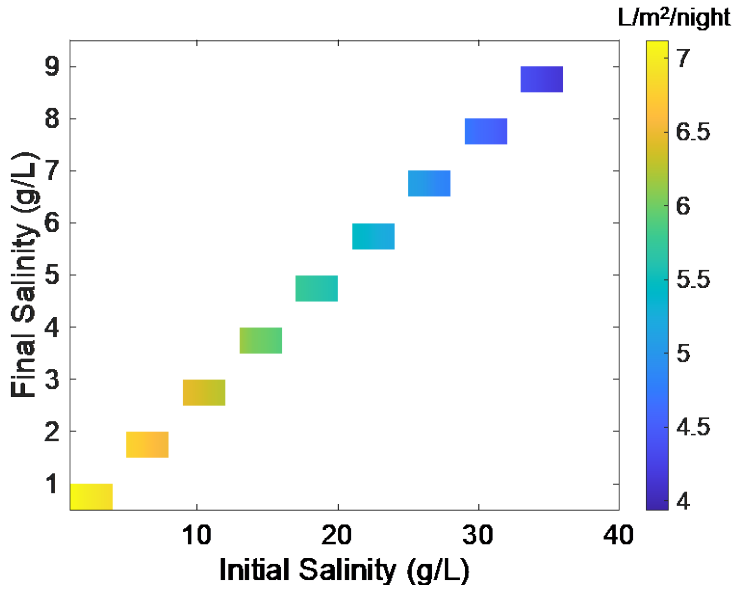

Figure S4. Simulated freshwater production after one stage desalination process according to different initial input salinity

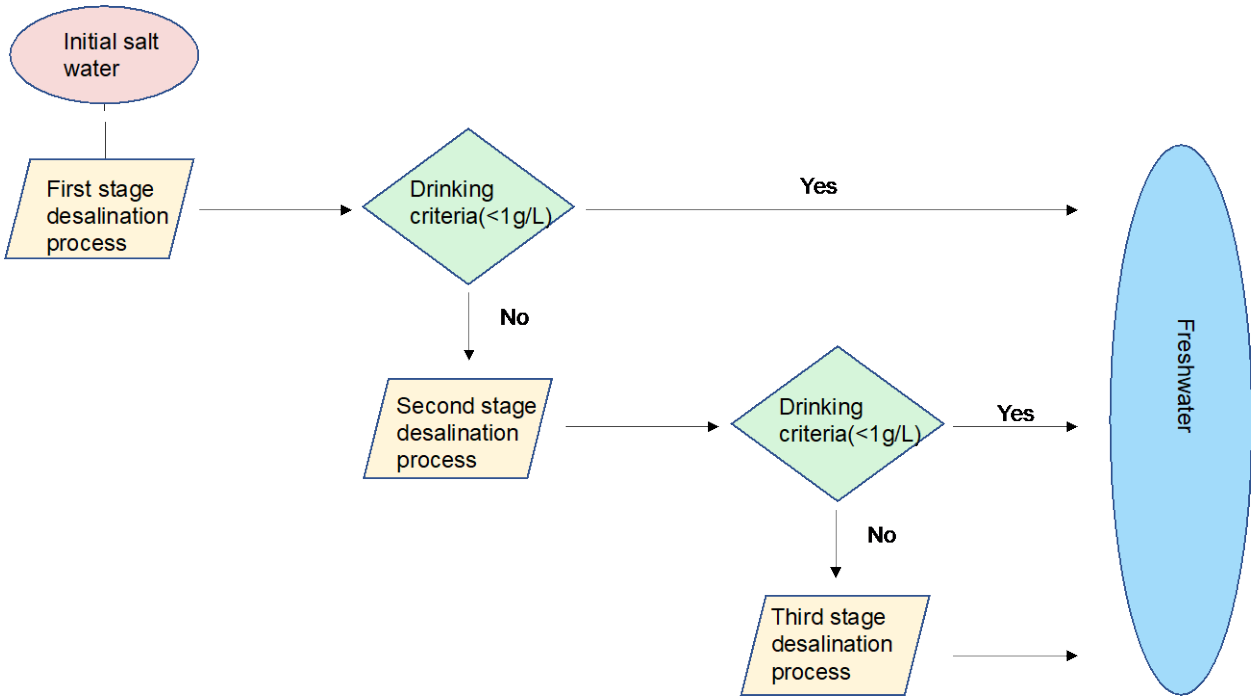

Figure S5. Flow chart showing the decision flow in the developed model to determine the number of radiative cooling freezing desalination stages needed for a given initial input salinity

Figure S5 shows the radiative cooling freezing desalination stages according to different initial input salinity. Figure 4F uses this flowchart to calculate the amount of freshwater production based on different initial input salinity. For input salinities close to seawater, it may take three stages to get freshwater based on our current implementation. Lower salinity of initial saltwater may require only one or two stages.

6. Levelized cost of water (LCW) analysis

To explore the economic factor of this method, we performed a preliminary levelized cost of water (LCW) analysis based on the current implementation of the radiative cooling freezing desalination system. The following general formulas are applied to calculate the LCW of the proposed passive freezing desalination system[4]

$$LCW(\$/m^3) = \frac{C_0 + \sum_{t=1}^{25} \frac{OM_t + F_t}{(1+i_t)^t}}{\sum_{t=1}^{25} \frac{W_t}{(1+i_t)^t}}$$

Here C_0 represents the capital cost, OM_t represents annual cost (including chemical and overhead), F_t represents the decommissioning cost and W_t is the water production. We assume that the project / product lifetime is 25 years, and the interest rate of financing(i_t) is assumed to be 3% and for simplicity we assume no decommissioning cost ($F_t = 0$).

We calculate a capital cost of \$10.7/m^2. As inputs we include aluminum foil from Walmart (item 550050985) at \$0.5/m^2, 3M Scotch tape from Walmart (item 565092890) at \$0.1/m^2 and low-density polyethylene from Walmart (item 551257829) at \$0.1/m^2. We obtained the cold plate with from a vendor in China at a cost of \$10 /m^2. This estimate is highly conservative as it assumes

as raw costs the price of components at low volumes from consumer retailers. The annual operational cost is calculated a value of \$0.821 /m^2. This includes electricity costs of \$0.011/m^2/year, filter cost at 0.81 \$/m^2/year. Filter is made from 3d printer PLA filament from Amazon (item PLA175RBLK). For the current water production of 3.3 L/day/m^2, the LCW cost is \$1.19/m^3, as is shown in table S1, which is price compatible with solar desalination at 0.8-1.5 \$/m^3. [4]

interest rate(i_t)	Capital cost (C_0)			Annual cost (OM_t)	
	Radiative cooler	Low-density polyethylene	Metal plate with tube	Electricity	Filter
3%	\$0.6/m^2	\$0.1 /m^2	\$10/m^2	\$0.011/m^2	\$0.81/m^2

Table S1. Inputs for levelized cost of water (LCW) estimate for our radiative cooling freezing desalination system

Figure S6 shows LCW estimates from the seawater by radiative cooling freezing desalination method against different daily production rate. For a constant cost of desalination system, the higher production rate, the lower LCW we can get. The current LCW cost of the radiative cooling freezing system is \$1.19/m^3, which is comparable with solar desalination and reverse osmosis. With improved performance, including those identified in the calculations for

Figure 5B and 5D, and economies of scale, this approach holds the potential to compare favorably with both thermal and membrane desalination systems.

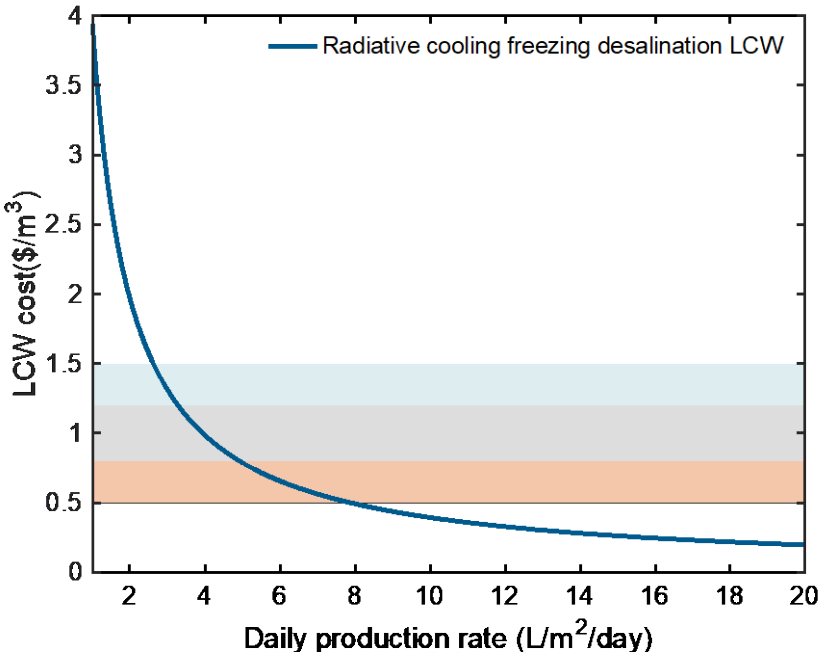

Figure S6. Levelized cost of water (LCW) estimates of radiative cooling drive freezing desalination for different production rates. The results indicate that, based on current performance, the system holds the potential to compete favorably with solar desalination with further improvements may also compare well with membrane desalination in the climate zones identified in Figure 5D.

7. Potential water production in different climates in a vacuum system

For seawater desalination with initial input salinity at 35 g/L, based on the current implementation, which is current cold plate, scotch tape as the emitter, no supercooling as well as vacuum system achieved in other literature[5], the performance of this system at different ambient

temperatures and relative humidities is shown in Figure S7A. The amount of water produced by radiative cooling freezing desalination on a daily basis based on the same assumptions from January to December for the cities of five different climate zones are shown in Figure S7B.

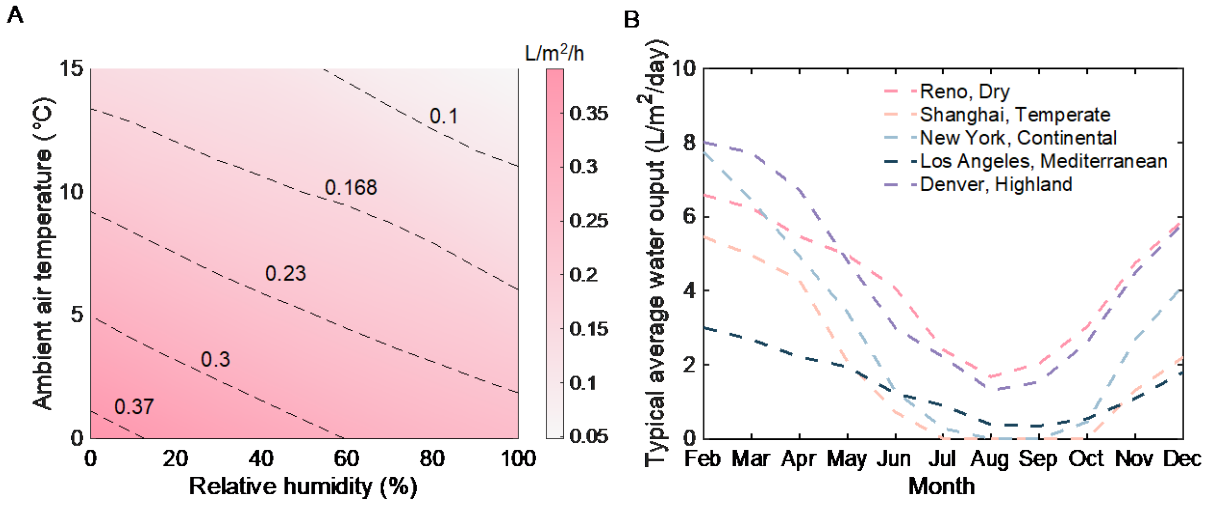

Figure S7. **(A)** Prediction of the amount of water produced by radiative cooling freezing desalination in the scenario where the non-radiative heat transfer coefficient is maximally suppressed (h_c=0) for different relative humidity and ambient temperatures. **(B)** Prediction of the amount of water with this method for the cities of five different climate zones in the potential real case when the non-radiative heat transfer coefficient h_c=0.

8. Annual average daily water production for different climate zones

The annual average daily water production at different initial input salinity with radiative cooling freezing desalination method for the identified cities in five different climate zones is shown in Table S2. The dry climate and highland climate are notably the best weather conditions for this method as it has the highest annual average daily production compared with other weather

conditions. However, with further improvements in the system, performance and associated LCW (Figure S6) may be competitive across all the climate zones shown.

Initial Salinity	Climate zone	Dry-Reno	Temperate-Shanghai	Continental-New York	Mediterranean-LA	Highland-Denver
35 g/L	Ideal annual average daily production	11.21 L/m^2	5.03 L/m^2	7.8 L/m^2	3.9 L/m^2	11.57 L/m^2
35 g/L	Real annual average daily production	2 L/m^2	0.43 L/m^2	1.16 L/m^2	0 L/m^2	2.27 L/m^2
17.5 g/L	Ideal annual average daily production	12.4 L/m^2	5.93 L/m^2	9 L/m^2	5 L/m^2	12.9 L/m^2
17.5 g/L	Real annual average daily production	2.57 L/m^2	0.65 L/m^2	1.4 L/m^2	0.2 L/m^2	2.77 L/m^2

Table S2. Prediction of annual average daily water production with passive freezing desalination for the cities of five different climate zones.

9. Potential ways to further improve water quality

Prior work has shown the washing process applied post crystallization to enhance crystal quality. Besides the washing method, which we implemented, a sweating process has also been shown to be an effective post treatment method to remove brine trapped within ice crystals.[6,7] Mandri et al. investigated the sweating process through one cycle of indirect freezing desalination[8]. It was observed that salinity of the saline solution was substantially reduced from 35 g/kg to 0.5 g/kg at 0 °C post optimization of the freezing condition and sweating step.

Addition of ice seeds to induce nucleation was also applied to enhance product quality as well as achieve better control over nucleation. Without ice seed, the water usually has a supercooling state, which is beneficial to form dendritic ice crystals. At the end of the supercooling stage, greater impurities get trapped between dendritic ice crystals, which in turn, imply lower quality of water[9]. Addition of ice seed will terminate the supercooling state immediately and ice crystals are formed shortly.[10,11] Scientists have introduced ice seed for the freezing desalination process to avoid supercooling and increase water quality.[10,12,13]

10. Transmittance of polyethylene film used

Multi-layer insulation to improve cooling performance has been widely used in radiative cooling experiments where there is a deep sub-ambient temperature regime one is trying to reach. In this regime, the insulation benefits of two layers (a reduced non-radiative coefficient of heat exchange) can outweigh the transmission loss due to additional layers of PE. This was observed in Trombe's[14] original demonstrations (1967) which employed this form of multi-layer insulation. Two layers of PE films will form an air pocket which will provide better thermal insulation

compared with single layer PE film. As is shown in Figure S8A, the infrared transmittance of PE film towards the zenith is ~92%, with two layers bringing it down to approximately 84%. For our application, the advantage of providing well thermal insulation will outweigh its effects influencing the infrared transmittance, causing a higher cooling power compared with the single layer PE film. As is shown in Figure S8B, we calculate the net cooling power vs. temperature for a selective radiative cooler beneath a single layer of LDPE and one under two layers of LDPE. As expected, at temperatures near the air temperature, a single layer of LDPE is superior as the loss in IR transmittance is more important than any gain in conductive or convective isolation. However, as one proceeds to lower sub-ambient temperatures, the benefit of the reduced coefficient of conductive and convective heat exchange results in net cooling power of the two-layer LDPE window outperforming that of the single-layer LDPE configuration. This begins within a few °C below ambient and is even more important as one reaches lower temperatures.

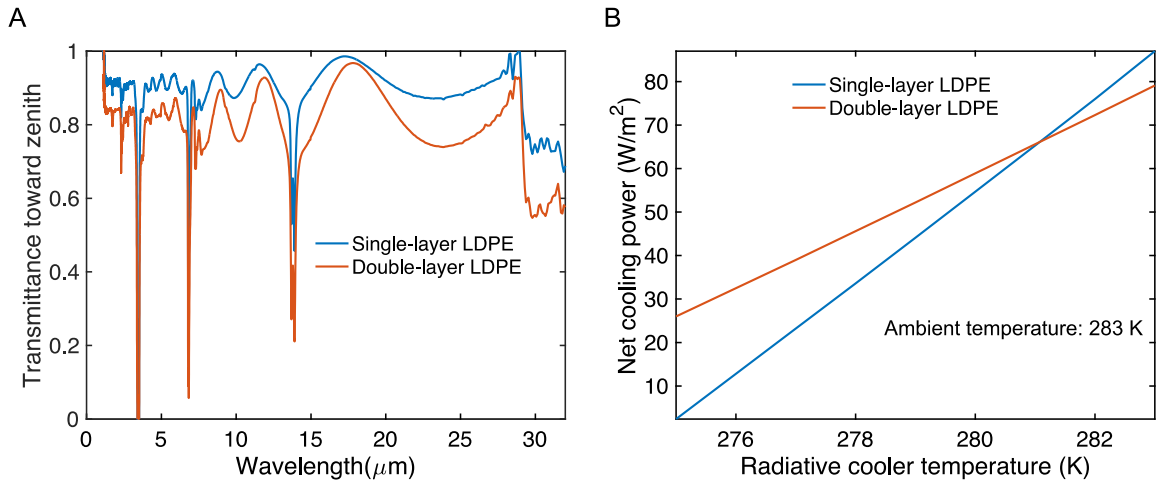

Figure S8. (**A)** Experimentally measured transmittance of single and double-layer 12.5 um-thick polyethylene films used in our experiments at zenith (0° angle of incidence). (**B)** Net radiative

cooling power vs. radiative cooling temperature for a selective radiative cooler beneath a single layer of LDPE and one under two layers of LDPE

5.5 References

1. Shannon, M.A., Bohn, P.W., Elimelech, M., Georgiadis, J.G., Mariñas, B.J., and Mayes, A.M. (2008). Science and technology for water purification in the coming decades. Nature *452*, 301–310. 10.1038/nature06599.

2. Stephens, G.L., Slingo, J.M., Rignot, E., Reager, J.T., Hakuba, M.Z., Durack, P.J., Worden, J., and Rocca, R. (2020). Earth's water reservoirs in a changing climate. Proc Math Phys Eng Sci *476*, 20190458. 10.1098/rspa.2019.0458.

3. Jones, E., Qadir, M., van Vliet, M.T.H., Smakhtin, V., and Kang, S. (2019). The state of desalination and brine production: A global outlook. Science of The Total Environment *657*, 1343–1356. 10.1016/j.scitotenv.2018.12.076.

4. Schiermeier, Q. (2008). Water: Purification with a pinch of salt. Nature *452*, 260–261. 10.1038/452260a.

5. Vidic, R.D., Brantley, S.L., Vandenbossche, J.M., Yoxtheimer, D., and Abad, J.D. (2013). Impact of Shale Gas Development on Regional Water Quality. Science *340*. 10.1126/science.1235009.

6. Brantley, S.L., Vidic, R.D., Brasier, K., Yoxtheimer, D., Pollak, J., Wilderman, C., and Wen, T. (2018). Engaging over data on fracking and water quality. Science *359*, 395–397. 10.1126/science.aan6520.

7. Kim, B., Kwak, R., Kwon, H.J., Pham, V.S., Kim, M., Al-Anzi, B., Lim, G., and Han, J. (2016). Purification of High Salinity Brine by Multi-Stage Ion Concentration Polarization Desalination. Sci Rep *6*, 31850. 10.1038/srep31850.

8. Lattemann, S., and Höpner, T. (2008). Environmental impact and impact assessment of seawater desalination. Desalination *220*, 1–15. 10.1016/j.desal.2007.03.009.

9. Vengosh, A., Jackson, R.B., Warner, N., Darrah, T.H., and Kondash, A. (2014). A Critical Review of the Risks to Water Resources from Unconventional Shale Gas Development and Hydraulic Fracturing in the United States. Environ. Sci. Technol. *48*, 8334–8348. 10.1021/es405118y.

10. Palomar, P., and Losada, I.J. (2011). Impacts of Brine Discharge on the Marine Environment. Modelling as a Predictive Tool (IntechOpen) 10.5772/14880.

11. Wenten, I.G. and Khoiruddin (2016). Reverse osmosis applications: Prospect and challenges. Desalination *391*, 112–125. 10.1016/j.desal.2015.12.011.

12. Tong, T., and Elimelech, M. (2016). The Global Rise of Zero Liquid Discharge for Wastewater Management: Drivers, Technologies, and Future Directions. Environ. Sci. Technol. *50*, 6846–6855. 10.1021/acs.est.6b01000.

13. Greenlee, L.F., Lawler, D.F., Freeman, B.D., Marrot, B., and Moulin, P. (2009). Reverse osmosis desalination: water sources, technology, and today's challenges. Water Res *43*, 2317–2348. 10.1016/j.watres.2009.03.010.

14. Ghaffour, N., Missimer, T.M., and Amy, G.L. (2013). Technical review and evaluation of the economics of water desalination: Current and future challenges for better water supply sustainability. Desalination *309*, 197–207. 10.1016/j.desal.2012.10.015.

15. Borsani, R., and Rebagliati, S. (2005). Fundamentals and costing of MSF desalination plants and comparison with other technologies. Desalination *182*, 29–37. 10.1016/j.desal.2005.03.007.

16. Sommariva, C., Hogg, H., and Callister, K. (2003). Cost reduction and design lifetime increase in thermal desalination plants: thermodynamic and corrosion resistance combined analysis for heat exchange tubes material selection. Desalination *158*, 17–21. 10.1016/S0011-9164(03)00427-2.

17. Darwish, M.A., and Al-Najem, N.M. (1987). Energy consumptions and costs of different desalting systems. Desalination *64*, 83–96. 10.1016/0011-9164(87)90087-7.

18. Ghaffour, N., Bundschuh, J., Mahmoudi, H., and Goosen, M.F.A. (2015). Renewable energy-driven desalination technologies: A comprehensive review on challenges and potential applications of integrated systems. Desalination *356*, 94–114. 10.1016/j.desal.2014.10.024.

19. Elimelech, M., and Phillip, W.A. (2011). The Future of Seawater Desalination: Energy, Technology, and the Environment. Science *333*, 712–717. 10.1126/science.1200488.

20. Tao, P., Ni, G., Song, C., Shang, W., Wu, J., Zhu, J., Chen, G., and Deng, T. (2018). Solar-driven interfacial evaporation. Nat Energy *3*, 1031–1041. 10.1038/s41560-018-0260-7.

21. Wang, Z., Horseman, T., Straub, A.P., Yip, N.Y., Li, D., Elimelech, M., and Lin, S. (2019). Pathways and challenges for efficient solar-thermal desalination. Science Advances *5*, eaax0763. 10.1126/sciadv.aax0763.

22. Zhou, L., Tan, Y., Wang, J., Xu, W., Yuan, Y., Cai, W., Zhu, S., and Zhu, J. (2016). 3D self-assembly of aluminium nanoparticles for plasmon-enhanced solar desalination. Nature Photon *10*, 393–398. 10.1038/nphoton.2016.75.

23. Bae, K., Kang, G., Cho, S.K., Park, W., Kim, K., and Padilla, W.J. (2015). Flexible thin-film black gold membranes with ultrabroadband plasmonic nanofocusing for efficient solar vapour generation. Nat Commun *6*, 10103. 10.1038/ncomms10103.

24. Zhou, L., Tan, Y., Ji, D., Zhu, B., Zhang, P., Xu, J., Gan, Q., Yu, Z., and Zhu, J. (2016). Self-assembly of highly efficient, broadband plasmonic absorbers for solar steam generation. Science Advances *2*, e1501227. 10.1126/sciadv.1501227.

25. Zhang, L., Xing, J., Wen, X., Chai, J., Wang, S., and Xiong, Q. (2017). Plasmonic heating from indium nanoparticles on a floating microporous membrane for enhanced solar seawater desalination. Nanoscale *9*, 12843–12849. 10.1039/C7NR05149B.

26. Yi, L., Ci, S., Luo, S., Shao, P., Hou, Y., and Wen, Z. (2017). Scalable and low-cost synthesis of black amorphous Al-Ti-O nanostructure for high-efficient photothermal desalination. Nano Energy *41*, 600–608. 10.1016/j.nanoen.2017.09.042.

27. Ye, M., Jia, J., Wu, Z., Qian, C., Chen, R., O'Brien, P.G., Sun, W., Dong, Y., and Ozin, G.A. (2017). Synthesis of Black TiOx Nanoparticles by Mg Reduction of TiO2 Nanocrystals and their Application for Solar Water Evaporation. Advanced Energy Materials *7*, 1601811. 10.1002/aenm.201601811.

28. Zielinski, M.S., Choi, J.-W., La Grange, T., Modestino, M., Hashemi, S.M.H., Pu, Y., Birkhold, S., Hubbell, J.A., and Psaltis, D. (2016). Hollow Mesoporous Plasmonic Nanoshells for Enhanced Solar Vapor Generation. Nano Lett. *16*, 2159–2167. 10.1021/acs.nanolett.5b03901.

29. Ni, G., Li, G., Boriskina, S.V., Li, H., Yang, W., Zhang, T., and Chen, G. (2016). Steam generation under one sun enabled by a floating structure with thermal concentration. Nat Energy *1*, 1–7. 10.1038/nenergy.2016.126.

30. Li, Y., Gao, T., Yang, Z., Chen, C., Luo, W., Song, J., Hitz, E., Jia, C., Zhou, Y., Liu, B., et al. (2017). 3D-Printed, All-in-One Evaporator for High-Efficiency Solar Steam Generation under 1 Sun Illumination. Advanced Materials *29*, 1700981. 10.1002/adma.201700981.

31. Kashyap, V., Al-Bayati, A., Sajadi, S.M., Irajizad, P., Wang, S.H., and Ghasemi, H. (2017). A flexible anti-clogging graphite film for scalable solar desalination by heat localization. J. Mater. Chem. A *5*, 15227–15234. 10.1039/C7TA03977H.

32. Zhao, F., Zhou, X., Shi, Y., Qian, X., Alexander, M., Zhao, X., Mendez, S., Yang, R., Qu, L., and Yu, G. (2018). Highly efficient solar vapour generation via hierarchically nanostructured gels. Nature Nanotech *13*, 489–495. 10.1038/s41565-018-0097-z.

33. Chavan, S., Park, D., Singla, N., Sokalski, P., Boyina, K., and Miljkovic, N. (2018). Effect of Latent Heat Released by Freezing Droplets during Frost Wave Propagation. Langmuir *34*, 6636–6644. 10.1021/acs.langmuir.8b00916.

34. Bartholin, T., Haubold, P., Godicchen, M., and Bartholin, E. (1661). Thomae Bartholini de nivis usu medico observationes variae: accessit D. Erasmi Bartholini De figura nivis dissertatio ; cum operum authoris catalogo (Typis Matthiae Godicchii, Sumptibus Petri Haubold, Bibl).

35. Chiu, S.-Y., Fan, L.-T., and Akins, R.G. (1969). Experimental Study of the Ice-Making Operation in the Inversion Desalination Freezing Process. Ind. Eng. Chem. Proc. Des. Dev. *8*, 347–356. 10.1021/i260031a009.

36. Beier, N., Sego, D., Donahue, R., and Biggar, K. (2007). Laboratory investigation on freeze separation of saline mine waste water. Cold Regions Science and Technology *48*, 239–247. 10.1016/j.coldregions.2006.12.002.

37. Khawaji, A.D., Kutubkhanah, I.K., and Wie, J.-M. (2008). Advances in seawater desalination technologies. Desalination *221*, 47–69. 10.1016/j.desal.2007.01.067.

38. Rich, A., Mandri, Y., Mangin, D., Rivoire, A., Abderafi, S., Bebon, C., Semlali, N., Klein, J.-P., Bounahmidi, T., Bouhaouss, A., et al. (2012). Sea water desalination by dynamic layer melt

crystallization: Parametric study of the freezing and sweating steps. Journal of Crystal Growth *342*, 110–116. 10.1016/j.jcrysgro.2011.03.061.

39. Cole, D.M., and Shapiro, L.H. (1998). Observations of brine drainage networks and microstructure of first-year sea ice. Journal of Geophysical Research: Oceans *103*, 21739–21750. 10.1029/98JC01264.

40. Williams, P.M., Ahmad, M., Connolly, B.S., and Oatley-Radcliffe, D.L. (2015). Technology for freeze concentration in the desalination industry. Desalination *356*, 314–327.

41. Fujioka, R., Wang, L.P., Dodbiba, G., and Fujita, T. (2013). Application of progressive freeze-concentration for desalination. Desalination *319*, 33–37. 10.1016/j.desal.2013.04.005.

42. Badawy, S.M. (2016). Laboratory freezing desalination of seawater. Desalination and Water Treatment *57*, 11040–11047. 10.1080/19443994.2015.1041163.

43. Xie, C., Zhang, L., Liu, Y., Lv, Q., Ruan, G., and Hosseini, S.S. (2018). A direct contact type ice generator for seawater freezing desalination using LNG cold energy. Desalination *435*, 293–300. 10.1016/j.desal.2017.04.002.

44. Raman, A.P., Anoma, M.A., Zhu, L., Rephaeli, E., and Fan, S. (2014). Passive radiative cooling below ambient air temperature under direct sunlight. Nature *515*, 540–544. 10.1038/nature13883.

45. Chen, Z., Zhu, L., Raman, A., and Fan, S. (2016). Radiative cooling to deep sub-freezing temperatures through a 24-h day–night cycle. Nat Commun *7*, 13729. 10.1038/ncomms13729.

46. Incropera, F.P., and Incropera, F.P. eds. (2007). Fundamentals of heat and mass transfer 6th ed. (John Wiley).

47. Zhao, D., Aili, A., Zhai, Y., Xu, S., Tan, G., Yin, X., and Yang, R. (2019). Radiative sky cooling: Fundamental principles, materials, and applications. Applied Physics Reviews *6*, 021306. 10.1063/1.5087281.

48. Hossain, M.M., and Gu, M. (2016). Radiative Cooling: Principles, Progress, and Potentials. Advanced Science *3*, 1500360. 10.1002/advs.201500360.

49. Li, W., Dong, M., Fan, L., John, J.J., Chen, Z., and Fan, S. (2021). Nighttime Radiative Cooling for Water Harvesting from Solar Panels. ACS Photonics *8*, 269–275. 10.1021/acsphotonics.0c01471.

50. Fournier, J., Grange, J.L., and Vergara, S. (1974). Water desalination by natural freezing. Desalination *15*, 167–175. 10.1016/S0011-9164(00)82080-9.

51. Mandal, J., Mandal, S., Brewer, J., Ramachandran, A., and Raman, A.P. (2021). Radiative Cooling and Thermoregulation in the Earth's Glow. arXiv:2006.11931 [physics].

52. Zhang, Y., Anim-Danso, E., Bekele, S., and Dhinojwala, A. (2016). Effect of Surface Energy on Freezing Temperature of Water. ACS Appl. Mater. Interfaces *8*, 17583–17590. 10.1021/acsami.6b02094.

53. Chang, J., Zuo, J., Lu, K.-J., and Chung, T.-S. (2016). Freeze desalination of seawater using LNG cold energy. Water Res *102*, 282–293. 10.1016/j.watres.2016.06.046.

54. Yang, Y., Lu, Y., Guo, J., and Zhang, X. (2017). Application of freeze concentration for fluoride removal from water solution. Journal of Water Process Engineering *19*, 260–266. 10.1016/j.jwpe.2017.05.009.

55. Melak, F., Ambelu, A., Laing, G.D., and Alemayehu, E. (2017). Freeze Desalination as Point of Use Water Treatment Technology: A Case of Chromium (VI) Removal from Water. Proceedings *2*, 173. 10.3390/ecws-2-04942.

56. Shirai, Y., Wakisaka, M., Miyawaki, O., and Sakashita, S. (1998). Conditions of producing an ice layer with high purity for freeze wastewater treatment. Journal of food engineering.

57. Shirai, Y., Wakisaka, M., Miyawaki, O., and Sakashita, S. (1999). Effect of seed ice on formation of tube ice with high purity for a freeze wastewater treatment system with a bubble-flow circulator. Water Research *33*, 1325–1329. 10.1016/S0043-1354(98)00335-2.

58. Luo, C., Chen, W., and Han, W. (2010). Experimental study on factors affecting the quality of ice crystal during the freezing concentration for the brackish water. Desalination *260*, 231–238. 10.1016/j.desal.2010.04.018.

59. Wang, P., and Chung, T.-S. (2012). A conceptual demonstration of freeze desalination-membrane distillation (FD-MD) hybrid desalination process utilizing liquefied natural gas (LNG) cold energy. Water Res *46*, 4037–4052. 10.1016/j.watres.2012.04.042.

60. Liu, L., Fujii, T., Hayakawa, K., and Miyawaki, O. (1998). Prevention of Initial Supercooling in Progressive Freeze-concentration. Bioscience, Biotechnology, and Biochemistry *62*, 2467–2469. 10.1271/bbb.62.2467.

61. Wang, W., Shi, Y., Zhang, C., Hong, S., Shi, L., Chang, J., Li, R., Jin, Y., Ong, C., Zhuo, S., et al. (2019). Simultaneous production of fresh water and electricity via multistage solar photovoltaic membrane distillation. Nat Commun *10*, 3012. 10.1038/s41467-019-10817-6.

62. Durkaieswaran, P., and Murugavel, K.K. (2015). Various special designs of single basin passive solar still – A review. Renewable and Sustainable Energy Reviews *49*, 1048–1060. 10.1016/j.rser.2015.04.111.

63. Wang, P. (2018). Emerging investigator series: the rise of nano-enabled photothermal materials for water evaporation and clean water production by sunlight. Environ. Sci.: Nano *5*, 1078–1089. 10.1039/C8EN00156A.

64. Kaya, A., Tok, M.E., and Koc, M. (2019). A Levelized Cost Analysis for Solar-Energy-Powered Sea Water Desalination in The Emirate of Abu Dhabi. Sustainability *11*, 1691. 10.3390/su11061691.

Chapter 6: High-efficiency dew condensation and collection using hydrophilic radiative cooling surfaces

6.1 Introduction

Water scarcity is one of the most challenging issues facing humankind this century. Over fifty percent of the global population faces a shortage of water today, with that number expected to reach two-thirds by 2025[1,2]. Although desalination can facilitate the use of sea water, landlocked places are unable to take advantage of this approach to fresh water generation. Atmospheric water harvesting has thus attracted great attention for potable freshwater generation because of its ease of access and the large amount of freshwater resources accessible in our atmosphere[3].

Current atmospheric water harvesting methods are typically based on refrigeration, exploiting a cooled surface to cool the air below dew point powered by electricity[4,5]. However, because of the large enthalpy of condensation, active cooling methods impose large electricity requirements which are unfavorable from both a cost and carbon emissions point of view. Instead of cooling the surface to increase the local relative humidity (RH), a significant body of research has explored atmospheric water harvesting materials with the ability to extract water vapor from air spontaneously such as hygroscopic materials[6–8] , silica gels[9–11] and zeolites[12–14]. However, the fundamental challenge remains in the high energy consumption to release the water because of the high affinity between the water and the harvesting material. Metal organic framework (MOF)-based materials[15–17] were demonstrated to take up water at a relatively low RH and release water with small temperature increase through tailored material modifications. However, most viable MOFs have been challenging to synthesize on a commercial scale, limiting their potential for large-

scale, cost-effective water production. Furthermore, the long-term stability through cycling, as well as shaping/processing of MOFs are important limitations to future practical applications[3].

With a view towards overcoming the energy constraints associated with condensing atmospheric water vapor, and building on developments in passive radiative cooling[18–27], dew condensation on radiatively-cooled surfaces has been investigated in recent years[16–19]. In this approach, sky-facing surfaces radiate their heat as thermal radiation into cold space through an atmospheric window in the long-wave infrared part of the electromagnetic spectrum between 8–13 μm. The cooling effect cools down the surface to below the dew point thereby facilitating condensation. Due to its underlying mechanism, passive condensation can in principle be achieved in a broad range of weather conditions. Recently, through proper spectral engineering, a range of high emittance radiative cooling materials[20,22,28–30] have been demonstrated, including a low-cost, high emittance radiative cooler that experimentally achieved a 11 °C temperature drop[29].

Although dew condensation through radiative cooling has been experimentally explored[31,32] with a range of materials chosen for their optical properties, comparatively little attention has been paid to the surface properties of the radiative cooling surface to facilitate both condensation and collection of generated water. For condensation applications, the water droplet usually attaches on the surface and requires active energy to remove it. Engineering surfaces with water nucleation and removal attracted much attention. Recent work used a hydrophilic Al foil as the condenser to increase the condensation efficiency[33]. However strong adhesion between water and the Al foil surface makes it challenging to collect the condensed water, necessitating a weighing approach to infer the actual water condensed. For highly saturated vapors (relative humidities > 95%), another recent paper demonstrated the utility of superhydrophobic coatings[34] which can achieve self-removal of harvested dew through its strongly repelling water

characteristics. While intriguing, these recent works focused on condensing vapor from a separate source, typically involving high relative humidities in the introduced water vapor. By contrast, for atmospheric water generation, the surface requires both high water condensation efficiency as well as high water removal efficiency, which previous works have not demonstrated. Indeed, hydrophilic surfaces will typically have a high condensation rate while hydrophobic surfaces can facilitate high water removal efficiency. A potential solution to this challenge lies in the recent development of slippery liquid-infused porous surfaces (SLIPS)[35–40] consisting of a film of lubricating liquid locked in place by a micro/nanoporous substrate because of capillary action. Although SLIPS have shown exceptional high water condensation efficiency and water collection efficiency at the same time, in the context of water harvesting they have only been used for fog harvesting.

In this chapter, we experimentally demonstrate high-efficiency atmospheric water harvesting driven by hydrophilic slippery radiative cooling surface (SRCs) with water nucleation and removal functions. We fabricate a hydrophilic slippery radiative cooling surface by incorporating the hydroxy PDMS-25 oil into the hierarchically porous poly(vinylidene fluoride-co- hexafluoropropene(P(VdF-HFP). To further increase the water collection efficiency, we optimize our system with a vertical surface, allowing water collection on both sides of the surface. We experimentally demonstrate that we collected 25 g/m^2 atmospheric water over 6h of outdoor nighttime testing at RH of 65% and as high as 45 $g/m^2/h$ water at RH of 95% with extraordinarily high efficiency, nearing the thermodynamic limit. Our results suggest that dew condensation via radiative cooling, in addition to being of scientific interest, may in fact emerge as a practical technology for water harvesting.

6.2 Results and Discussion

System design and working principle

Conventional approaches to dew condensation enabled by radiative cooling have utilized a flat or tilted sky-facing surface. However, in addition to condensing the water, collection has not been optimized, with droplets typically remaining immobile on the surface and manually collected at the end of a fixed time period. We thus introduce multi-functional hydrophilic slippery radiative cooling surfaces (SRCs). By radiatively cooling themselves, the SRCs passively cools down below the ambient air around the surfaces, which in turn, leads to condensation on the surfaces. The hydrophilic nature of the surface promotes water condensation, while its slippery nature optimizes collection by facilitating the immediate removal of condensed droplets (Fig. 1A).

Fig. 1B presents the specific steps involved in making the slippery radiative cooling surface. We first create a precursor solution of P(VdF-HFP) (polymer) and water (non-solvent) in acetone based on a phase-inversion process[20] to create a hierarchically porous polymer. We then place the film on a substrate and let it dry in the open air. The acetone evaporates quickly, causing the P(VdF-HFP) to phase-separate from the water, forming micro- and nanodroplets. After the water further evaporates, the porous P(VdF-HFP) coating is created, as is shown in Fig 2A. Finally, hydroxy-terminated PDMS oil was impregnated into the porous P(VdF-HFP) surface. The sample was subsequently placed in a vacuum desiccator overnight to make sure that the PDMS oil spread uniformly on the whole substrate through capillary wicking, with excess oil removed by gravity.

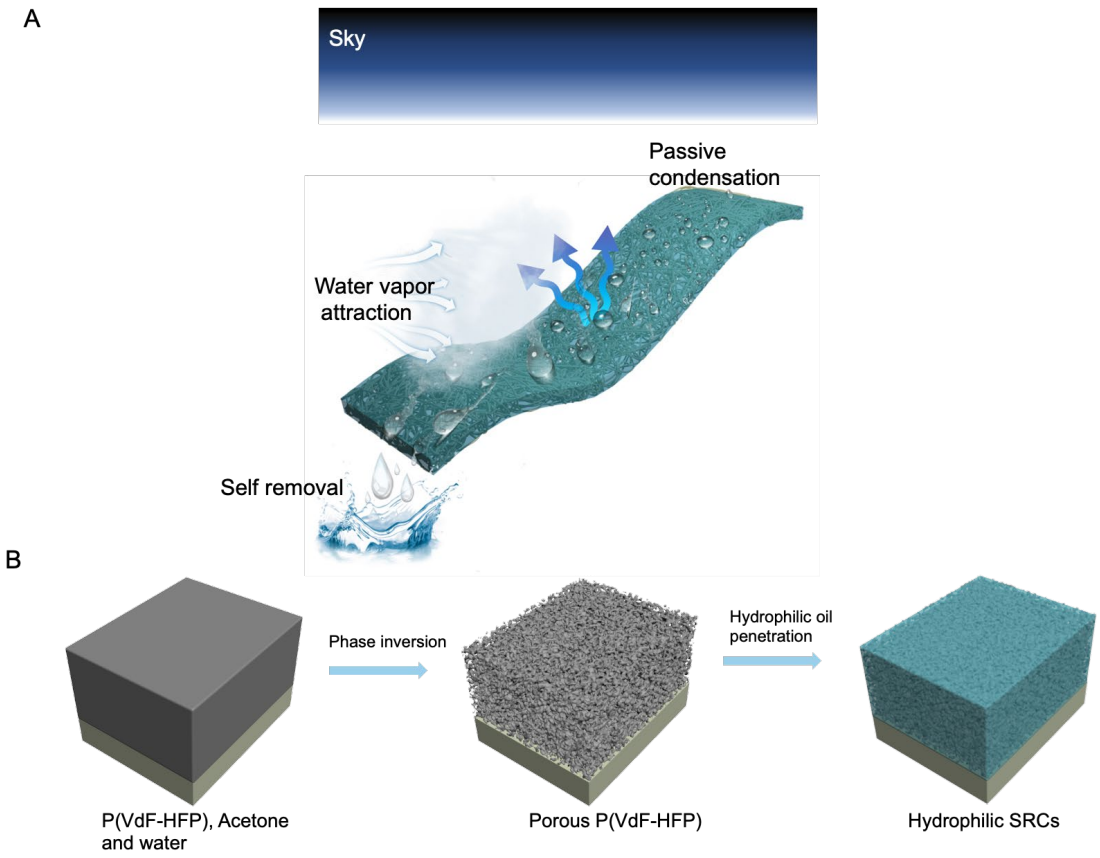

Figure 1: Design of the multi-functional hydrophilic slippery radiative cooling surfaces. (A) Working principle of atmospheric water harvesting process with slippery radiative cooling surface. B) Schematics showing the fabrication of hydrophilic SRCs by infiltrating a porous solid with lubricating film.

The nucleation process was not considered in the design of the first liquid-infused surfaces, which were created to reduce pinning forces and produce super-liquid repellency by using non-polar liquid, such as ketones[35]. Although SLIPS attracts much attention, hydrophobic but not hydrophilic oil lubricants such as silicone oil[41], Krytox oil[35,42] are widely used. To increase nucleation, hydrophilic hydroxy-terminated PDMS oil on porous P(VdF-HFP) was used for the

hydrophilic SRCs, attracting water vapor condense on the liquid surface. Because of the minimized pinning force, condensed droplets are shed from a vertical surface when they reach a particular diameter. To test this effect, besides hydrophilic SRCs, we also fabricated three other reference radiative cooling materials: hydrophobic SRCs made of hydrophobic PDMS oil on porous P(VdF-HFP) slippery surface, hydrophobic porous P(VdF-HFP) as well as a hydrophilic cellulose acetate sheet. As is shown in Fig 2C, the measured static contact angle ranges from 105° for the hydrophobic porous P(VdF-HFP) and 65° for the hydrophilic SRCs. The contact angles of the hydrophobic SRCs and the hydrophilic cellulose acetate sheet are 95° and 70° respectively. We further measured the hemispherical emittance of the four samples using a Fourier-transform-based Spectrometer equipped with an integrating sphere. As is shown in Fig 2B, all of them have an exceptionally high hemispherical emittance, ranging from 0.93-0.97. On hydrophilic SRCs, rapid droplet coalescence can efficiently increase the droplet volume over time, favoring fast droplet removal by gravitation.

To assess condensation behavior in a controlled environment, four samples were attached on the same thermal electric cooler with 5℃ below dew point with the results shown in Fig 2D. For a normal hydrophobic P(VdF-HFP) and hydrophilic cellulose surface, the water droplet pins to the surface, leading to many tiny droplets. For the hydrophobic SRCs**,** the droplets are very mobile, resulting in dynamic coalescence, however droplet nucleation is limited due to the hydrophobic nature of the surface. There are numerous nucleation sites on the hydrophilic SRCs, and the droplets are quite mobile, which makes the maximum droplet size of the hydrophilic SRCs orders of magnitude larger than the other three samples.

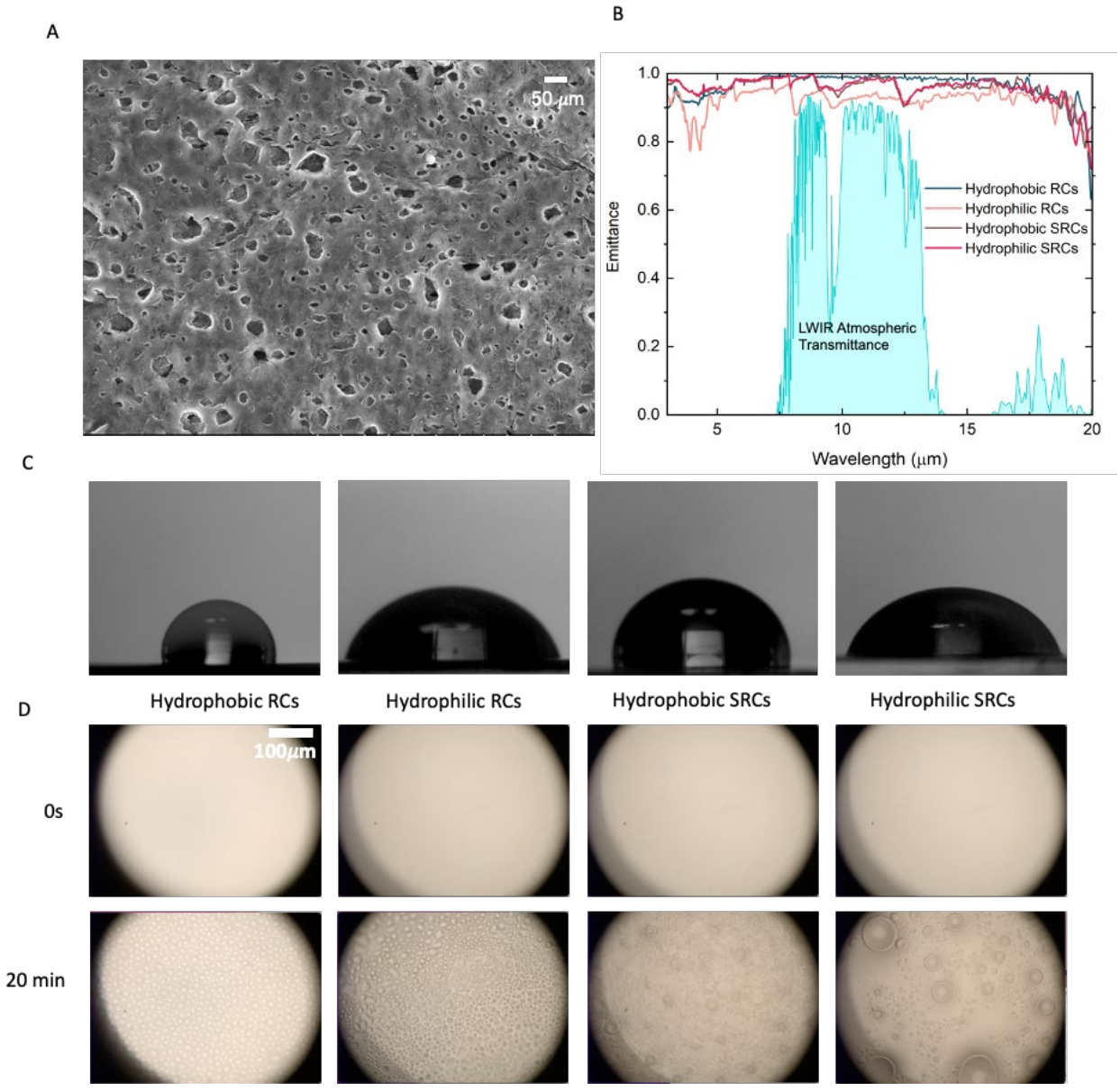

Figure 2: Comparison of four samples, hydrophobic material, hydrophilic material, hydrophobic SRCs, hydrophilic SRCs. A) SEM image of P(VdF-HFP) showing the porous features B) Measured emittance of four samples. C) Measured contact angle of four samples D) Imaged water condensation performance of four samples.

We next quantified the atmospheric water collecting performance of the SRCs, comparing their performance against the other reference materials. We performed outdoor experiments for these four samples with a custom-built apparatus as is shown in Fig. 3A. The samples were mounted vertically with a plastic holder to allow water vapor condensed on both sides of the surface to be collected by gravity. This is an important design development that allows for the practical utilization of these surfaces, as no manual removal of water is needed. Two Mylar mirrors, at a 45° angle relative to the ground, reflect the thermal radiation of the radiative cooler to the sky, facilitating radiative cooling. We demonstrated the performance of the atmospheric water collecting at a test site at the University of California, Los Angeles, (location shown in Fig. 3B), by putting these four samples into Fig. 3A apparatus during night-time hours and testing its performance.

As shown in the temperature data of Fig. 3C, immediately after the samples are exposed to the environment, all of them drop to approximately 4-6℃ below ambient temperature. Compared with the other three samples, the hydrophilic SRCs is 0.5~1 ℃ higher than the other three samples because of the larger condensation latent from higher condensation rate on the surface. This can be further explained by Fig. 4D, which summarizes the final yield of these four samples. For hydrophobic P(VdF-HFP) and hydrophilic cellulose acetate, the water droplet pins to the surface, leading to near zero collection during this 6 h period. We use a napkin to mechanically wipe the surface and measure the weight difference before and after to get the condensation yield. For hydrophobic and hydrophilic SRCs, the condensed water droplet drops by gravity and we successfully collected them with the bottom container without any other mechanical force. For

humidity ranges from 62% to 74%, we finally collect 0.5 ml water with a 0.02 m^2 radiative cooling surface in 6 hours. Another experiment is carried out at a different weather with relative humidity ranging from 68% to 87%. The temperature of these four samples is shown in Fig. 3E. Because of a more humid weather condition, they drop 3-5 ℃ below ambient temperature, which is less than the first experiment. However, because of the humid weather, more available water vapor around the radiative cooler leads to a larger yield, as is shown in Fig. 3F. For hydrophobic P(VdF-HFP) and hydrophilic cellulose acetate, although more water droplets form on the surface, the pinning effect still prevents them dropping to the bottom container. Therefore, for hydrophobic P(VdF-HFP) and hydrophilic cellulose acetate, the result in Fig. 3F shows the condensation yield which comes from the weight difference of the napkin before and after mechanically wiping the surface. Overall hydrophilic SRCs has the largest collection yield of 1.5 ml at this weather condition in 6 hours.

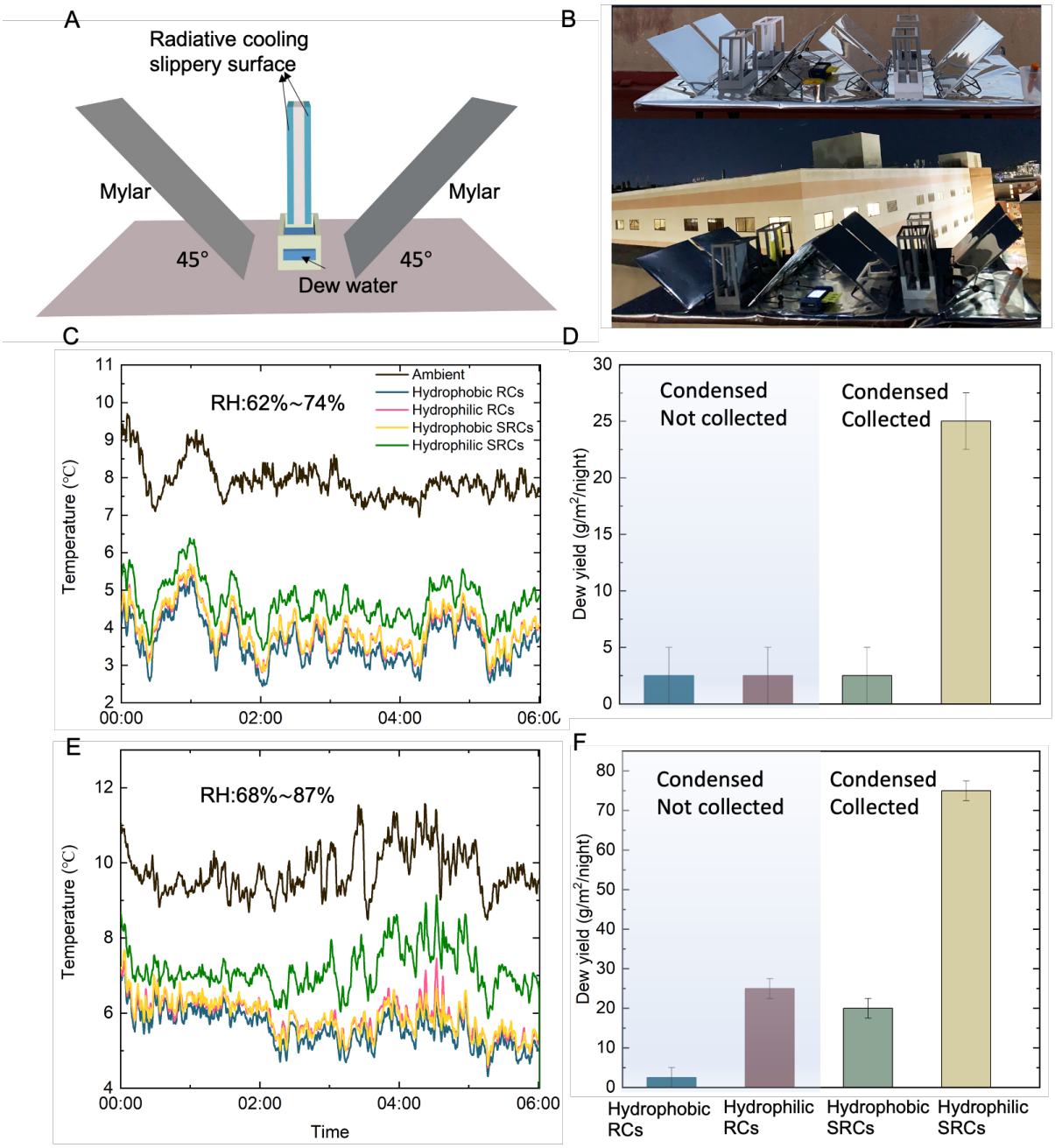

Figure 3: A) Three-dimensional schematic of the radiative cooling apparatus. B) Photo of the setup and its surroundings in University of California, CA, USA. Experiments were conducted at night. C) Measurements of temperature of four samples, including hydrophobic, hydrophilic, hydrophobic SRCs and hydrophilic SRCs against ambient temperature on a clear night at University of California on 01/03/2022. D) Experimental collection results of four samples,

including hydrophobic, hydrophilic, hydrophobic SRCs and hydrophilic SRCs. E) Measurements of temperature of four samples against ambient temperature on a clear night at University of California on 01/04/2022. F) Experimental collection results of four samples

Heat transfer coefficient is another important parameter affecting the atmospheric water collection using radiative cooling method. A smaller heat transfer coefficient leads to a colder radiative cooling surface because of the smaller heat loss to the environment. The cooler surface could condense water vapor in a dryer environment. However, the insufficient water vapor surrounding the radiative cooler causes less condensation forming on the surface. Therefore, there is an optimal heat transfer coefficient for atmospheric water collection driven by radiative cooling. To test this effect, we prepare three identical hydrophilic SRCs surfaces with the apparatus in Fig. 3A. As is shown in Fig. 4A, one sample directly contacting with ambient air without any cover, one sample encapsulated with the low density polyethylene (LDPE), and one sample partially encapsulated with LDPE with randomly making some holes on the LDPE layer. The temperature of these three setups is shown in Fig. 4B. Because of the smallest heat transfer coefficient, the sample fully closed with LDPE has the lowest temperature, but it nearly collects little amount of water shown in Fig. 4C. For the largest heat transfer coefficient, which is the sample directly contacting with air, although plenty of water vapor near the surface, the higher surface temperature limits its atmospheric water collection. As is shown in Fig. 4C, the highest atmospheric water collection comes from the partially open setup with the heat transfer coefficient closer to the ideal heat transfer coefficient.

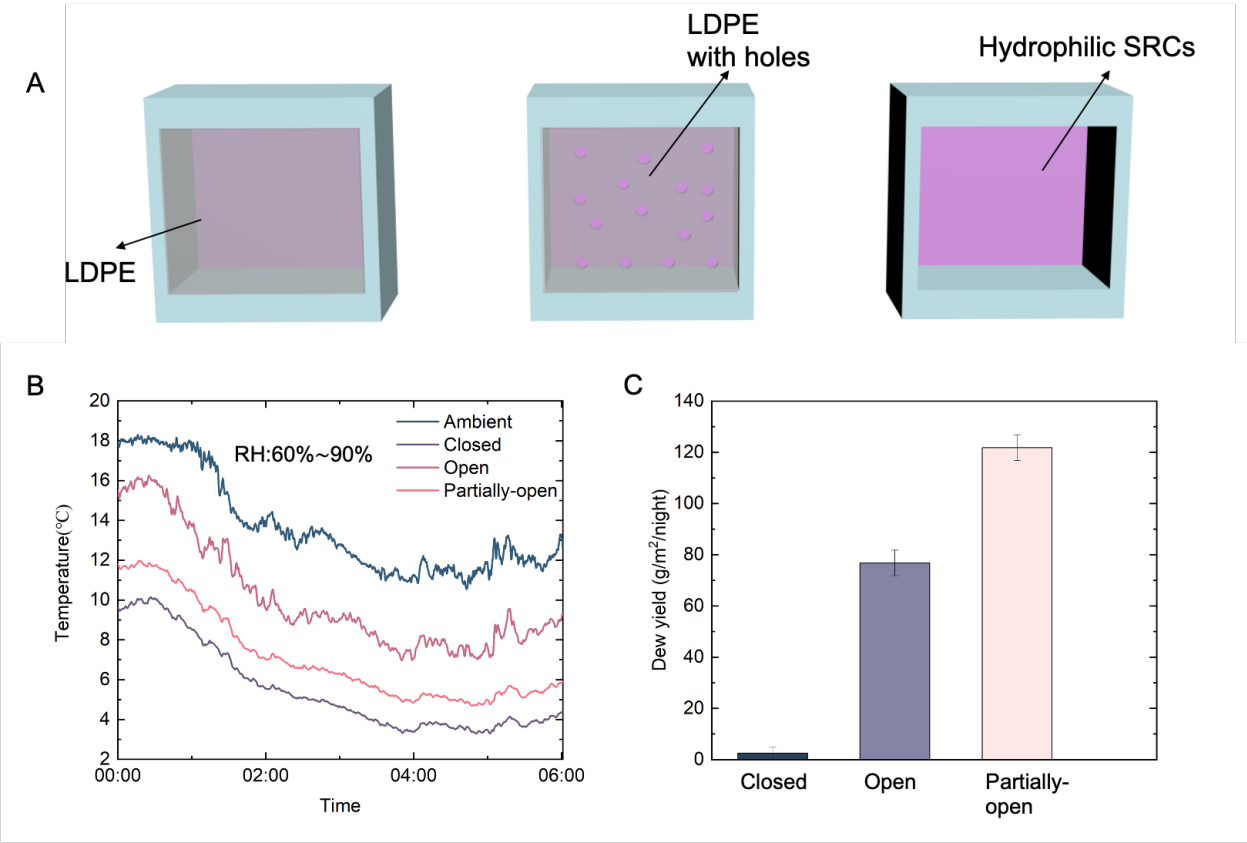

Figure 4: A) Schematic of the experiment apparatus with three different setups, sample exposed to air directly, sample sealed with low density polyethylene film, and sample partially sealed with low density polyethylene film. B) Measurements of temperature of hydrophilic SRCs with three different setups against ambient temperature on a clear night at University of California on 01/05/2022. C) Experimental water collection results of three samples with the different set up in Fig A.

We develop a theoretical model for radiative cooling atmospheric water harvesting to predict the freshwater yield. According to the relevant energy balance equation, we have that:

$$Q_{latent} = Q_{condenser}(T_{condenser}) - Q_{atm}(T_{ambient,}RH) - h\,(T_{ambient} - T_{condenser}) \quad (1)$$

where $Q_{condenser}$ represents the thermal radiation emitted from the condenser and Q_{atm} represents the absorbed downwelling atmospheric irradiance over long-wave infrared wavelengths. h is the air heat transfer coefficient due to conduction and convection.

For the second constraint, we use Lewis and Hofmann's analyses. We develop a universal expression by simultaneously analyzing heat and mass transport,

$$Q_{latent} = (Le)^n \frac{h}{\gamma}\left[RH \times P_{H_2O}(T_{ambient}) - P_{H_2O}(T_{condenser})\right] \quad (2)$$

where Q_{atm} is the Lewis number, γ is the psychrometric constant (67 PaK^{-1} at 20 °C) and P_{H_2O} is the saturation vapor pressure. Solving Eqns.(1) and (2), we can obtain Q_{latent}. And then the dew harvesting rate m' can be calculated by

$$m' = \frac{Q_{latent}}{\Delta H} \quad (3)$$

where ΔH is the evaporation latent heat per unit mass.

Experimental atmospheric water collection results of these four samples at different relative humidity are shown in Fig. 5A. As might be intuitively expected, increasing relative humidity favors the atmospheric water harvesting yield. We next calculated the theoretical limit at different relative humidity while keeping constant ambient temperature and optimal heat transfer coefficient. We can see that the water collection by our hydrophilic radiative cooling slippery surface is substantially larger than the other three samples and it closes to the theoretical limit. One advantage of our sample is that the hydrophilic oil surface attracts water vapor condensing on the

surface because of larger numbers of nucleation sites. Besides, the slippery surface will favor fast droplet removal by gravitation once the water droplet reaches a critical size. Furthermore, the fast droplet removal will recover the nucleation sites covered by the liquid droplet and increase condensation efficiency. Fig. 5B shows the freshwater atmospheric water production with the theoretical model against experiment at different heat transfer coefficients. At a specific ambient and relative humidity, there is an optimal heat transfer coefficient to maximize atmospheric water collection. A typical open system has the heat transfer coefficient from 7 $Wm^{-2}K^{-1}$ to 11 $Wm^{-2}K^{-1}$, a closed system has the heat transfer coefficient from 0 $Wm^{-2}K^{-1}$ to 1 $Wm^{-2}K^{-1}$ and a partially open system has the heat transfer coefficient from 2 $Wm^{-2}K^{-1}$ to 6 $Wm^{-2}K^{-1}$. From Fig. 5, we can see that our hydrophilic radiative cooling slippery surface substantially advances the state of art and we could also increase atmospheric water harvesting yield by adjusting the thermal system.

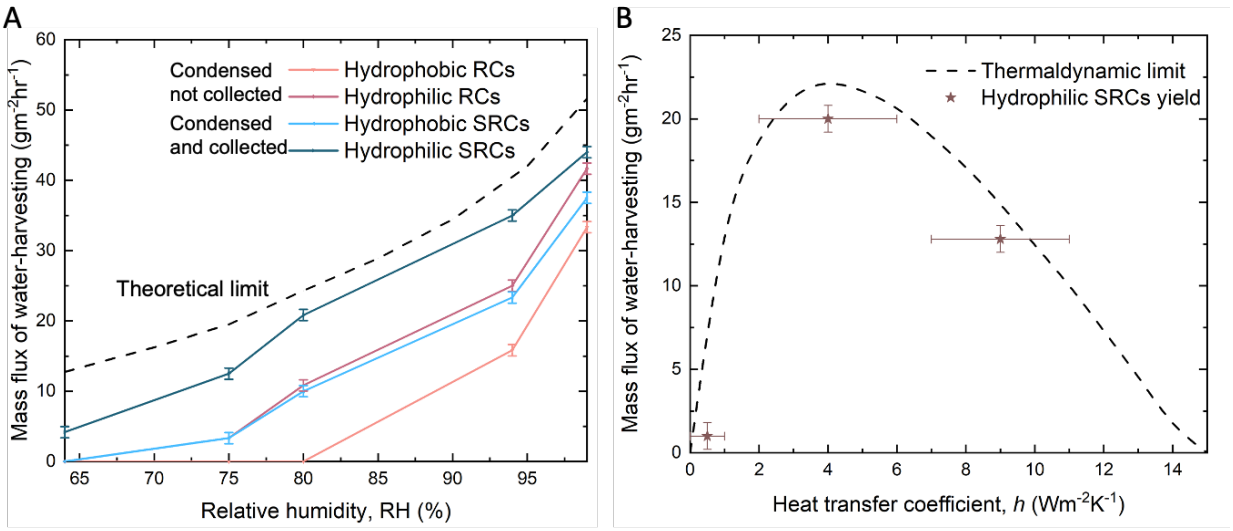

Figure 5: Simulated freshwater atmospheric water production with the theoretical model against experiment. A) Effect of relative humidity. B) Effect of heat transfer coefficient.

6.3 Conclusions

To summarize, we have highlighted the remarkable performance of atmospheric water collecting performance using the hydrophilic SRCs. Compared with other atmospheric water harvesting methods, our approach is passive and can maintain high water condensation efficiency as well as advanced water self-removal property. Furthermore, we emphasize that we could push this technology to the theoretical thermodynamic limit by parameterizing the ambient heat transfer coefficient. While radiative cooling has emerged as an important field for research in energy challenges in recent years, this work emphasizes the critical role that exploiting the thermodynamic resource of space cold could have in addressing the water challenges we face this century.

6.4 Supporting Information

Fabricating the hydrophilic slippery radiative cooling surface (SRCs)

Arkema's P(VdF-HFP) (Kynar Flex 2801) was first dissolved in acetone, then water was added to form a 1:8:1 mass ratio P(VdF-HFP)-acetone-water precursor solution. The precursor solution was then painted onto an aluminum plate to achieve the desired coating thickness. Oil-infused samples were created by utilizing the following process to infuse silicone oils with various viscosities to the surface. First of all, an appropriate amount of oil was spread to the surface and the whole surface was inside a vacuum chamber overnight. Then the excess oil was then removed from the surface followed by vertical placement of the surface for one day to ensure a thin oil layer over the surface.

Spectral characterization of the radiative cooler

The hemispherical emittance of the samples are measured by a Bruker Invenio-R FTIR spectrometer, and is shown in Fig 2B. Emittance is measured by angular reflectance measurements from 0° to 80 with integrating sphere and averaged using Eq. (6). We observe strong thermal emittance in the atmospheric window between 8 μm and 13 μm.

$$\varepsilon_\lambda = \frac{\int_0^{2\pi} \int_0^{\pi/2} \varepsilon_{\lambda,\theta}(\lambda,\theta,\phi) cos\theta sin\theta d\theta d\phi}{\int_0^{2\pi} \int_0^{\pi/2} cos\theta sin\theta d\theta d\phi} \quad (6)$$

Temperature and relative humidity measurements

Atmospheric water harvesting experiments were performed on the top floor in Bolter hall, University of California, Los Angeles. The apparatus containing the vertical samples were stabled by a plastic framework built by 3D printing. Two aluminized mylar mirrors were put on each side of the samples, as is shown in Fig 3A.

The sample surfaces were attached by a thermocouple with ±0.25 ℃ accuracy, connected to a data logger (Omega-OM-USB-TC). Ambient air temperature is measured by another thermocouple with accuracy with free air flow near the sample. The relative humidity was measured by Elitech RC-51H PDF humidity data logger with ±5% accuracy.

Contact angle measurement

A standard contact angle goniometer was used to measure the contact angle and surface tension at room temperature. By using 5 μL droplets on the test platform, all of the contact angle values were averaged from at least 5 separate measurements.

SEM Imaging

The SEM image of the samples are measured by Meas SEM - Hitachi S4700 and is shown in Fig 2A. 10 nm gold layer is deposited on the surface before SEM characterization.

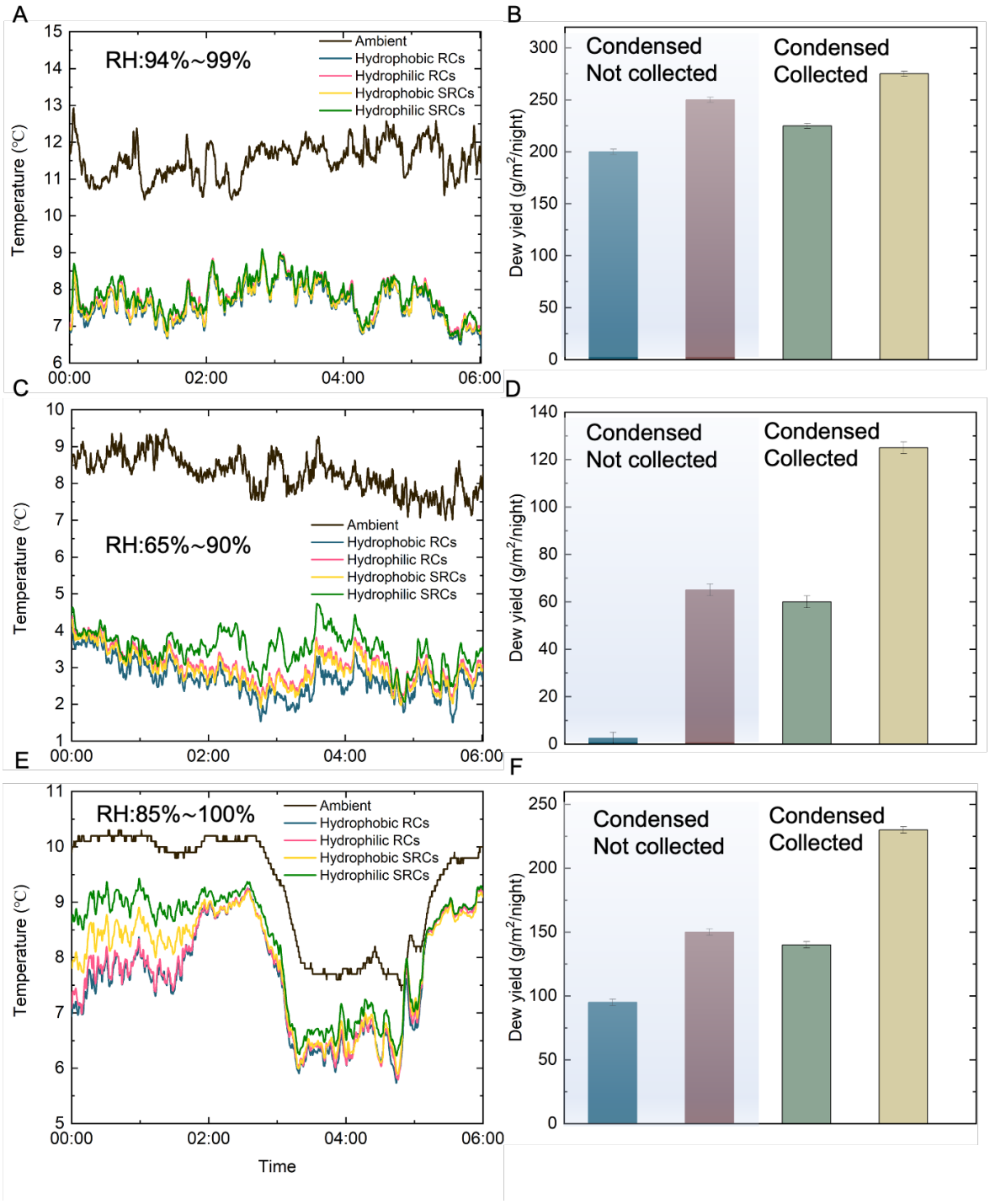

Figure S1: A) Measurements of temperature of four samples, including hydrophobic, hydrophilic, hydrophobic SRCs and hydrophilic SRCs against ambient temperature on a clear night at University of California on 12/05/2021. B) Experimental collection results of four samples, including hydrophobic, hydrophilic, hydrophobic SRCs and hydrophilic SRCs. C) Measurements of temperature of four samples against ambient temperature on a clear night at University of California on 12/20/2021. D) Experimental collection results of four samples. E) Measurements of temperature of four samples against ambient temperature on a clear night at University of California on 01/06/2022. F) Experimental collection results of four samples

To quantify the atmospheric water collecting performance, we perform more outdoor experiments for these four samples in the Bolter hall roof of University of California, Los Angles with a custom-built apparatus as is shown in Fig 3A. The samples were mounted vertically with a plastic holder to allow water vapor condensed on both sides of the surface. Two Mylar mirrors, standing 45° away from the ground, reflect the thermal radiation of the radiative cooler into space. As shown in the temperature data of Fig S1 A, immediately after the samples are exposed to the environment, all of them drop to approximately 4-6℃ below ambient temperature. Compared with the other three samples, the hydrophilic SRCs is 0.2 ℃ higher than the other three samples because of the larger condensation latent from higher condensation rate on the surface. This can be further explained by Fig S1 B, which summarizes the final yield of these four samples. For hydrophobic P(VdF-HFP) and hydrophilic cellulose acetate, the water droplet pins to the surface, leading to near zero collection during this 6h period. We use a napkin to mechanically wipe the surface and measure the weight difference before and after to get the nucleation yield. For hydrophobic and hydrophilic SRCs, the condensed water droplet drops by gravity and we successfully collected

them with the bottom container without any other mechanical force. For humidity ranges from 94% to 99%, we finally collect 4.5 ml water with 0.02 m^2 hydrophobic SRCs and 5.5 ml water with hydrophilic SRCs in 6 hours. Although the relative humidity is high tonight, the inversion layer on the sky leads to high radiative cooling power while maintaining high relative humidity. Another experiment is carried out at a different weather with relative humidity ranging from 65% to 90%. The temperature of these four samples is shown in Fig. S1 C. For this weather condition, they drop 5-6 ℃ below ambient temperature. However, because of the humid weather, more available water vapor around the radiative cooler leads to a larger yield, as is shown in Fig S1 D. We didn't collect any water for the hydrophobic and hydrophilic sample and the nucleation rate shown in the figure was measured by the weight difference of the napkin mechanically wiping the surface. We finally collect 1.2 ml water with 0.02 m^2 hydrophobic SRCs and 2.5 ml water with hydrophilic SRCs in 6 hours. For a high humidity weather, which is from 85% to 100%, the temperature data of the four samples are shown in Fig S1 E. Because of the high humidity weather, the temperature only drops 1-2℃ below ambient temperature. Even close to dew formation, the droplet forming on the surfaces didn't drop and we measured the weight difference by wiping the surface. We finally collect 2.8 ml water with 0.02 m^2 hydrophobic SRCs and 4.6 ml water with hydrophilic SRCs in 6 hours.

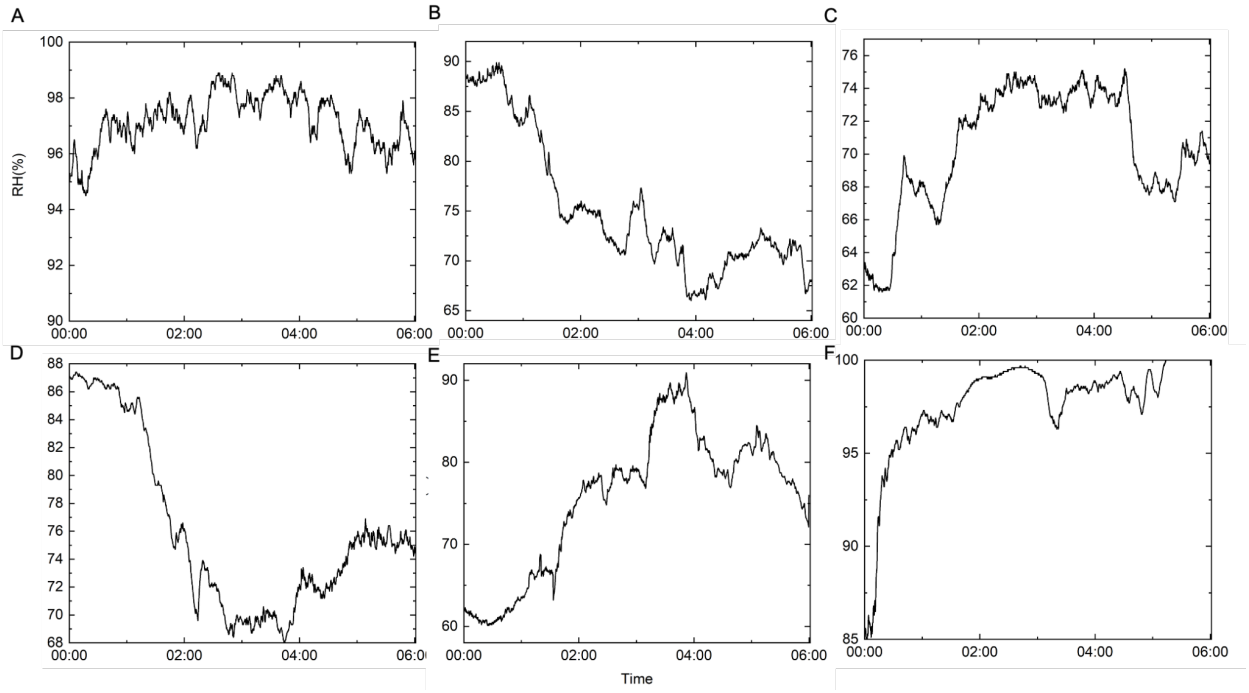

Figure S2: A) Measurements of relative humidity (RH) on a clear night at University of California on 12/05/2021, shown for Fig S1A. B) Measurements of relative humidity (RH) on a clear night at University of California on 12/20/2021, shown for Fig S1C. C) Measurements of relative humidity (RH) on a clear night at University of California on 01/03/2022, shown for Fig 3C. D) Measurements of relative humidity (RH) on a clear night at University of California on 01/04/2022, shown for Fig 3D. E) Measurements of relative humidity (RH) on a clear night at University of California on 01/05/2022, shown for Fig 4B. F) Measurements of relative humidity (RH) on a clear night at University of California on 01/06/2022, shown for Fig S1E.

6.5 References

1. Zhuang, S., Qi, H., Wang, X., Li, X., Liu, K., Liu, J., and Zhang, H. (2021). Advances in Solar-Driven Hygroscopic Water Harvesting. Glob. Chall. *5*, 2000085.

10.1002/gch2.202000085.

2. Mekonnen, M.M., and Hoekstra, A.Y. Four billion people facing severe water scarcity. Sci. Adv. *2*, e1500323. 10.1126/sciadv.1500323.
3. Zhou, X., Lu, H., Zhao, F., and Yu, G. (2020). Atmospheric Water Harvesting: A Review of Material and Structural Designs. ACS Mater. Lett. *2*, 671–684. 10.1021/acsmaterialslett.0c00130.
4. Wikramanayake, E.D., Ozkan, O., and Bahadur, V. (2017). Landfill gas-powered atmospheric water harvesting for oilfield operations in the United States. Energy *138*, 647–658. 10.1016/j.energy.2017.07.062.
5. Wahlgren, R.V. (2001). Atmospheric water vapour processor designs for potable water production: a review. Water Res. *35*, 1–22. 10.1016/S0043-1354(00)00247-5.
6. Zhang, H., Yoshino, H., Hasegawa, K., Liu, J., Zhang, W., and Xuan, H. (2017). Practical moisture buffering effect of three hygroscopic materials in real-world conditions. Energy Build. *139*, 214–223. 10.1016/j.enbuild.2017.01.021.
7. Kallenberger, P.A., and Fröba, M. (2018). Water harvesting from air with a hygroscopic salt in a hydrogel–derived matrix. Commun. Chem. *1*, 1–6. 10.1038/s42004-018-0028-9.
8. Li, R., Shi, Y., Alsaedi, M., Wu, M., Shi, L., and Wang, P. (2018). Hybrid Hydrogel with High Water Vapor Harvesting Capacity for Deployable Solar-Driven Atmospheric Water Generator. Environ. Sci. Technol. *52*, 11367–11377. 10.1021/acs.est.8b02852.
9. Wang, D.C., Xia, Z.Z., Wu, J.Y., Wang, R.Z., Zhai, H., and Dou, W.D. (2005). Study of a novel silica gel–water adsorption chiller. Part I. Design and performance prediction. Int. J. Refrig. *28*, 1073–1083. 10.1016/j.ijrefrig.2005.03.001.
10. Ng, K.C., Chua, H.T., Chung, C.Y., Loke, C.H., Kashiwagi, T., Akisawa, A., and Saha, B.B.

(2001). Experimental investigation of the silica gel–water adsorption isotherm characteristics. Appl. Therm. Eng. *21*, 1631–1642. 10.1016/S1359-4311(01)00039-4.

11. Zhuravlev, L.T. (2000). The surface chemistry of amorphous silica. Zhuravlev model. Colloids Surf. Physicochem. Eng. Asp. *173*, 1–38. 10.1016/S0927-7757(00)00556-2.
12. Trzpit, M., Soulard, M., Patarin, J., Desbiens, N., Cailliez, F., Boutin, A., Demachy, I., and Fuchs, A.H. (2007). The Effect of Local Defects on Water Adsorption in Silicalite-1 Zeolite: A Joint Experimental and Molecular Simulation Study. Langmuir *23*, 10131–10139. 10.1021/la7011205.
13. Jänchen, J., Ackermann, D., Stach, H., and Brösicke, W. (2004). Studies of the water adsorption on Zeolites and modified mesoporous materials for seasonal storage of solar heat. Sol. Energy *76*, 339–344. 10.1016/j.solener.2003.07.036.
14. Wei, X., Wang, W., Xiao, J., Zhang, L., Chen, H., and Ding, J. (2013). Hierarchically porous aluminosilicates as the water vapor adsorbents for dehumidification. Chem. Eng. J. *228*, 1133–1139. 10.1016/j.cej.2013.05.062.
15. Kalmutzki, M.J., Diercks, C.S., and Yaghi, O.M. (2018). Metal–Organic Frameworks for Water Harvesting from Air. Adv. Mater. *30*, 1704304. 10.1002/adma.201704304.
16. Kim, H., Yang, S., Rao, S.R., Narayanan, S., Kapustin, E.A., Furukawa, H., Umans, A.S., Yaghi, O.M., and Wang, E.N. (2017). Water harvesting from air with metal-organic frameworks powered by natural sunlight. Science *356*, 430–434. 10.1126/science.aam8743.
17. Dietzel, P.D.C., Johnsen, R.E., Blom, R., and Fjellvåg, H. (2008). Structural Changes and Coordinatively Unsaturated Metal Atoms on Dehydration of Honeycomb Analogous Microporous Metal–Organic Frameworks. Chem. – Eur. J. *14*, 2389–2397. 10.1002/chem.200701370.

18. Raman, A.P., Anoma, M.A., Zhu, L., Rephaeli, E., and Fan, S. (2014). Passive radiative cooling below ambient air temperature under direct sunlight. Nature *515*, 540–544. 10.1038/nature13883.

19. Chen, Z., Zhu, L., Raman, A., and Fan, S. (2016). Radiative cooling to deep sub-freezing temperatures through a 24-h day–night cycle. Nat. Commun. *7*, 13729. 10.1038/ncomms13729.

20. Mandal, J., Fu, Y., Overvig, A.C., Jia, M., Sun, K., Shi, N.N., Zhou, H., Xiao, X., Yu, N., and Yang, Y. (2018). Hierarchically porous polymer coatings for highly efficient passive daytime radiative cooling. Science *362*, 315–319. 10.1126/science.aat9513.

21. Trombe, F. Perspectives sur l'utilisation des rayonnements solaires et terrestres dans certaines re´gions du monde. Revue Generale Thermique 6, 1215–1234 (1967).

22. Berdahl, P. (1984). Radiative cooling with MgO and/or LiF layers. Appl. Opt. *23*, 370–372. 10.1364/AO.23.000370.

23. Raman, A.P., Li, W., and Fan, S. (2019). Generating Light from Darkness. Joule *3*, 2679–2686. 10.1016/j.joule.2019.08.009.

24. Bhatia, B., Leroy, A., Shen, Y., Zhao, L., Gianello, M., Li, D., Gu, T., Hu, J., Soljačić, M., and Wang, E.N. (2018). Passive directional sub-ambient daytime radiative cooling. Nat. Commun. *9*, 5001. 10.1038/s41467-018-07293-9.

25. Granqvist, C.G., and Hjortsberg, A. (1981). Radiative cooling to low temperatures: General considerations and application to selectively emitting SiO films. J. Appl. Phys. *52*, 4205–4220. 10.1063/1.329270.

26. Hossain, M.M., and Gu, M. (2016). Radiative Cooling: Principles, Progress, and Potentials. Adv. Sci. *3*, 1500360. 10.1002/advs.201500360.

27. Zhao, D., Aili, A., Zhai, Y., Xu, S., Tan, G., Yin, X., and Yang, R. (2019). Radiative sky cooling: Fundamental principles, materials, and applications. Appl. Phys. Rev. *6*, 021306. 10.1063/1.5087281.

28. Mandal, J., Yang, Y., Yu, N., and Raman, A.P. (2020). Paints as a Scalable and Effective Radiative Cooling Technology for Buildings. Joule *4*, 1350–1356. 10.1016/j.joule.2020.04.010.

29. Huang, X., Mandal, J., and Raman, A. (2021). Do-it-yourself radiative cooler as a radiative cooling standard and cooling component for device design. J. Photonics Energy *12*, 012112. 10.1117/1.JPE.12.012112.

30. Gentle, A.R., and Smith, G.B. (2015). A Subambient Open Roof Surface under the Mid-Summer Sun. Adv. Sci. *2*, 1500119. 10.1002/advs.201500119.

31. Muselli, M., Beysens, D., Mileta, M., and Milimouk, I. (2009). Dew and rain water collection in the Dalmatian Coast, Croatia. Atmospheric Res. *92*, 455–463. 10.1016/j.atmosres.2009.01.004.

32. Muselli, M., Beysens, D., Marcillat, J., Milimouk, I., Nilsson, T., and Louche, A. (2002). Dew water collector for potable water in Ajaccio (Corsica Island, France). Atmospheric Res. *64*, 297–312. 10.1016/S0169-8095(02)00100-X.

33. Zhou, M., Song, H., Xu, X., Shahsafi, A., Qu, Y., Xia, Z., Ma, Z., Kats, M.A., Zhu, J., Ooi, B.S., et al. (2021). Vapor condensation with daytime radiative cooling. Proc. Natl. Acad. Sci. *118*. 10.1073/pnas.2019292118.

34. Haechler, I., Park, H., Schnoering, G., Gulich, T., Rohner, M., Tripathy, A., Milionis, A., Schutzius, T.M., and Poulikakos, D. (2021). Exploiting radiative cooling for uninterrupted 24-hour water harvesting from the atmosphere. Sci. Adv. *7*, eabf3978.

10.1126/sciadv.abf3978.

35. Wong, T.-S., Kang, S.H., Tang, S.K.Y., Smythe, E.J., Hatton, B.D., Grinthal, A., and Aizenberg, J. (2011). Bioinspired self-repairing slippery surfaces with pressure-stable omniphobicity. Nature *477*, 443–447. 10.1038/nature10447.

36. Dai, X., Sun, N., Nielsen, S.O., Stogin, B.B., Wang, J., Yang, S., and Wong, T.-S. (2018). Hydrophilic directional slippery rough surfaces for water harvesting. Sci. Adv. *4*, eaaq0919. 10.1126/sciadv.aaq0919.

37. Feng, R., Xu, C., Song, F., Wang, F., Wang, X.-L., and Wang, Y.-Z. (2020). A Bioinspired Slippery Surface with Stable Lubricant Impregnation for Efficient Water Harvesting. ACS Appl. Mater. Interfaces *12*, 12373–12381. 10.1021/acsami.0c00234.

38. Guo, Z., Zhang, L., Monga, D., Stone, H.A., and Dai, X. (2021). Hydrophilic slippery surface enabled coarsening effect for rapid water harvesting. Cell Rep. Phys. Sci. *2*, 100387. 10.1016/j.xcrp.2021.100387.

39. Lyu, P., Zhang, X., Peng, M., Shang, B., and Liu, X. (2021). Multibioinspired Wettable Patterned Slippery Surface for Efficient Water Harvesting. Adv. Mater. Interfaces *8*, 2100691. 10.1002/admi.202100691.

40. Samaha, M.A., and Gad-el-Hak, M. (2021). Slippery surfaces: A decade of progress. Phys. Fluids *33*, 071301. 10.1063/5.0056967.

41. Anand, S., Rykaczewski, K., Subramanyam, S.B., Beysens, D., and Varanasi, K.K. (2014). How droplets nucleate and grow on liquids and liquid impregnated surfaces. Soft Matter *11*, 69–80. 10.1039/C4SM01424C.

42. Sun, J., and Weisensee, P.B. (2019). Microdroplet self-propulsion during dropwise condensation on lubricant-infused surfaces. Soft Matter *15*, 4808–4817.

10.1039/C9SM00493A.